

NEURAL NETWORK BASED VECTOR HYSTERESIS MODEL AND THE NONDESTRUCTIVE TESTING METHOD

by

MIKLÓS KUCZMANN
MSc in Electrical Engineering

supervisor

PROF. AMÁLIA IVÁNYI

A thesis submitted to the
Budapest University of Technology and Economics
for the degree of
DOCTOR OF PHILOSOPHY
IN ELECTRICAL ENGINEERING

Department of Broadband Infocommunications and Electromagnetic Theory
Budapest University of Technology and Economics
Budapest
2004

Contents

1	Introduction and the scope of my research	1
1.1	The proposed research activity	2
1.2	Acknowledgment	3
2	Literature overview	4
2.1	Artificial neural networks	4
2.1.1	Biological background	4
2.1.2	Structure and training of feedforward neural networks	4
2.2	Preisach–type hysteresis models based on NN	7
2.2.1	The classical scalar Preisach model	7
2.2.2	The classical scalar Preisach model via NNs	10
2.2.3	Vector hysteresis modeling	12
2.3	The nondestructive testing method	14
2.4	Formulation and potentials of the electromagnetic field problems	15
2.5	The finite element method	17
2.5.1	Nodal finite elements	18
2.5.2	Edge finite elements	19
2.5.3	FEM in 2D using linear shape functions	20
2.5.4	FEM in 3D using linear shape functions	23
3	Neural network based hysteresis operator	25
3.1	The scalar hysteresis operator	25
3.1.1	Training sequence and preprocessing of measured data	25
3.1.2	Operation of the model	27
3.1.3	Properties of the scalar model	29
3.1.4	Scalar magnetic hysteresis measurement using LabVIEW	31
3.2	The isotropic vector hysteresis operator	34
3.2.1	Description of the model	34
3.2.2	The identification process	34
3.2.3	Verification of the model	39
3.3	The anisotropic vector hysteresis operator	41

3.3.1	Anisotropic model in 2D	41
3.3.2	Anisotropic model in 3D	44
3.3.3	The relation between the scalar and the vector Everett functions	47
3.4	Some properties of the vector hysteresis characteristics	51
3.5	New scientific results	53
4	Nonlinear FEM using edge finite elements	55
4.1	Problem definition and the FEM formulation	55
4.1.1	Time varying magnetic field problem in linear media	56
4.1.2	Eddy current field in linear media	59
4.1.3	The $\mathbf{T}, \Psi - \Psi$ formulation in hysteretic media	65
4.2	Summary	71
4.3	New scientific results	71
5	Simulation of the built NDT measurement system	72
5.1	Description of the measurement system	72
5.2	Applying the FluxSet sensor	74
5.2.1	Preliminary measurements	74
5.2.2	Calibration of the sensor	75
5.2.3	The lock-in amplifier	77
5.2.4	NDT measurements	78
5.3	Applying the Hall-type sensor	81
5.3.1	Preliminary measurements and calibration	81
5.3.2	NDT measurements	82
5.4	Conclusions of the measurements	83
5.5	Simulation of the installed NDT equipment	86
5.5.1	Global-local model in 3D calculations	86
5.5.2	Simulation of the Hall sensor	93
5.6	New scientific results	97
6	Summary of the new scientific results	98
7	Conclusions and future developments	100

Notations

NN	Neural Network
NDT	Nondestructive Testing
FEM	Finite Element Method
MSE	Means Square Error
BP	Backpropagation training method
PE	Processing Element (neuron)
CAD	Computer Aided Design
NI	National Instruments
DAQ	Data Acquisition
DC, AC	Direct Current, Alternating Current
CC mode	Constant Current mode of the power supply
W	Weight matrix of a neural network
$\mu(\alpha, \beta)$	Preisach distribution function
$E(\alpha, \beta)$	Everett function
$F(\alpha, \beta)$	Measured Everett function for the isotropic vector model
$F(\alpha, \beta, \varphi)$	Measured Everett function for the 2D anisotropic vector model
$F(\alpha, \beta, \varphi, \vartheta)$	Measured Everett function for the 3D anisotropic vector model
F_m, F_{nm}	Fourier coefficients of the measured anisotropic Everett function
E_m, E_{nm}	Fourier coefficients of the identified anisotropic Everett function
$\mathcal{H}\{\}, \mathcal{H}_M\{\}, \mathcal{H}_B\{\}$	Hysteresis operator
ξ	Parameter of a reversal hysteresis curve
$\hat{\gamma}(\alpha, \beta)$	Relay operator
H, \mathbf{H}	Magnetic field intensity (scalar, vector)
M, \mathbf{M}	Magnetization (scalar, vector)
B, \mathbf{B}	Magnetic flux density (scalar, vector)
\mathbf{J}_0	Current density of the exciting current
\mathbf{J}_e	Eddy current density
\mathbf{J}	Total current density
\mathbf{E}	Electric field intensity
μ_0	Vacuum permeability
μ_r	Relative permeability

σ	Conductivity
Ψ	Magnetic scalar potential
\mathbf{T}_0	Impressed field quantity of the exciting current
\mathbf{T}	Current vector potential
N_i	Nodal shape functions
\mathbf{W}_k	Edge shape functions
$\mathbf{e}_x, \mathbf{e}_y, \mathbf{e}_z$	Cartesian coordinates
f, ω	Frequency, angular frequency
t	Time
\hat{I}	Peak value of the exciting current

Chapter 1

Introduction and the scope of my research

From mathematical and engineering point of view, the hysteresis characteristic is a non-linear and multivalued relationship between the magnetic field intensity and the magnetization of the magnetic materials. This phenomenon has been researched by many physicists and material scientists as well. The point of view of interests may be very different; the physicists are interested in the microscopic behavior and the microscopic description of the magnetic materials, the mathematicians treat this as an interesting mathematical problem from the field of nonlinear systems. I focus on the models of hysteresis characteristics of the ferromagnetic materials –as many engineers– as a mathematical tool to handle the hysteretic behavior of the magnetic materials, to work out a model with simple identification process which can be built into a finite element software.

The possible origin of magnetism is the motion of electrons at different energy levels in the atomic structures of the materials and this motion can be simulated by elementary current loops. The associated magnetic dipoles are characterized by the magnetic moments. The volume density of the vector sum of these moments results in the magnetization vector. The assumption of elementary current loops is the basis of the macroscopic description and of the theory of domain structure. Microscopic models consider energy contributions on very small dimensions, based on energy minimization of different energy terms (e.g. demagnetization, anisotropic, exchange and so on). The microscopic models have precise physical justification, but it may be difficult to apply them to solve real engineering problems, because of the very large computation time.

Applying neural networks in the field of function approximation has the advantage of easy identification, and the resulting model can approximate the measured object attractively as a continuous function. At the same time, neural networks are black box models, and there is no connection between the physical meaning of the phenomenon to be simulated and the parameters of the model. The main challenge of simulations is to predict the behavior of an arrangement, but the atomic level and the microscopic behavior are not in the focus of engineers. The basis of simulations is to work out a mathematical model of the given arrangement and a mathematical model of the material behavior. These models can be applied to calculate the physical quantities which we are interested in.

In engineering practice, the simulation of measuring arrangements and various electrical equipments is based on Maxwell's equations coupled with the constitutive relations.

It is very important to take into account the hysteretic behavior as well as the vector property of the magnetic field quantities. However, in some cases it is adequate to use constant permeability or single valued nonlinearity. Hysteresis characteristics must be taken into consideration when, for example, hysteresis losses in electrical machines or effects related to the remanent magnetization are to be calculated.

The finite element method is the most widely used and the most popular simulation technique in the solution of electromagnetic field problems. The weak form of the partial differential equations formulated by potentials, obtained from Maxwell's equations can be solved by using simple shape functions on a discrete mesh of the arrangement. When hysteresis characteristics must be taken into consideration, the solver and the model must be coupled by an adequate iteration scheme, because the resulting system of equations is nonlinear.

Nowadays, electromagnetic nondestructive evaluation methods have a dynamic and intense development, applied to secure the structural integrity of complex mechanical systems. Nondestructive inspection techniques require continuously better and better detection sensitivity and field applicability. There are several benchmark problems can be found in the literature aiming to compare different measuring systems, computer software and solvers. There are some common areas of nondestructive testing, e.g. optimization of probes, fast electromagnetic field analysis to reconstruct natural cracks, etc.

1.1 The proposed research activity

The scope of my PhD dissertation is to develop a new neural network based vector hysteresis operator and the insertion of this model into a three dimensional finite element based procedure to simulate an installed nondestructive testing equipment.

In view of the advantageous properties of neural networks in function approximation, it is a challenge for me to develop a new neural network based scalar hysteresis operator. I intend to build a measurement system to show the applicability of the predictions of the model by comparing scalar measurements and simulation results. I will generalize the scalar model to describe the vector hysteresis property in 2D and in 3D, and I will take into account the anisotropic behavior as well. My aim is to develop an original identification procedure to fit the isotropic and the anisotropic models to measured hysteresis curves. Unfortunately, the vector hysteresis measurement is a large project in itself, especially no 3D measurements are known to me. This is beyond my research's scope, that is why I will generate 2D and 3D measurements via the Preisach model.

I intend to build a nondestructive testing measurement system, and to realize simple test measurements by applying the FluxSet sensor and the Hall-type sensor as well. I will examine manufactured specimens with well defined artificial slots and holes. My aim is not to work out a new measurement system, but to allow to check the simulation results obtained from calculations introduced in the next paragraph.

To simulate the above measurement system, I will apply the finite element method with the combination of the nodal and the edge shape functions. I intend to develop a 3D finite element model of the arrangement and to take into account the effect of hysteresis characteristics by comparing measured and simulated results. I will use the $\mathbf{T}, \Psi - \Psi$ potential formulation, because it directly gives the magnetic field intensity vector, therefore I can apply the direct isotropic neural network based vector hysteresis model. I intend to identify the isotropic vector hysteresis model from measurements,

using a specimen of toroidal shape made of the same material as the nondestructive testing arrangement. I will develop and implement in the finite element method a fixed-point iteration scheme to handle the nonlinearity of the hysteresis characteristics.

The organization of my dissertation is the following.

Chapter 2 contains a brief overview of some results known from the literature. The basics of the application of neural networks in system identification, scalar and vector hysteresis models based on neural network techniques, the general nondestructive testing methods and procedures, and an overview of the finite element method, especially edge finite elements can be found here. A short introduction, how to develop the nodal and the edge shape functions for triangular and tetrahedral finite elements is also given.

The following chapters contain the summary of my research activity.

In Chapter 3, I introduce the neural network based scalar hysteresis operator developed by me. I present some comparisons with real scalar measurements to show the applicability of the model. I perform a possible generalization to describe 2D and 3D vector properties, and I propose a new and original identification technique. The generalization has been worked out both for the isotropic as well as the anisotropic case.

In Chapter 4, I describe the finite element based procedure developed both for the time varying magnetic field and the eddy current field problems. First of all, I have analyzed a simple 2D arrangement, then I have introduced the global to local model in 3D to simulate the measurement equipment introduced in Chapter 5. I introduce the fixed-point iteration scheme to handle the nonlinearity of the simulated material. Chapter 5 deals with the studied nondestructive testing equipment built in our Magnetic Laboratory. The arrangement worked out and the studied specimens, the applied sensors and the measurement set-up controlled by a graphical user interface implemented in the frame of the software package LabVIEW are discussed. Finally, I show some comparisons between measurements and simulations to verify the computations.

Last, the summary of my dissertation, the PhD theses can be found in Chapter 6, and conclusions with future works are presented in Chapter 7. Main references in alphabetical order used through my research are also given at the end of this dissertation.

I used the \LaTeX word processor to write this document. Figures are located at the top of the actual page. I used the following notations: vectors are denoted by bold italic letters, e.g. \mathbf{T} , scalars are denoted by italic letters, e.g. μ , matrices and arrays are denoted by bold letters, e.g. \mathbf{K} .

1.2 Acknowledgment

I wish to express my grateful acknowledgement to my supervisor Amália Iványi for her advices, encouragements and suggestions provided during my PhD studies. I am very grateful to Imre Sebestyén, Oszkár Bíró, Maurizio Repetto, Carlo Ragusa, József Pávó and János Szöllősy for their assistance during developing the finite element software and the measurements using the FluxSet sensor. The scalar hysteresis measurements have been developed with the help of Péter Kis and János Füzi. I thank my student, Szilárd Jagasics for developing the Hall sensor. I would like to express my thanks to György Fodor, Oszkár Bíró and Imre Sebestyén for reading of the dissertation and for the helpful suggestions and also for all members of the Department. I thank the scholarship provided by the Tateyama Laboratory Hungary Ltd. Last but not least, I would like to thank my family, my parents and my girlfriend, Lívía Kicsák for the daily assistance and patience.

Chapter 2

Literature overview

In this chapter, I briefly present the major research directions in the field of application of neural networks in system identification, using neural networks in hysteresis modeling, and formulations of the finite element method, especially in the field of nondestructive testing. I focus on the topics which are close to my research activity.

2.1 Artificial neural networks

Artificial neural networks (NNs) are parallel, information-processing systems implemented by hardware (like Hopfield-type NN, HNN, Cellular Neural Network, CNN) or software (simulation tools, e.g. NN Toolbox of the software package MATLAB). Applying the technique of NNs is a quite new and challenging field of research, motivated by neuroscience, the study of the human brain and the nervous system. The brain's capacity of self-accommodation, powerful thinking, remembering and problem solving capabilities have inspired many scientists to attempt computer modeling of its operation [19, 25, 27].

2.1.1 Biological background

The human brain and nervous system consist of billions of ganglion-cells which are densely interconnected. For example, the human brain is estimated to have 10^{11} to 10^{12} neurons with more than 10^{15} synapses among them. The function of individual nerve-cells or how groups of neurocytes operate together is the scope of investigations by neurologists and neuroscientists.

The structure of a biological neuron is very tricky. There are three main parts building a neuron; the cell body (soma) is the central part of the ganglion-cell containing the nucleus, the dendrites where the excitation is accepted, and the axon (neurite) is the continuation of the soma splitting up nerve endings and connects to other dendrites through synapses [4].

2.1.2 Structure and training of feedforward neural networks

There is an increasing number of different types of NNs, like feedforward NNs, Adaptive Resonance Theory (ART) networks, Cerebellar Model Articulation Controllers (CMAC), Principal Component Analysis (PCA) networks, CNN, HNN, and so on. There is a large number of books in this field, I mainly studied and worked through [19, 25, 27], where the

structure, the training methods and a wide range of applications can be found. I used the group of feedforward-type NNs to approximate hysteresis characteristics, because this is the simplest NN.

Feedforward NNs can be applied as an alternative mathematical tool for universal function approximation. This application is based on the Kolmogorov–Arnold theorem (1958) [27]:

Kolmogorov–Arnold 2.1.1 *For each positive integer n , there exist $2n + 1$ continuous functions $\Phi_1, \Phi_2, \dots, \Phi_{2n+1}$, mapping $[0, 1]$ into the real line, and having the additional property that, for any continuous function f of n real variables, there is a continuous function Ψ of one variable on $[0, n]$ into the real line such that*

$$f(x_1, x_2, \dots, x_n) = \sum_{q=1}^{2n+1} \Psi \left(\sum_{p=1}^n \Phi_q(x_p) \right), \quad (2.1)$$

for all values of x_1, x_2, \dots, x_n in $[0, 1]$.

There is no general rule yet, how to choose the functions Ψ and Φ_q , but there is a lot of latitude from experimental methods.

The formulation (2.1) can be represented by feedforward type NNs with at least two hidden layers with nonlinear activation function.

The output of an individual neuron (processing element, PE) y is the output of the so called activation function (transfer function) $\psi(s)$ and the input of this transfer function is the linear combination of I inputs, $\mathbf{x} = [x_1, x_2, \dots, x_I]^T$ and the bias b of the PE, $s = \sum_{i=1}^I w_i x_i + b = \mathbf{w}^T \mathbf{x} + b$, where the vector \mathbf{w} contains the weight parameters of a neuron, $\mathbf{w} = [w_1, w_2, \dots, w_I]^T$ (see the upper right hand corner of Fig. 2.1). The transfer functions are generally non-linear, continuous and differentiable functions. There are some widely used activation functions (e.g. hard limit, linear, saturating linear, radial basis function and so on), I used the bipolar sigmoidal function (hyperbolic tangent function),

$$\psi(s) = \frac{1 - e^{-2s}}{1 + e^{-2s}}. \quad (2.2)$$

This function transfers its input space $s \in \mathbb{R}$ into the interval $[-1, \dots, +1]$.

A feedforward NN can be built by using such PEs grouping them into layers as it can be seen in Fig. 2.1. The inputs of the neurons in layer j are the weighted sum of the outputs of the neurons in layer $j - 1$. In this case, a multi input single output (MISO) system has been shown for simplicity.

After selecting the activation functions of the individual neurons and the number of layers and neurons, the only degree of freedom left is setting the value of weights and biases of the NN. Weights and biases of neurons in a layer are collected in the weight matrix \mathbf{W} . Training is an iterative and convergent algorithm which modifies the weights and the biases until a given value of a suitably defined error ε (e.g. mean square error, MSE, sum squared error, SSE, etc.) between the desired output value (target) t and the output of the NN d according to the given input vector \mathbf{x} is reached. This training method is based on the training sequence, $\tau^{(N)} = \{(\mathbf{x}_k, t_k), k = 1, \dots, N\}$, which may be a set of measured data, that should be approximated by the NN, i.e. $t_k = f(\mathbf{x}_k)$, $k = 1, \dots, N$. The function $f(\cdot)$ represents the measured functional relationship between the input–output patterns, and N denotes the number of measured data pairs.

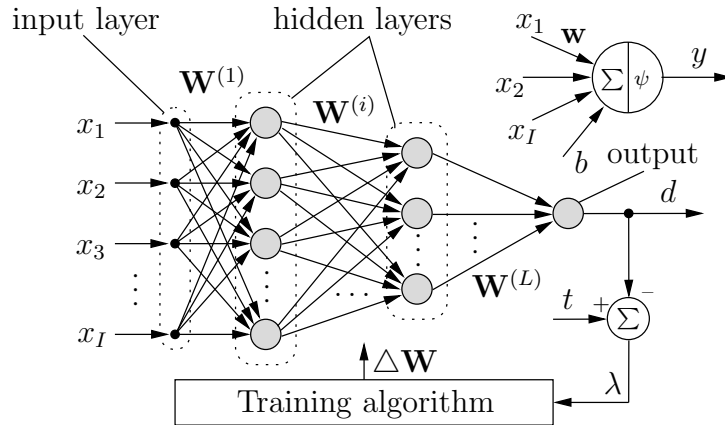


Fig. 2.1. Structure and training of feed-forward type NNs

According to the training sequence $\tau^{(N)}$, the aim of training is to find the optimal weight coefficients and biases of the network \mathbf{W}^* , i.e. to minimize the function

$$\mathbf{W}^* : \min_{\mathbf{W}} \frac{1}{N} \sum_{k=1}^N (t_k - \mathcal{N}(\mathbf{x}_k, \mathbf{W}))^2, \quad (2.3)$$

where $d_k = \mathcal{N}(\mathbf{x}_k, \mathbf{W})$ is the function approximated by the NN. Once training is finished, the NN –with given number of neurons and given structure– is able to approximate the function $f(\mathbf{x})$ with the given value of the error function ε ,

$$\exists \mathbf{W}^* : \|\mathcal{N}(\mathbf{x}, \mathbf{W}^*) - f(\mathbf{x})\| < \varepsilon. \quad (2.4)$$

A trained NN is able to generalize. This means that, not only the discrete set of the training sequence can be represented, but other input–output data can be approximated which are not included in the training sequence, because the NN is a continuous function approximator.

The training can be done by any optimization technique based on the gradient method. The aim of optimization is to minimize an error function $\varepsilon = \varepsilon(\lambda)$ depending on the individual $\lambda = t - d$ values: $\partial\varepsilon/\partial\mathbf{W} = \nabla[\varepsilon] \rightarrow 0$. Weights are adapted in every iteration step k as

$$\mathbf{W}_{k+1} = \mathbf{W}_k + \Delta\mathbf{W}_k. \quad (2.5)$$

The value of $\Delta\mathbf{W}_k$ can be formulated in many ways. The backpropagation (BP) training algorithm is the most widely used one, but the faster Levenberg-Marquardt iteration technique as a modification of the BP method is preferred with the adaptation rule $\Delta\mathbf{W} = -(\mathbf{J}^T\mathbf{J} + \alpha\mathbf{I})^{-1}\mathbf{J}^T\mathbf{e}$, where \mathbf{J} is the Jacobian matrix formed by the derivatives of each error to each weight, \mathbf{I} is the unit matrix, α is the Levenberg parameter and \mathbf{e} is the error vector [99].

The operation of a MISO feedforward NN model can be expressed mathematically as

$$\mathcal{N}(\mathbf{x}, \mathbf{W}) = \psi \left(\sum_i W_i^{(L)} \psi \left(\sum_j W_{ij}^{(L-1)} \dots \psi \left(\sum_m W_{km}^{(1)} x_m \right) \right) \right), \quad (2.6)$$

where $\psi(\cdot)$ denotes the transfer functions of a PE.

Using the chain rule, the derivatives of the formulation (2.6) with respect to any input of the NN can be expressed in analytical form.

This is the general form of feedforward type NNs; although not all models share all of the characteristics. Individual neurons can have numerous inputs and can send data to numerous other PEs. There is such a large variety of NNs.

2.2 Preisach–type hysteresis models based on NN

The hysteresis phenomenon is encountered in many different areas of science, and has been in the focus of research and investigation for a long time. Thanks to the fast computers available nowadays, it is possible to simulate hysteresis characteristics more and more precisely taking into account important physical phenomena. The developed models can be inserted into field calculation software to examine an investigated material or an arrangement.

There are many hysteresis models to simulate the behavior of magnetic materials, such as the Preisach model [39, 67, 88, 93], the Jiles–Atherton model [43], the Stoner–Wohlfarth model [18, 39, 88, 93] etc., and applying a new technique, the method of NNs, which will be presented with references in this section.

The investigated NN model of magnetic hysteresis presented in this dissertation is mainly based on the ideas of the Preisach model, therefore this model with its modifications, and some methods, where the NN techniques are used are briefly described and overviewed.

2.2.1 The classical scalar Preisach model

The classical scalar Preisach model [31, 32, 39, 67, 88, 93] describes the scalar hysteresis phenomenon as a collection of elementary shifted rectangular hysteresis operators $\hat{\gamma}(\alpha, \beta)$ with different coercive fields (see Fig. 2.2). The switching fields α and β –where the magnetization jumps up from -1 to $+1$ and jumps down from $+1$ to -1 , respectively–characterize each operator. The operators also can be defined by their coercive field, $h_c = (\alpha - \beta)/2$ and their interaction field, $h_m = (\alpha + \beta)/2$. The magnetization M can be expressed by the integral

$$M(t) = \iint_{\alpha \geq \beta} \mu(\alpha, \beta) \hat{\gamma}(\alpha, \beta) H(t) d\alpha d\beta, \quad (2.7)$$

where $\mu(\alpha, \beta)$ is the Preisach distribution function, i.e. the weight function of the elementary hysteresis operators $\hat{\gamma}(\alpha, \beta)$, $H(t)$ is the applied magnetic field intensity, and $M(t)$ is the magnetization at time t . In a computer realization, the integral (2.7) is approximated by the weighted sum of elementary operators as

$$M(t) \simeq \sum_{i=1}^{N+1} \sum_{j=N+2-i}^{N+1} \mu(\alpha_i, \beta_j) \hat{\gamma}(\alpha_i, \beta_j) H(t), \quad (2.8)$$

where N is the number of subdivisions in the Preisach plane. Each point on the half space $\alpha \geq \beta$ corresponds to one elementary hysteresis operator only. In this way, a mathematical representation can be introduced and known as the Preisach triangle [39, 67],

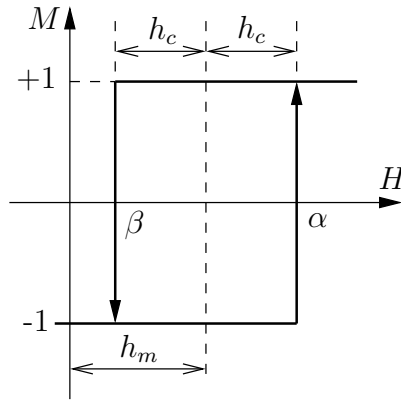


Fig. 2.2. Magnetization curve of an elementary hysteresis operator, $\hat{\gamma}(\alpha, \beta)$

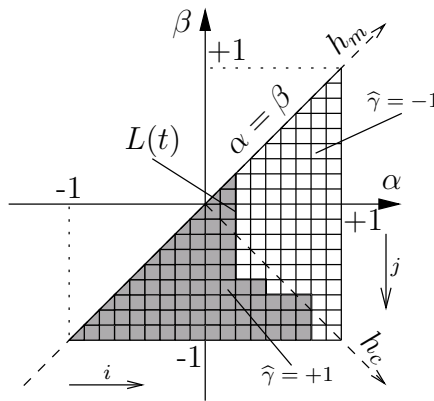


Fig. 2.3. The Preisach triangle and the staircase line

shown in Fig. 2.3. Applying the staircase line $L(t)$, the magnetization can be calculated taking into account the prehistory of the material. Increasing the magnetic field intensity, the staircase line is moving from left to right, and decreasing the magnetic field intensity, the staircase line is moving from top to bottom on the Preisach triangle switching the elementary operators, and the magnetization can be calculated by the formula (2.8). The Preisach distribution function can be easily approximated by Gaussian or exponential distribution functions, and the parameters of these distributions can be fitted to experimentally measured hysteresis curves.

Using the Everett function leads to a very favorable implementation of the Preisach model [39, 67]. The discrete Everett table must be calculated once from the measured first order reversal curves at very low frequency ($f < 1$ Hz), avoiding the computation of the integral in (2.7) or the sum in (2.8). It gives a better approximation, because the Everett function is very close to measurements,

$$E(\alpha, \beta) = \frac{1}{2}(M_\alpha - M_{\alpha, \beta}), \quad (2.9)$$

where M_α is a reversal magnetization point in the major hysteresis loop corresponding to the magnetic field intensity α , and $M_{\alpha, \beta}$ is the value of magnetization in a reversal curve starting from the reversal point (α, M_α) , when the magnetic field intensity is equal to β . A reversal curve with given points can be seen in Fig. 2.4. The Preisach distribution

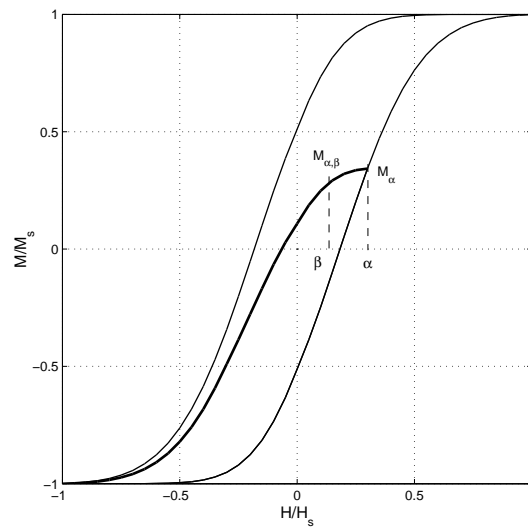


Fig. 2.4. A first order reversal curve to measure the Everett function

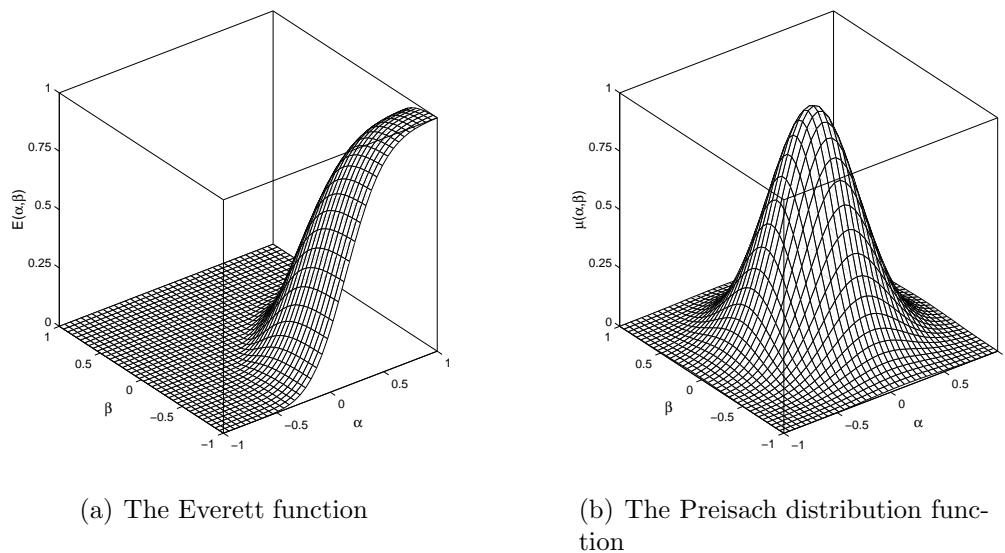


Fig. 2.5. The Everett function and the Preisach distribution function

function can be expressed from the Everett function as

$$\mu(\alpha, \beta) = \frac{\partial^2 E(\alpha, \beta)}{\partial \alpha \partial \beta}, \quad \text{and} \quad E(\alpha, \beta) = \iint_{\alpha \geq \beta} \mu(\alpha', \beta') d\alpha' d\beta'. \quad (2.10)$$

The differentiation must be performed numerically from the measured Everett function which amplifies the measurement noise. An example –generated by the Preisach model– for a calculated Everett function $E(\alpha, \beta)$ and the corresponding distribution function $\mu(\alpha, \beta)$ are plotted in Fig. 2.5(a) and in Fig. 2.5(b), respectively.

Knowing the Everett function, the following expression can be used to determine the

magnetization [67, 72]:

$$M = -E(\alpha_0, \beta_0) + 2 \sum_{k=1}^n \{E(M_k, m_{k-1}) - E(M_k, m_k)\}, \quad (2.11)$$

where $\{M_k\}_{k=1}^n$ and $\{m_k\}_{k=1}^n$ are the increasing and the decreasing sequences of the magnetic field intensity applied to the sample and stored by using the staircase line, and $\alpha_0 = 1$, $\beta_0 = -1$.

The classical scalar Preisach model is unable to describe some phenomena, such as noncongruency [39, 44, 67] and accommodation [39, 67, 94]. Simulated minor loops are congruent, i.e. a stable minor loop cycling between two fixed values of the applied field has the same size and shape. The moving model [39, 72] and the product model [39, 45] can solve this problem. The moving model contains the classical Preisach model with a feedback which modifies the actual value of the applied magnetic field intensity by a term of αM , i.e. $H_k = H_k + \alpha M_{k-1}$ at the discrete time of simulation t_k , and α is a small positive number. In the product model, the rate of change of magnetization with respect to the applied field dM/dH is expressed by a Preisach-like integral formula multiplied by a function $R(M)$. Accommodation of a loop means that, it takes many cycles for a minor hysteresis loop to stabilize and it continues until an equilibrium is reached asymptotically. The moving model and the product model also can fulfill this property. Accommodation cannot be simulated by the classical Preisach model, because a minor loop closes at the same point (H, M) , where it was started. This is caused by the wiping-out property.

2.2.2 The classical scalar Preisach model via NNs

The memory storage mechanism of the ferromagnetic materials can be described by means of the Preisach triangle. Several papers have been written about this approach when using NNs.

The authors of [84] used a discrete set of Play operators $\Psi_j = \Psi(t, h_c^j)$, $j = 0, \dots, J-1$ to simulate the memory mechanism of magnetic materials and a feedforward NN to store the experimentally measured data set $B = \mathcal{H}_B\{\Psi(t, h_c^j)\}$. The block diagram of this model can be seen in Fig. 2.6. The authors have considered a NN with $J = 20$ inputs and one hidden layer with 40 neurons. Each neuron employs a bipolar sigmoidal activation function. The training data set has contained 50 $H - B$ pairs in a nested loop. Five first order reversal curves have been measured in one magnetic sample and seven in another sample. They have demonstrated the good quality of the predictions of the model by comparing simulation results and measured symmetrical minor loops. This model has also been applied to simulate noisy and incomplete measurement data [98]. It is very difficult to identify the classical Preisach model when the reversal curves have been loaded with noise, but NNs are able to filter the noise during the learning process. Preprocessing of noisy measured data is not required in this case.

A possible way to represent the main features of the classical scalar Preisach model applying NNs can be found in [1]. The block representation of the Preisach model has been realized by a NN structure with bipolar sigmoidal activation function, if the hysteresis operators are represented by elementary rectangular loops $\hat{\gamma}(\alpha, \beta)$, and the distribution function $\mu(\alpha, \beta)$ has been characterized by the weights of the network as illustrated in Fig. 2.7. This means that, a large number of inputs (few hundred), and

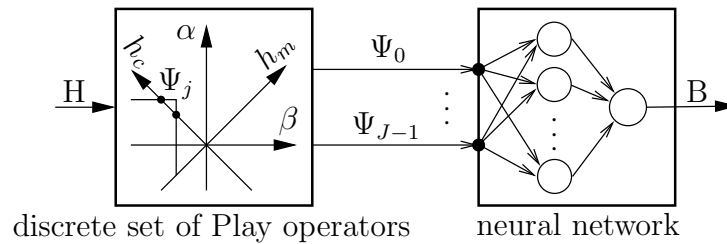


Fig. 2.6. Implementation via feedforward NN of the system with Preisach memory

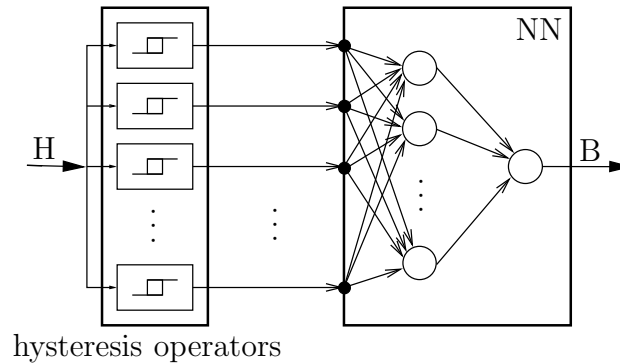


Fig. 2.7. Operator NN realization of the classical Preisach model

consequently a large number of unknown weights are required for the model, so the authors have grouped the rectangular operators into a smaller, but more sophisticated set of 20 hysteresis operators having different widths and 10 neurons in one hidden layer. The measured data set contains 304 $H - B$ pairs in the form of a decreasing oscillating sequence. After training, higher order minor loops are demonstrated and compared with measured data.

The approximation of the Preisach distribution function or the Everett function can be realized by a feedforward NN with 2 inputs (α and β) and one output ($\mu(\alpha, \beta)$ or $E(\alpha, \beta)$) [23]. The output of a NN having continuous and differentiable activation functions can be differentiated with respect to its input, and the value of the differential susceptibility $\chi_{diff} = dM/dH$ is a continuous function of H and it can be expressed in analytical form. Applying the Newton–Raphson iteration technique in numerical field calculation problems leads to faster convergence, but this technique requires the differential susceptibility. It is also shown in the paper that, the integral form (2.7), as well as the energy losses can also be worked out by an analytical expression when NNs are used. It gives a computationally effective model. The authors used a NN with 75 neurons in one hidden layer to approximate a measured Everett surface with very good accuracy.

NN technique combined with the Fourier description can be used to calculate the magnetization in cases when a periodic magnetic field excites the ferromagnetic device as presented in [80]. This method is a quite simple computational instrument for designers and takes into account the frequency dependence of the hysteresis characteristics.

A nonlinear circuit model of hysteresis characteristics can be developed as proposed in [20]. The investigated model is based on a two-layer feedforward connected nonlinear circuit. The first layer contains elementary cells (simple hysteresis operators) and the second layer is a simple adder. The parameter identification of this model can be solved

by a NN approach. The proposed model has been compared with the Jiles–Atherton hysteresis model and a good agreement has been found, including the dynamic properties (e.g. frequency dependence) of the hysteresis loop.

The dynamic Preisach model which encompasses the dynamic effects such as the eddy currents and the domain wall displacement is a generalization of the static Preisach model introducing the rate of change of the magnetization dM/dt [30, 39, 67], i.e.

$$M(t) = \iint_{\alpha \geq \beta} \mu(\alpha, \beta, dM/dt) \hat{\gamma}(\alpha, \beta) H(t) d\alpha d\beta. \quad (2.12)$$

The rate dependent generalization of the Preisach model considers the hysteresis switches to be not ideal ones [5], but their output changes at a finite rate, so ideal rectangular hysterons are changed to idealized magnetization characteristic. The disadvantage of this model is the time consuming calculation of the output.

This effect can also be handled by the classical Preisach model coupled with a differential equation as shown in [30]. The differential equation responsible for the dynamic features uses a variable H_m as input for the static Preisach model delayed with respect to the actual field strength H is

$$\frac{dH_m}{dt} = a(H - H_m) - b \frac{dB}{dt} + c \frac{dH}{dt}, \quad (2.13)$$

where dH/dt and dB/dt are the magnetic field intensity and the magnetic flux density variation rates and a , b and c are model parameters, adjusted by an iterative method.

A recurrent NN can be used to handle time dependent mapping. The authors of [79] used the Elman type recurrent NN which is a three-layer recurrent network. The middle layer is recurrent containing hidden and context neurons. The context neurons act as a delay in one sampling period, meaning that, the magnetization is a function of the present state, the previous state and the present magnetic field intensity. The network was trained using two symmetrical hysteresis loops and tested with another loop different from the training sequence. The simulation results agree well with the experimental measurements, but minor loops are not shown in the paper.

I have developed a new NN based hysteresis operator which differs from the above models (Chapter 3). Measured curves are approximated by NNs, the memory mechanism of the model is based on a knowledge-base containing the properties of the hysteresis characteristics as if-then rules.

2.2.3 Vector hysteresis modeling

Scalar hysteresis characteristics can simulate special cases, when the magnetic field intensity and the magnetization vectors are in the same direction (e.g. inside a toroidal shape core), but generally, these vectors do not have the same directions. In this case, a vector hysteresis model must be used.

The Stoner–Wohlfarth model is the most successful physics-based model, because a graphical representation by means of an astroid can be used to follow the magnetization vector in the presence of a two-dimensional magnetic field intensity [5, 39, 88, 93]. The anisotropic behavior is embedded in the equations of the model, but the identification process is a difficult task.

The most widely used vector model is proposed by Mayergoyz [67]. This is an extension of the classical Preisach model, because this vector model is built as a superposition of continuously distributed scalar Preisach models in given directions \mathbf{e}_φ of the 2D plane. The magnetization vector \mathbf{M} can be expressed in two dimensions as

$$\mathbf{M} = \int_{-\pi/2}^{\pi/2} \mathbf{e}_\varphi \mathcal{H}\{H_\varphi\} d\varphi, \quad (2.14)$$

where $M_\varphi = \mathcal{H}\{H_\varphi\}$ is the scalar magnetization in the direction \mathbf{e}_φ . The characteristic $\mathcal{H}\{\cdot\}$ depends on the polar angle φ if the magnetic material presents anisotropy, otherwise it is φ -independent [10, 67, 77, 78].

The identification process can be worked out by applying either the Everett function or the Preisach distribution function both for isotropic and anisotropic case. The identification process is based on the integral equation

$$F(\alpha, \beta) = \int_{-\pi/2}^{\pi/2} \cos \varphi E(\alpha \cos \varphi, \beta \cos \varphi) d\varphi, \quad (2.15)$$

where $F(\alpha, \beta)$ and $E(\alpha, \beta)$ are the measured scalar Everett function and the unknown vector Everett function. The identification process based on the Preisach distribution function can also be applied, i.e.

$$\mu(\alpha, \beta) = \int_{-\pi/2}^{\pi/2} \cos^3 \varphi \nu(\alpha \cos \varphi, \beta \cos \varphi) d\varphi, \quad (2.16)$$

where $\mu(\alpha, \beta)$ and $\nu(\alpha, \beta)$ are the measured scalar distribution function and the unknown vector distribution function. These integral equations can be solved only numerically, because no analytical solution is available, that is why the Preisach triangle must be divided into elements.

The above integral equations are valid for isotropic characterization for simplicity. A possible solution composed with the Preisach distribution function of an anisotropic material with the help of Fourier expansion can be found in [78].

Working out a vector hysteresis measurement system is an extensive project [34, 64, 85, 86], therefore, it is sometimes simpler to use a known model to generate measurements.

A vectorial realization based on NN technique has been investigated and performed in [2]. After some mathematical formulations of the basic equations of the anisotropic 2D vector Preisach model and applying Fourier expansion, the vector Preisach model can be identified by a two layer feedforward type NN. The input layer consists of twice as many nodes as the number of elementary hysteresis operators necessary to construct a reasonably accurate hysteresis model. Only 36 rectangular elementary hysteresis operators have been used in the model. The identification of the model is based on 706 $H - M$ pairs. Measured first order reversal curves have been compared with predictions of the model.

I have worked out an original identification method based on the measured Everett function to simulate both isotropic and anisotropic magnetic materials. A possible generalization for 3D also will be presented in Chapter 3, however, only two-dimensional anisotropic vector models are known from the literature.

2.3 The nondestructive testing method

Structural damage may result from a number of causes and it can be of different types. It is most often called crack which is a change in the geometry with respect to the uncracked state of the structure. Early stages of cracks may be undetectable, but cracks may grow and propagate at a very high rate quickly compromising the structural integrity. Detection of cracks is the main goal of the damage detection systems under design [46,81].

There are two main groups of testing of materials in the industry, destructive and nondestructive testing methods.

In the first case, a sample from the analyzed structure must be taken and examined in a laboratory. After making a standardized test specimen (with given size and shape) from the sample, some measurements can be done, such as the hardness test, the Charpy's striking-bending test, tensile strength test, measuring different electrical properties and so on [76].

In nondestructive testing (NDT), the tested material is not damaged [46,81], but it needs more precise measuring equipments controlled by computers. Thanks to the intense advance in computer techniques, these methods have an extreme advance nowadays researched by many engineers. Using computers and electronic control in NDT systems allows to reduce operator workload and improves the speed and quality of the process. Of course, it requires extensive software development, too. The reason for this extensive work is that, products of standardized production must satisfy increasingly rigorous criteria. Monitoring can be worked out by fast and precise measuring arrangements. The automation of NDT techniques and procedures is beginning to spread among different industries and fields of engineering. The benefits of automated NDT include more reliable and more predictable operation machinery, decreased probability of industrial accidents and less operation costs.

There are several major directions of such methods. For example the X-ray method is the first flaw detection technique, the UV optical technique with digital image processing methods, measuring with electronmicroscope, the ultrasonic test [95]. I mainly focus on the magnetic flux leakage method [46]. In short, the basis of the magnetic flux leakage method is that, inhomogenities (like cracks, slots and flaws) change the generated homogeneous field distribution inside the material, and this field perturbation can be measured by an appropriate sensor. The specimen can be magnetized either by passing a direct current through it or by applying an external magnetic field. It is easy to understand that, the surface cracks can be identified much easier than cracks lying inside the material, because flux lines disperse to the area surrounding the defect, but this problem can be handled by choosing an appropriate frequency or amplitude of the excitation. It is also hard to find a crack parallel to the magnetic flux. Much better results can be obtained when two separate and perpendicular magnetization fields are used, because cracks with any orientation can be detected then.

The other general magnetization process found in the literature is to move an exciting coil above the specimen generating a magnetic field intensity. The leakage field modified by the eddy currents inside the material can be measured then. This method is limited by the skin effect only to thin and non-magnetic structural components. A possible alternative is the use of pulse eddy currents [12,15,74], when the rich harmonic component of a pulse accounts for a multi-frequency analysis, since the lower harmonics penetrating deeper into the structure.

An increasing number of articles about nondestructive testing (e.g. [13, 14, 28, 37, 71, 74, 95, 96] and so on) can be found in books, proceedings and journals in recent years. There are many sensors [15, 28, 33, 37, 69–71, 75, 96, 97], measuring arrangements and visualization techniques described in the literature. There are two main groups of probes: measuring the changes in coil impedance, and measuring induced voltages. The measuring test arrangement consists of a test specimen with artificial cracks, a positioning device which is used to scan the surface by moving the probe above the test specimen and a computer to control the measuring system and to store the measured data.

The applied simulation techniques are mainly based on the finite element method with different potential formulations. Modeling natural cracks is a long-standing and difficult task, let us think about pits caused by corrosion, hairline cracks with varying shape and depth, flaws and so on [89]. Such natural cracks can be found in real industrial environment. It is in the scope of interest of many projects to form the complicated profiles of natural cracks, but in computation it is obvious to use simply characterized cracks of elliptical, semielliptical or rectangular shape. The simplest model is to discretize the geometry by finite elements and to assign the same material properties to crack as to the air region.

Visualization, as well as recognition and identification of damage are also important stages in NDT techniques [3, 14, 69, 70, 74, 92, 103, 104]. The recognition is an inverse problem. It should be performed automatically with high reliability. In the field of recognition and classification of computational intelligence (as fuzzy systems, neural networks, neuro-fuzzy systems, knowledge-based systems) there is an increasing challenge and revival of learning. It is the main direction of research which replaces the statistical and traditional methods.

A search of literature (IEEE Transactions on Magnetics, Electromagnetic Nondestructive Evaluation, Applied Electromagnetics and Mechanics in the frame of Studies in Applied Electromagnetics and Mechanics, and Proceedings of Conferences) show a wide and increasing area of automated NDT applications. There are several benchmark problems aimed at working out the common standards and solvers, to compare different numerical techniques. This activity shows the increasing importance of this field.

2.4 Formulation and potentials of the electromagnetic field problems

An electromagnetic field calculation problem can be characterized by the field intensities and the flux densities described by partial differential equations derived from Maxwell's equations and boundary conditions [6, 21, 29, 40, 41, 87]. There are several potential formulations applicable to calculate the field quantities, fundamentally using scalar and vector potentials. In this section, I briefly overview only the most popular formulations used in the simulation of nondestructive testing methods in connection with the Finite Element Method (FEM) [6, 7, 16, 68, 90, 91], especially with the edge element based FEM. Essentially, NDT represents an eddy current field problem.

At low frequencies and with normal conducting materials used in NDT techniques, the displacement currents are small compared with the conductive currents and can be neglected. Consequently, the studied electromagnetic field can be described by the

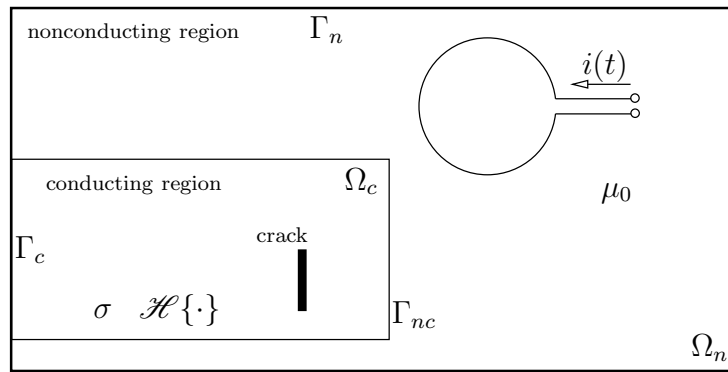


Fig. 2.8. Structure of an eddy current problem, crack is located in the conducting region

quasi-static Maxwell's equations written in differential form as

$$\nabla \times \mathbf{H} = \mathbf{J}, \quad (2.17)$$

$$\nabla \times \mathbf{E} = -\partial \mathbf{B} / \partial t, \quad (2.18)$$

$$\nabla \cdot \mathbf{B} = 0, \quad (2.19)$$

$$\mathbf{B} = \mathcal{H}\{\mathbf{H}\}, \quad (2.20)$$

$$\mathbf{J} = \mathbf{J}_0 + \sigma \mathbf{E}, \quad (2.21)$$

where \mathbf{H} and \mathbf{E} are the magnetic and the electric field intensities, \mathbf{B} is the magnetic flux density, \mathbf{J} is the total current density and \mathbf{J}_0 represents the current density of the exciting current. The symbol $\mathcal{H}\{\cdot\}$ represents the hysteresis characteristic of the magnetic material and σ is the conductivity of the investigated material. The hysteresis operator can be a linear or nonlinear and/or hysteretic relation depending on the analyzed material.

A typical structure of an eddy current field problem (object of NDT) can be seen in Fig. 2.8. A current excitation $i(t)$ (or a current density \mathbf{J}_0) with given waveform is placed into the nonconducting region Ω_n (where μ_0 is the vacuum permeability), the eddy current distribution is unknown in the conducting material Ω_c . Maxwell's equations are valid in the problem region $\Omega = \Omega_c \cup \Omega_n$.

The boundary conditions of the problem can be given at the artificial far boundaries of the nonconducting region Γ_n , where homogeneous boundary conditions are assumed, i.e. the tangential component of the magnetic field intensity or the normal component of the magnetic flux density is zero, $\mathbf{H} \times \mathbf{n} = \mathbf{0}$ or $\mathbf{B} \cdot \mathbf{n} = 0$, where \mathbf{n} is the outer normal unit vector of the region. Homogeneous boundary conditions can be supposed along the symmetry planes (a part of Γ_n and Γ_c): $\mathbf{H} \times \mathbf{n} = \mathbf{0}$, i.e. $\mathbf{J} \cdot \mathbf{n} = 0$ and $\mathbf{E} \times \mathbf{n} = \mathbf{0}$. On the interface between the conducting and the nonconducting regions Γ_{nc} , the interface conditions must be satisfied: $\mathbf{H} \times \mathbf{n}$ and $\mathbf{B} \cdot \mathbf{n}$ must be continuous and $\mathbf{J} \cdot \mathbf{n} = 0$.

There are several potential formulations that can be used to solve a problem [6, 21, 29, 40, 41, 87].

The static magnetic field in the eddy current free region (air) can be described by the magnetic scalar potential Ψ or by the magnetic vector potential \mathbf{A} . The magnetic scalar potential is defined by

$$\mathbf{H} = \mathbf{T}_0 - \nabla \Psi, \quad (2.22)$$

where the impressed field quantity \mathbf{T}_0 can be applied to consider the current density of the current source \mathbf{J}_0 , that is $\nabla \times \mathbf{T}_0 = \mathbf{J}_0$, because $\nabla \cdot \mathbf{J}_0 = 0$. It is better to

find an approximating vector potential \mathbf{T}_0 to take into account the effect of the exciting current, than generating a mesh for \mathbf{J}_0 , since it leads to a consistent right hand side of the equations, moreover the exact modeling of the coils can be avoided. The magnetic scalar potential is approximated by nodal shape functions, \mathbf{T}_0 can be represented by the aid of edge basis functions.

The magnetic vector potential is defined by

$$\mathbf{B} = \nabla \times \mathbf{A} \quad (2.23)$$

which satisfies (2.19) exactly. The magnetic vector potential can be approximated by nodal or edge shape functions as well, depending on the dimension of the problem. The reduced vector potential \mathbf{A}_r , approximated by edge shape functions can be applied more efficiently if current sources are present, since the right hand side of the assembled equation is then consistent. The reduced vector potential can be introduced as

$$\mathbf{B} = \mu_0 \mathbf{H}_s + \nabla \times \mathbf{A}_r, \quad (2.24)$$

where \mathbf{H}_s is the Biot–Savart field of the exciting current flowing in the exciting coils.

The use of the magnetic scalar potential in eddy current free region reduces the computational costs as compared with the use of the magnetic vector potential, because Ψ has only one component, and \mathbf{A} has three components, when using nodal shape functions. Furthermore, the use of \mathbf{A} requires the inclusion of the coils in the mesh increasing the number of unknowns. A simpler mesh can be generated by using the vector field of \mathbf{T}_0 .

Two potential functions can be used in the eddy current region, either a current vector potential \mathbf{T} or a magnetic vector potential \mathbf{A} . The current vector potential approximated by edge shape functions can be applied more effectively when thin flaws in the conducting material are present [7]. The current vector potential is introduced as [6]

$$\mathbf{H} = \mathbf{T}_0 + \mathbf{T} - \nabla \Psi. \quad (2.25)$$

The magnetic vector potential can be applied in several ways: the \mathbf{A}^* -formulation, the \mathbf{A}, V -formulation, and the \mathbf{A}_r, V -formulation and some other combinations of the potentials as presented in [6].

The various formulations in the conducting and nonconducting regions must be coupled through the interface conditions. In my research work, I used the $\mathbf{T}, \Psi - \Psi$ formulation. In this case, Ψ is approximated by nodal shape functions, \mathbf{T} and \mathbf{T}_0 are approximated by edges shape functions, Ψ and \mathbf{T}_0 are defined in the whole region Ω , and \mathbf{T} is defined only in the conducting region Ω_c .

2.5 The finite element method

By using potentials, Maxwell's equations can be transformed into partial differential equations and they can be solved by numerical methods. The basis of numerical techniques is to reduce the partial differential equations to algebraic equations whose solution gives the unknown potentials in the given points of a mesh. This reduction can be done by discretizing the partial differential equations in time and in space as well. The potential functions, the approximation method and the generated mesh distinguish the numerical

field solvers. There is a number of methods, e.g. the finite element method, the finite difference method, the boundary element method, the integral equation method and the global variational method [40, 41].

The FEM is the most popular and flexible numerical technique to determine the approximate solution of partial differential equations in engineering [8, 21, 35, 82, 105]. The fundamental idea of the FEM is to divide the problem region to be analyzed into smaller finite elements with given shape (e.g. triangles in 2D or tetrahedra in 3D). The scalar potential functions can be approximated by nodal shape functions, and the vector potential functions can be approximated by either nodal or vector shape functions. A shape function is a simple continuous polynomial function defined in a finite element. Applying first-order nodal and edge shape functions, the unknown potentials can be associated with the nodes as well as the edges of the finite element mesh. Shape functions are described below in this section.

The finite element analysis consists of four main steps. The first step is to work out a simplified mathematical model of the arrangement which is adequate to calculate electromagnetic field quantities. There may be some details that can be neglected or simplified, e.g. the symmetry of the equipment can be taken into account. This cannot be automated, it is advisable to build a problem specific model. The preprocessing task is the second step when the geometry, the material parameters, the excitation waveform, etc. must be given and then the finite element mesh can be generated. The next step is the calculation, generation of the element based equations, assembling of the global system of linear equations, and the solution of the assembled equations must be performed. The last step is the postprocessing, when calculated results are plotted and shown, quantities of interest (e.g. capacity, losses) are calculated. There are some feedbacks during FEM calculations, for example to make a denser mesh, to vary time steps and so on. If the problem to be solved is nonlinear, then an iterative feedback must be used during the third step of calculations.

In my research, I used the first-order nodal and edge shape functions which vary linearly in a finite element to determine the magnetic field intensity above a test specimen with well defined surface cracks (slots and holes with different, but well defined size). A problem not easily treated by nodal finite elements arises, when singularities are to be approximated at sharp corners, for example at cracks in a conducting material. This is the reason why I used the combined nodal and edge finite elements.

My work is mainly based on the papers [6, 36, 66] and on the dissertation [21]. In the followings, I briefly describe the nodal and edge finite elements, following the above literature.

2.5.1 Nodal finite elements

Scalar potential functions can be represented by a linear combination of shape functions associated with nodes of the finite element mesh. Within a finite element, a scalar potential function $\Psi = \Psi(\mathbf{r}, t)$ is approximated by $\Psi_h = \Psi_h(\mathbf{r}, t)$ as

$$\Psi_h \simeq \sum_{i=1}^I N_i \Psi_i, \quad (2.26)$$

where $N_i = N_i(\mathbf{r})$ and $\Psi_i = \Psi_i(t)$ are the first-order nodal shape functions and the value of potential function corresponding to the i^{th} node. The number of degrees of freedom

is $I = 3$ in a 2D problem using triangular FEM mesh and $I = 4$ in a 3D arrangement meshed by tetrahedral elements.

The sum of all nodal shape functions is equal to 1, $\sum_{i=1}^I N_i = 1$, hence the sum of their gradients is zero, $\sum_{i=1}^I \nabla N_i = 0$. This means that, the maximal number of linearly independent gradients of the nodal basis functions is $I - 1$. The shape functions are presented in the sections 2.5.3 and 2.5.4.

2.5.2 Edge finite elements

Vector potentials can be represented by nodal shape functions as well. The natural approach is to treat the vector field $\mathbf{T} = \mathbf{T}(\mathbf{r}, t)$ as two (in 2D) or three (in 3D) coupled scalar fields, T_x , T_y and T_z . Scalar shape functions can be used again, i.e. each node has two (2D) or three (3D) unknowns, and scalar shape functions can be used. For example in 3D, \mathbf{T} can be approximated by $\mathbf{T}_h = \mathbf{T}_h(\mathbf{r}, t)$ as

$$\mathbf{T}_h \simeq \sum_{i=1}^I (T_{x,i} \mathbf{e}_x + T_{y,i} \mathbf{e}_y + T_{z,i} \mathbf{e}_z) N_i. \quad (2.27)$$

Instead of scalar shape functions, I used vector shape functions

$$\mathbf{T}_h \simeq \sum_{k=1}^K \mathbf{W}_k T_k, \quad (2.28)$$

where $\mathbf{W}_k = \mathbf{W}_k(\mathbf{r})$ and $T_k = T_k(t)$ are the first-order edge shape functions and the degree of freedom is associated to the edges. The number of degrees of freedom is $K = 3$ in 2D when applying triangular mesh and $K = 6$ in the 3D case by applying tetrahedral finite elements. The shape functions are also presented in the sections 2.5.3 and 2.5.4.

I used linear elements [21], having only K unknowns in each finite element, one attached to each edge. They allow the normal component of the field to be free to jump at each facet of the element. The direction of the edges must be defined by the global mesh, but the equations of one element assume a local orientation.

The line integral of the shape functions \mathbf{W}_k along the k^{th} edge is equal to one, meaning that the line integral of the vector potential along this edge is T_k ,

$$\int_{l_k} \mathbf{T}_h \cdot d\mathbf{l} = \int_{l_k} (\mathbf{W}_k T_k) \cdot d\mathbf{l} = T_k. \quad (2.29)$$

This means that, the value of T_k along an edge of a finite element is equal to the value of T_k along the edge of another finite element if these finite elements share the edge. Therefore the vector function \mathbf{T} is tangentially continuous across all element interfaces, but its normal component is not.

The gradients of the nodal shape functions are in the function space spanned by the edge basis functions, that is

$$\nabla N_i = \sum_{k=1}^K c_{ik} \mathbf{W}_k, \quad i = 1, \dots, I - 1, \quad (2.30)$$

where $\sum_{k=1}^K c_{ik}^2 > 0$. Taking the curl of each equation in (2.30) results in

$$\sum_{k=1}^K c_{ik} \nabla \times \mathbf{W}_k = \mathbf{0}, \quad i = 1, \dots, I - 1. \quad (2.31)$$

This shows that, the maximal number of linearly independent curls of the edge basis functions is $K - (I - 1)$. The interdependence of the curls of the edge basis functions means that, an ungauged formulation leads to a singular, positive semidefinite finite element curl–curl matrix. Singular systems can be solved by iterative methods, if the right hand side of the system of equations is consistent.

2.5.3 FEM in 2D using linear shape functions

I used a finite element mesh with triangular finite elements. Linear basis functions can be introduced by using the barycentric coordinate system in a finite element. The area of a triangle is denoted by Δ , and it can be calculated as

$$\Delta = \frac{1}{2} \begin{vmatrix} 1 & x_1 & y_1 \\ 1 & x_2 & y_2 \\ 1 & x_3 & y_3 \end{vmatrix},$$

where (x_1, y_1) , (x_2, y_2) and (x_3, y_3) are the coordinates of the three nodes of the triangle in the global coordinate system building an anticlockwise sequence. The area functions (see Fig. 2.9) of a given point inside the triangle with coordinates (x, y) can be calculated as

$$\Delta_1 = \frac{1}{2} \begin{vmatrix} 1 & x & y \\ 1 & x_2 & y_2 \\ 1 & x_3 & y_3 \end{vmatrix}, \quad \Delta_2 = \frac{1}{2} \begin{vmatrix} 1 & x_1 & y_1 \\ 1 & x & y \\ 1 & x_3 & y_3 \end{vmatrix}, \quad \Delta_3 = \frac{1}{2} \begin{vmatrix} 1 & x_1 & y_1 \\ 1 & x_2 & y_2 \\ 1 & x & y \end{vmatrix}.$$

Three linear shape functions N_i can be described by the above area functions as

$$N_i = \Delta_i / \Delta, \quad i = 1, 2, 3. \quad (2.32)$$

A shape function N_i is equal to 1 at the i^{th} node of the triangle, and equal to zero at the other two nodes and varies linearly over the triangle. If the potentials at the nodes are known, then a linear approximation of the potential function can be represented by (2.26).

The gradients of the basis functions are used to assemble the global system of equations, and the constant gradients of linear shape functions can be calculated as

$$\begin{aligned} \nabla N_1 &= \{(y_2 - y_3) \mathbf{e}_x + (x_3 - x_2) \mathbf{e}_y\} / 2\Delta, \\ \nabla N_2 &= \{(y_3 - y_1) \mathbf{e}_x + (x_1 - x_3) \mathbf{e}_y\} / 2\Delta, \\ \nabla N_3 &= \{(y_1 - y_2) \mathbf{e}_x + (x_2 - x_1) \mathbf{e}_y\} / 2\Delta. \end{aligned} \quad (2.33)$$

Whitney complex

The first–order (linear) edge basis functions can be generated by means of the Whitney complex, briefly described here, the extensive mathematical background can be found in [9, 21].

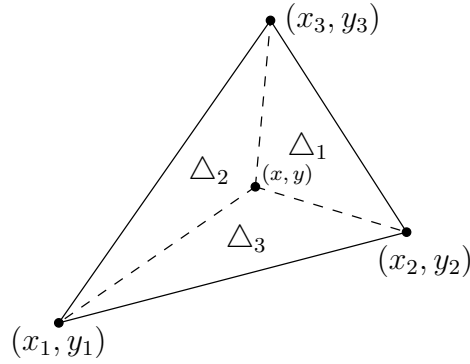


Fig. 2.9. The barycentric coordinates in 2D

The Whitney complex can be described as finite element bases for differential forms and it consists of a family of piecewise polynomial differential forms. Differential forms are fields of alternating multilinear mappings from \mathbb{R}^p to \mathbb{R} , and only forms of degree $p = 0, 1, 2, 3$ are considered and stand for vertices, edges, facets and tetrahedra. These forms are known as p -forms or Whitney forms. If $p = 0$ or $p = 3$, then they correspond to scalar functions, if $p = 1$ or $p = 2$, then to vector functions.

The Whitney forms in 3D are constructed as follows: consider a vertex i and a point x belonging to one of the tetrahedra which share vertex i , let N_i be the barycentric weight of x in its tetrahedron with respect to vertex i . The Whitney form associated with any p -simplex is defined as

$${}^p w_{i_0, \dots, i_p} = p! \sum_{j=0}^p (-1)^j N_{i_j} d^0 N_{i_0} \times \dots \times d^0 N_{i_p}, \quad (2.34)$$

where the differential operator d stands for

$$\begin{aligned} d^0 \phi &= (\nabla \phi) && \rightarrow \text{for } p = 0, \\ d^1 \mathbf{u} &= (\nabla \times \mathbf{u}) && \rightarrow \text{for } p = 1, \\ d^2 \mathbf{u} &= (\nabla \cdot \mathbf{u}) && \rightarrow \text{for } p = 2, \end{aligned} \quad (2.35)$$

and for $p = 3$, set $d^3 \phi = 0$. The expressions ϕ and \mathbf{u} are arbitrary scalar and vector functions in the problem region.

The lowest order Whitney element can be obtained when $p = 0$, i.e. $w_i = N_i$, the nodal shape function. If $p = 1$, and providing that i and j are vertices of an edge, then equation (2.34) gives the 1-form, the linear edge basis function, $\mathbf{w}_{ij} = N_i \nabla N_j - N_j \nabla N_i$. By applying the Whitney form, 2D vector basis functions \mathbf{W}_i can be calculated by using the nodal shape functions,

$$\begin{aligned} \mathbf{W}_1 &= (N_1 \nabla N_2 - N_2 \nabla N_1) \delta_1 = W_{1,x} \mathbf{e}_x + W_{1,y} \mathbf{e}_y, \\ \mathbf{W}_2 &= (N_2 \nabla N_3 - N_3 \nabla N_2) \delta_2 = W_{2,x} \mathbf{e}_x + W_{2,y} \mathbf{e}_y, \\ \mathbf{W}_3 &= (N_3 \nabla N_1 - N_1 \nabla N_3) \delta_3 = W_{3,x} \mathbf{e}_x + W_{3,y} \mathbf{e}_y. \end{aligned} \quad (2.36)$$

The edge basis function \mathbf{W}_i ($i = 1, 2, 3$) has tangential component only along the i^{th} edge and it is perpendicular to the other two edges as represented in Fig. 2.10(a)–2.10(c). It is easy to see that, an edge shape function has magnitude and direction. In linear edge functions, the value of δ_i is equal to ± 1 , depending on whether the local direction of the edge is the same as the global direction or opposite (see Fig. 2.11).

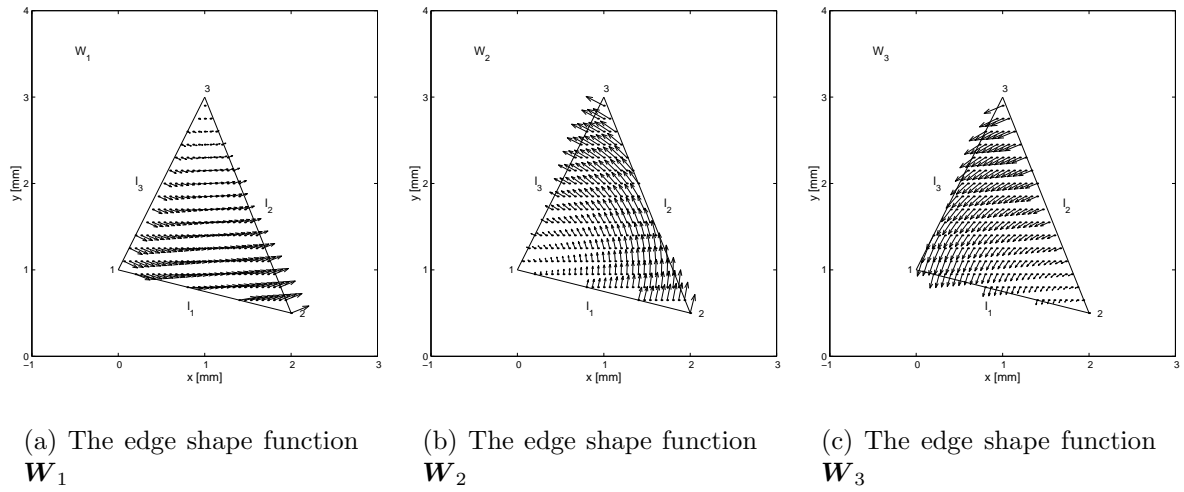


Fig. 2.10. The 2D edge shape functions

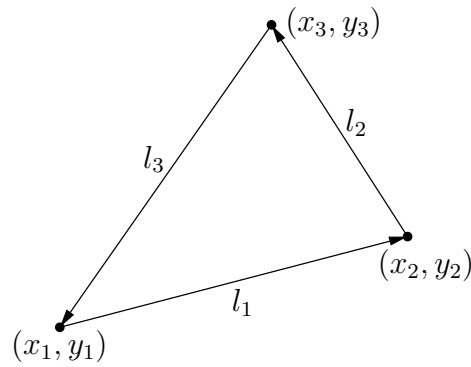


Fig. 2.11. The definition of edges with local directions of the triangular finite element

In eddy current field problems the curl vector of the edge basis functions must be applied, that is

$$\nabla \times \mathbf{W}_i = \begin{vmatrix} \mathbf{e}_x & \mathbf{e}_y & \mathbf{e}_z \\ \partial/\partial x & \partial/\partial y & 0 \\ W_{i,x} & W_{i,y} & 0 \end{vmatrix} = \mathbf{e}_z \left\{ \frac{\partial W_{i,y}}{\partial x} - \frac{\partial W_{i,x}}{\partial y} \right\}, \quad (2.37)$$

and explained as

$$\begin{aligned} \nabla \times \mathbf{W}_1 &= 2(\nabla N_1 \times \nabla N_2), \\ \nabla \times \mathbf{W}_2 &= 2(\nabla N_2 \times \nabla N_3), \\ \nabla \times \mathbf{W}_3 &= 2(\nabla N_3 \times \nabla N_1). \end{aligned} \quad (2.38)$$

The curl vector of linear edge shape functions is constant in a finite element, because of the constant value of the gradients of the linear nodal shape functions.

2.5.4 FEM in 3D using linear shape functions

Linear basis functions can be introduced again by using the barycentric coordinate system. The volume of a tetrahedron is denoted by V , and it can be expressed as

$$V = \frac{1}{6} \begin{vmatrix} x_4 - x_1 & y_4 - y_1 & z_4 - z_1 \\ x_4 - x_2 & y_4 - y_2 & z_4 - z_2 \\ x_4 - x_3 & y_4 - y_3 & z_4 - z_3 \end{vmatrix},$$

where (x_1, y_1, z_1) , (x_2, y_2, z_2) , (x_3, y_3, z_3) and (x_4, y_4, z_4) are the coordinates of the four nodes of the tetrahedron as shown in Fig. 2.12. The volume functions according to a given point inside the tetrahedron with coordinates (x, y, z) can be calculated as

$$V_1 = \frac{1}{6} \begin{vmatrix} x_4 - x & y_4 - y & z_4 - z \\ x_4 - x_2 & y_4 - y_2 & z_4 - z_2 \\ x_4 - x_3 & y_4 - y_3 & z_4 - z_3 \end{vmatrix},$$

$$V_2 = \frac{1}{6} \begin{vmatrix} x_4 - x_1 & y_4 - y_1 & z_4 - z_1 \\ x_4 - x & y_4 - y & z_4 - z \\ x_4 - x_3 & y_4 - y_3 & z_4 - z_3 \end{vmatrix},$$

$$V_3 = \frac{1}{6} \begin{vmatrix} x_4 - x_1 & y_4 - y_1 & z_4 - z_1 \\ x_4 - x_2 & y_4 - y_2 & z_4 - z_2 \\ x_4 - x & y_4 - y & z_4 - z \end{vmatrix},$$

$$V_4 = \frac{1}{6} \begin{vmatrix} x - x_1 & y - y_1 & z - z_1 \\ x - x_2 & y - y_2 & z - z_2 \\ x - x_3 & y - y_3 & z - z_3 \end{vmatrix}.$$

Four linear shape functions N_i correspondingly to the four nodes are

$$N_i = V_i/V, \quad i = 1, 2, 3, 4. \quad (2.39)$$

A shape function N_i is equal to 1 at the i^{th} node of the tetrahedron, moreover it is equal to zero at the other three nodes and varying linearly within the tetrahedron. If potentials at the nodes are known, then a linear approximation of the potential function can be represented by (2.26).

The gradients of such linear basis functions are constant and can be calculated as

$$\begin{aligned} \nabla N_1 &= \left\{ [z_2(y_3 - y_4) + z_3(y_4 - y_2) + z_4(y_2 - y_3)] \mathbf{e}_x \right. \\ &\quad + [x_2(z_3 - z_4) + x_3(z_4 - z_2) + x_4(z_2 - z_3)] \mathbf{e}_y \\ &\quad \left. + [y_2(x_3 - x_4) + y_3(x_4 - x_2) + y_4(x_2 - x_3)] \mathbf{e}_z \right\} / 6V, \\ \nabla N_2 &= \left\{ [z_1(y_4 - y_3) + z_3(y_1 - y_4) + z_4(y_3 - y_1)] \mathbf{e}_x \right. \\ &\quad + [x_1(z_4 - z_3) + x_3(z_1 - z_4) + x_4(z_3 - z_1)] \mathbf{e}_y \\ &\quad \left. + [y_1(x_4 - x_3) + y_3(x_1 - x_4) + y_4(x_3 - x_1)] \mathbf{e}_z \right\} / 6V, \\ \nabla N_3 &= \left\{ [z_1(y_2 - y_4) + z_2(y_4 - y_1) + z_4(y_1 - y_2)] \mathbf{e}_x \right. \\ &\quad + [x_1(z_2 - z_4) + x_2(z_4 - z_1) + x_4(z_1 - z_2)] \mathbf{e}_y \\ &\quad \left. + [y_1(x_2 - x_4) + y_2(x_4 - x_1) + y_4(x_1 - x_2)] \mathbf{e}_z \right\} / 6V, \\ \nabla N_4 &= \left\{ [z_1(y_3 - y_2) + z_2(y_1 - y_3) + z_3(y_2 - y_1)] \mathbf{e}_x \right. \\ &\quad + [x_1(z_3 - z_2) + x_2(z_1 - z_3) + x_3(z_2 - z_1)] \mathbf{e}_y \\ &\quad \left. + [y_1(x_3 - x_2) + y_2(x_1 - x_3) + y_3(x_2 - x_1)] \mathbf{e}_z \right\} / 6V. \end{aligned} \quad (2.40)$$

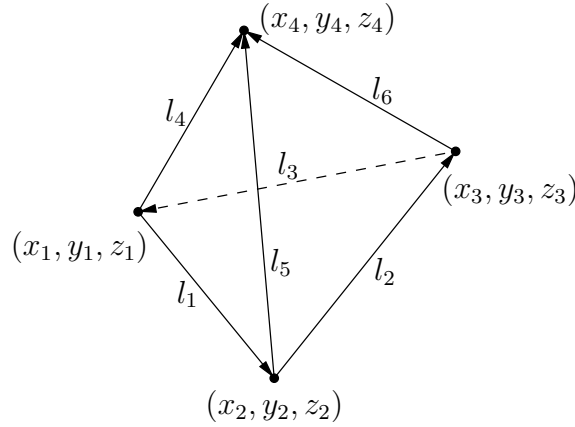


Fig. 2.12. The definition of edges with local directions of the tetrahedral finite element

Corresponding to the edge shape function defined in 2D, the 3D vector basis functions \mathbf{W}_i can also be generated by the Whitney form, and can be calculated by using the nodal shape functions, i.e.

$$\begin{aligned}
 \mathbf{W}_1 &= (N_1 \nabla N_2 - N_2 \nabla N_1) \delta_1 = W_{1,x} \mathbf{e}_x + W_{1,y} \mathbf{e}_y + W_{1,z} \mathbf{e}_z, \\
 \mathbf{W}_2 &= (N_2 \nabla N_3 - N_3 \nabla N_2) \delta_2 = W_{2,x} \mathbf{e}_x + W_{2,y} \mathbf{e}_y + W_{2,z} \mathbf{e}_z, \\
 \mathbf{W}_3 &= (N_3 \nabla N_1 - N_1 \nabla N_3) \delta_3 = W_{3,x} \mathbf{e}_x + W_{3,y} \mathbf{e}_y + W_{3,z} \mathbf{e}_z, \\
 \mathbf{W}_4 &= (N_1 \nabla N_4 - N_4 \nabla N_1) \delta_4 = W_{4,x} \mathbf{e}_x + W_{4,y} \mathbf{e}_y + W_{4,z} \mathbf{e}_z, \\
 \mathbf{W}_5 &= (N_2 \nabla N_4 - N_4 \nabla N_2) \delta_5 = W_{5,x} \mathbf{e}_x + W_{5,y} \mathbf{e}_y + W_{5,z} \mathbf{e}_z, \\
 \mathbf{W}_6 &= (N_3 \nabla N_4 - N_4 \nabla N_3) \delta_6 = W_{6,x} \mathbf{e}_x + W_{6,y} \mathbf{e}_y + W_{6,z} \mathbf{e}_z.
 \end{aligned} \tag{2.41}$$

The value of δ_i is also equal to ± 1 depending on whether the local direction of the edge is the same as the global direction or opposite. The edge definition employed in my analysis can be seen in Fig. 2.12. For example, the edge basis function \mathbf{W}_1 has tangential component only along the 1st edge and the facets $\{1-2-4\}$ and $\{1-2-3\}$, and perpendicular to the other five edges and the facets $\{1-3-4\}$ and $\{2-3-4\}$, where the numbers denote the nodes of the tetrahedron.

In eddy current field problems, equations contain the curl vector of the edge basis functions:

$$\nabla \times \mathbf{W}_i = \begin{vmatrix} \mathbf{e}_x & \mathbf{e}_y & \mathbf{e}_z \\ \partial/\partial x & \partial/\partial y & \partial/\partial z \\ W_{i,x} & W_{i,y} & W_{i,z} \end{vmatrix}, \tag{2.42}$$

or

$$\nabla \times \mathbf{W}_i = 2(\nabla N_j \times \nabla N_k), \tag{2.43}$$

where the edge i is pointing from the j^{th} node to the k^{th} node. Using linear shape functions, the curl vector has also constant value in a tetrahedron.

Chapter 3

Neural network based hysteresis operator

Hysteresis characteristics are nonlinear and multivalued relationships between the magnetic field intensity vector \mathbf{H} and the magnetization vector \mathbf{M} or the induction vector \mathbf{B} .

In this chapter, I present the NN based scalar [50, 53, 54, 60, 63] and the vector hysteresis operators [51, 56, 57, 62] developed by me with the necessary measurement data, the proposed identification technique and comparisons between measurements and simulations to show the applicability of the model. Finally, some properties of the model are presented.

3.1 The scalar hysteresis operator

In the scalar case (e.g. approximately inside a toroidal shape core), the hysteretic relationship can be represented by the scalar hysteresis operator, $M(t) = \mathcal{H}_M\{H(t)\}$ or $B(t) = \mathcal{H}_B\{H(t)\}$ [39].

3.1.1 Training sequence and preprocessing of measured data

When using NNs for function approximation, it is difficult to take into account the multivalued property of the hysteresis characteristics. To overcome this problem, I have introduced a new variable ξ associated with the measured first order reversal curves.

The first magnetization curve and a set of the first order reversal curves must be measured to build the model. Systematically generated ascending or descending external magnetic fields must be applied to measure the first order reversal curves applying the relation

$$H(t) = H_s \left[\frac{\alpha - 1}{2} + \frac{\alpha + 1}{2} \sin(2\pi ft + \pi/2) \right], \quad (3.1)$$

where H_s is the magnetic field intensity in the saturation state, f is the frequency of the excitation, $\alpha = \frac{k}{n}$ and $k \in [-n, n]$ is an integer, and $2n + 1$ is the number of generated reversal curves. These measurements must be performed at very low frequency ($f < 1$ Hz) to decrease the effect of eddy currents and other dynamic properties. Similar results can be obtained, when a triangular waveform is applied. Before measuring a

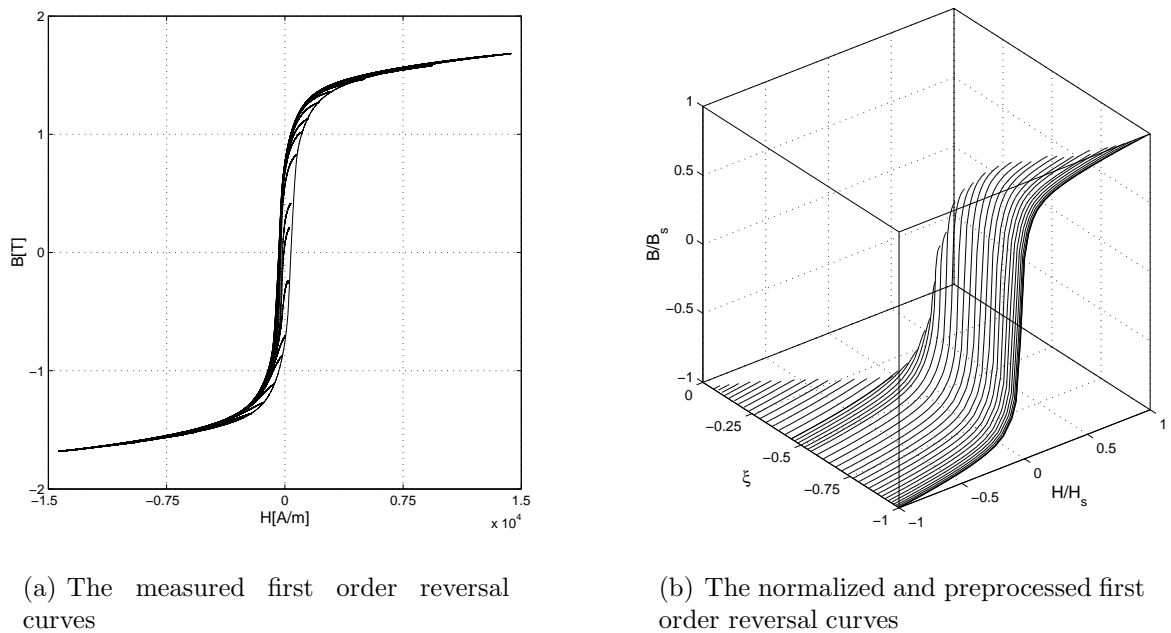


Fig. 3.1. The measured and the preprocessed training sequence

reversal curve, it is advisable to generate some major loops to make a loop stable after accommodation.

After measurements, it is useful to work with relative quantities, H/H_s and M/M_s or B/B_s , so that the input and the output of the model can run in the interval $[-1, 1]$ and the subscript s denotes the saturation state.

If a new variable ξ is added to the measured and normalized first order reversal curves, the multivalued characteristic can be represented by a single valued 2D surface with two independent variables H and ξ . It is enough to measure either the ascending or the descending branches because of the symmetry of the magnetic hysteresis characteristics. The upgrade part of the hysteresis characteristics can be described by a positive real parameter $\xi^{(asc)} = 1 - (1 + H_{tp}^{(asc)})/2$, and the downgrade part can be approximated by a negative real parameter $\xi^{(desc)} = -(1 + H_{tp}^{(desc)})/2$. These parameters can be calculated for a given transition curve starting from a turning point H_{tp} , and $\xi^{(asc)} \in [0, 1]$, $\xi^{(desc)} \in [-1, 0]$. The values ± 1 represent the major curve, e.g. -1 denotes the descending curve of the measured major loop.

After preprocessing, the aim is to find the approximating nonlinear functions which can be realized by feedforward type NNs trained by the Levenberg-Marquardt BP method [19,25,27]. Two NNs must be used, one to approximate the first magnetization curve and another one for the preprocessed first order reversal branches. The first magnetization curve (about 40 data pairs) can be approximated by a NN with 8 neurons in 1 hidden layer (1 input, H and 1 output, M or B), and the preprocessed first order transition curves (about 500-800 data pairs give accurate result depending on the shape of the characteristic) can be approached by a NN with 2 inputs (H and ξ) and 1 output (M or B) built by 7, 11 and 6 PEs in three hidden layers. The structure of the NN and the number of hidden layers and neurons have been set after some trials. The transfer function of the neurons is selected to be a bipolar sigmoid function.

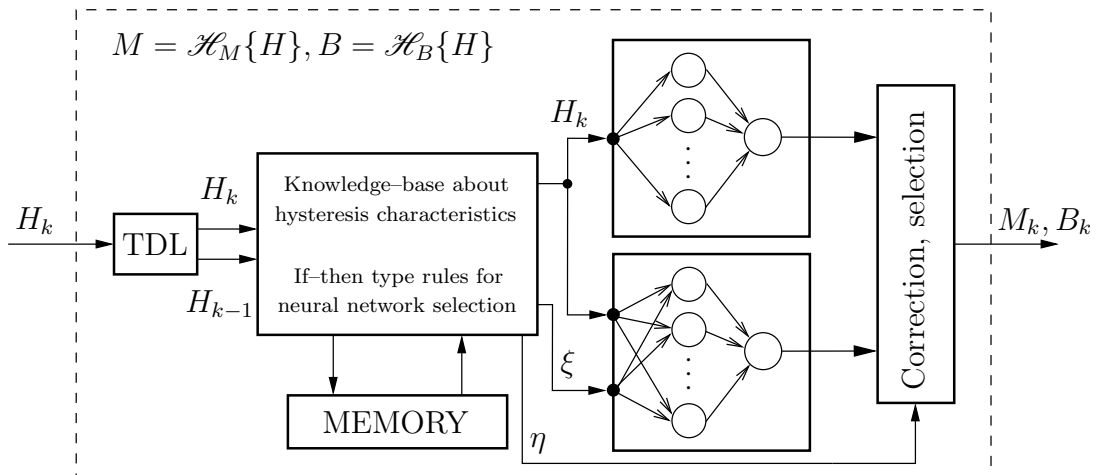


Fig. 3.2. The block representation of the scalar model

The training of the two NNs took about 20 minutes on a Celeron 566 MHz computer (192 Mbyte RAM) using the Neural Network Toolbox of MATLAB [99]. When applying a training sequence described above to identify the first magnetization curve and the preprocessed first order reversal curves, the stopping criterion $MSE = 10^{-6}$ can be reached by not more than 500 and 1200 training epochs in the two NNs. The measured first order descending curves (containing 46 branches) generated by the excitation waveform (3.1) are plotted in Fig. 3.1(a). In this case $n = 20$, but there are some measured curves near the coercive field where the characteristic is very steep and there is no information enough about the variation of the curves in this area. After applying the proposed preprocessing technique, a 2D surface can be obtained as shown in Fig. 3.1(b). The training sequence contained 1296 measured points. The measurement was performed at $f = 0.2$ Hz frequency on a toroidal shape C19 structural steel [52]. In this case, only technical saturation can be described by the values $H_s = 1.433 \cdot 10^4$ A/m and $B_s = 1.688$ T. Higher magnetic field intensity could not be generated by the applied power supply. The particular presentation of the measurement setup and scalar hysteresis measurements can be found in the section 3.1.4.

3.1.2 Operation of the model

As I stated in the last section, the developed hysteresis model consists of two trained NNs. The first magnetization curve and the first order reversal branches are stored in NNs, but a memory mechanism must be realized by an additional algorithm based on heuristics. The block representation of the NN based scalar hysteresis model can be seen in Fig. 3.2 and described below.

In general, the actual value of the magnetization (or the magnetic induction) is dependent on the actual value of the magnetic field intensity and the prehistory of the magnetic material. The normalized magnetization M_k or magnetic induction B_k at the simulation step k yielded by the NN based model is constructed on the actual value of the normalized magnetic field intensity H_k , the appropriate value of the parameter ξ and a set of turning points stored in the memory of the model.

The knowledge-base is the main part of the implemented NN model. It contains if-then type rules about the hysteresis phenomena and about the properties of the hysteresis

characteristics, and controls the other blocks of the model. The operation of this model is based on a set of turning points in the ascending and in the descending branches denoted by $H_{tp}^{(asc)}$ and $H_{tp}^{(desc)}$, respectively. Turning points are stored in the memory, that is an array with the elements $[H_{tp}, M_{tp}, \xi]^T$ or $[H_{tp}, B_{tp}, \xi]^T$, denoted by **MATRIX**^(asc) and **MATRIX**^(desc) for ascending and descending curves. Turning points can be detected by the evaluation of a sequence of $\{H_{k-1}, H_k\}$ generated by a tapped delay line (TDL). After detecting a turning point $H_{tp} = H_{START} = H_{k-1}$ and storing it in the memory, the aim is to select an appropriate transition curve with the right value ξ for the detected turning point (H_{tp}, M_{tp}) or (H_{tp}, B_{tp}) , where $M_{tp} = M_{START} = M_{k-1}$ or $B_{tp} = B_{START} = B_{k-1}$. This task has been solved by the regula-falsi method.

There are some basic rules I have implemented in the knowledge-base as if-then type rules. First, a simple lemma about the behavior of the minor loops has been determined: they must be closed as illustrated in Fig. 3.3(a). Therefore the accommodation phenomena cannot be simulated yet. After detecting a turning point, the algorithm for a general minor loop can be summarized as follows. If **MATRIX**^(desc) (**MATRIX**^(asc)) has more than one column and the normalized magnetic field intensity H_k is increasing (decreasing) at the k^{th} simulation step, i.e. $H_k > H_{k-1}$ ($H_k < H_{k-1}$), then the actual minor loop must be closed at the last stored value of $H_{GOAL} = H_{tp}^{(desc)}$ ($H_{GOAL} = H_{tp}^{(asc)}$) which can be found in the last column of **MATRIX**^(desc) (**MATRIX**^(asc)). The value of the normalized magnetization M_k yielded by the NN model at H_{GOAL} must be equal to $M_{GOAL} = M_{tp}^{(desc)}$ ($M_{GOAL} = M_{tp}^{(asc)}$) stored in the last column of the appropriate **MATRIX** (it is also true for magnetic induction). This is the condition for closing a minor loop. The data sets of reached turning points where the actual minor loop is closing must be cleared from the memory by deleting the appropriate column of the arrays according to the closing minor loop. These are always stored in the last column of the memory. The first column of the arrays in the memory containing the parameters of the normalized major loop ($[+1, +1, -1]^T$ and $[-1, -1, +1]^T$) cannot be cleared. The memory mechanism is very similar to the staircase line of the classical Preisach model, but the memory as well as the output of the NN model is continuous in nature and not discrete.

The results of simulation have highlighted that, the value of the normalized magnetization (induction) yielded by the relevant NN and the adequate value of the normalized magnetization (induction) chosen from the appropriate column of the memory at the value H_{GOAL} are not equal. Therefore a correction $\eta = \eta(H, M)$ ($\eta = \eta(H, B)$) must be used to eliminate this deviation while closing a minor loop. The value of the parameter η can be calculated as the difference between the required value of magnetization (induction) and the response of the actual NN at the value of the magnetic field intensity H_{GOAL} when an actual minor loop is closed:

$$\eta = M_{GOAL} - M^{(NN)}(H_{GOAL}, \xi_{START}), \quad (3.2)$$

where ξ_{START} is the value of the parameter ξ at the actual value of H_{START} . The parameter η must be calculated beforehand when opening a minor loop and must be applied increasing linearly during the magnetization process from zero (when the minor loop is opening) to the given value η (when the minor loop is closing).

An additional precept must be used as formulated in the following rule: symmetric hysteresis loops are assumed (see Fig. 3.3(b)). After the detection of a turning

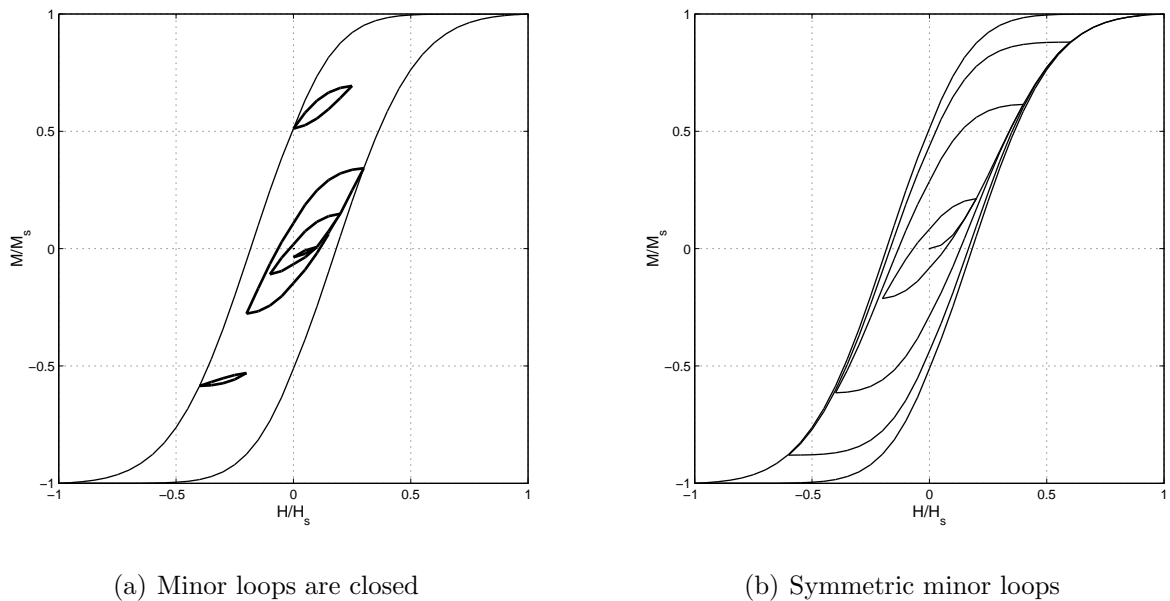


Fig. 3.3. Rules of minor loops in the knowledge-base of the model

point and an ascending (descending) curve has been chosen, furthermore $\mathbf{MATRIX}^{(desc)}$ ($\mathbf{MATRIX}^{(asc)}$) has only one column, then $H_{GOAL} = -H_{START}$ and $M_{GOAL} = -M_{START}$.

If $\mathbf{MATRIX}^{(desc)}$ or $\mathbf{MATRIX}^{(asc)}$ has been reduced to a single column array after the wiping out process, then saturation is assumed: $H_{GOAL} = 1$, $M_{GOAL} = 1$ or $H_{GOAL} = -1$, $M_{GOAL} = -1$, depending on the direction of the magnetic field intensity.

Accommodation property can also be simulated when $H_k = H_k + \alpha M_{k-1}$ is applied as input of the model, where α is the so called moving parameter.

The above two rules are also valid if the output of the model is the magnetic flux density.

3.1.3 Properties of the scalar model

The presented NN based hysteresis model is a mathematical model without physical meaning, because a NN is a black box model, and there is no connection between the object to be simulated and the weight coefficients of the NN model. However, the well known Preisach, the Jiles–Atherton and the Stoner–Wohlfarth models are based on physical background. These simulation techniques can also be used in Computer Aided Design (CAD) software and, in addition, they can explain physical phenomena. Sometimes it is difficult to identify these models from noisy measurements. From engineering point of view, it is very useful to apply a mathematical model with simple identification process.

There are some important advantages of the developed NN based scalar model, such as

- (a) the proposed preprocessing task can be applied on any kind of hysteresis characteristics, i.e. hysteresis curves with different shapes can be simulated without modifications of the model,

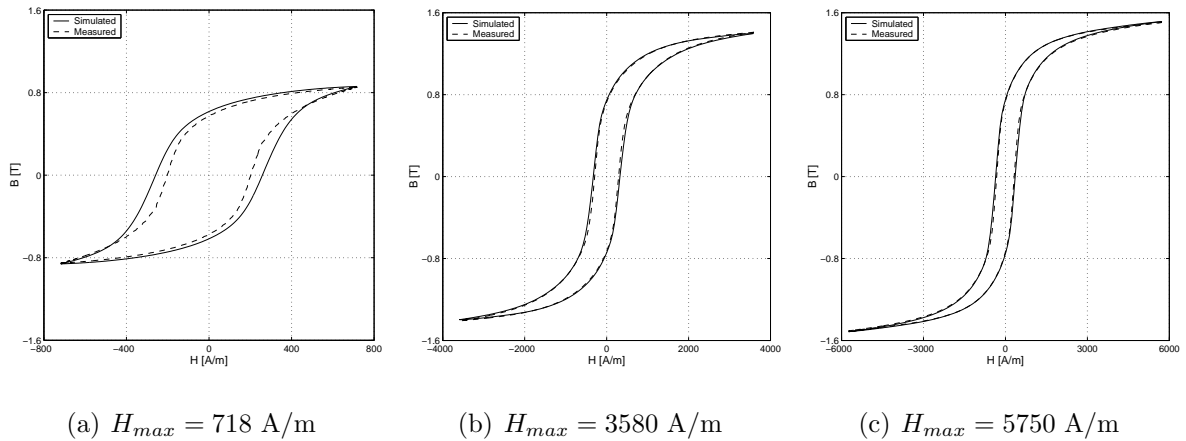


Fig. 3.4. Comparisons between the simulated and the measured symmetric minor loops

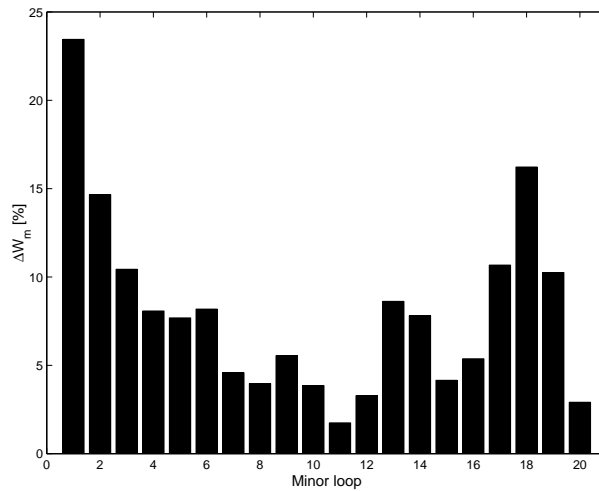


Fig. 3.5. The error in the hysteresis area between the measured and the simulated characteristics

- (b) the identification of the scalar model is an easy task, once the measured first magnetization curve and the first order reversal branches are known,
- (c) the output of the model, i.e. the normalized magnetization or the normalized induction is a continuous function of the magnetic field intensity, because NNs can interpolate between trained data according to the generalization property of the NNs,
- (d) if necessary, the differential susceptibility χ_{diff} as well as the integral of the output of the model (e.g. to calculate hysteresis losses) can be expressed in analytical form.

It is very important to verify a NN based model by comparing the simulated and the measured data which were not contained in the training sequence. I have measured symmetric minor loops, and the comparison between measurements and simulations can be seen in Fig. 3.4(a), Fig. 3.4(b) and Fig. 3.4(c). The maximum value of the calculated error $\Delta B = 100|(B_m - B_s)/B_{m,s}|$ is 35%, 10% and 8% respectively, where B_m and B_s

are the measured and the simulated induction, respectively, and $B_{m,s} = 1.688$ T is the measured induction in the saturation state. The maximum difference can be located near the coercive field as highlighted in the figures. The measured major loop and the measured first order reversal curves (i.e. the training sequence) can be approximated with an error value less than maximum 4 – 5%.

To compare the measured and the simulated characteristics, the hysteresis losses from the enclosed area of the hysteresis loops are determined for 20 measured and simulated symmetric minor loops. The calculated relative error in the losses with respect to the measured curves is plotted in Fig. 3.5.

3.1.4 Scalar magnetic hysteresis measurement using LabVIEW

Ferromagnetic hysteresis measurement has been performed in our Magnetic Laboratory by a computer controlled automated measuring system [47, 48, 52]. Generation of excitation and measurements are carried out by applying the user-friendly environment of LabVIEW. The graphical user interface of the developed software is illustrated in Fig. 3.6, data and graphs in the window are presented briefly below.

LabVIEW is an application software to perform sophisticated display and analysis capabilities required for virtual instrumentation. This can be used to create test measurement systems by combining different hardware and software components. Data acquisition and waveform generation can be carried out by virtual software instruments and tools, and the measurement can be realized by plug-in hardware connected to the computer via special National Instruments driver software [38].

Schematic view of the measurement set-up can be seen in Fig. 3.7. The investigated ferromagnetic sample has toroidal shape. It is supposed that, both the magnetic field intensity with its scalar value H and the magnetic induction B are uniform inside the material and directed along the axis of the toroidal core. This results in a scalar hysteresis characteristic. The excitation coil is excited by the current $i(t)$ supplied by the power generator KIKUSUI [22] and the current waveform is measured by the voltage of the temperature and voltage independent resistor of $R = 0.01 \Omega$ ($i(t) = u_P(t)/R$). The measured magnetic field intensity is proportional to the exciting current and can be calculated as

$$H(t) = \frac{N_p i(t)}{l}, \quad (3.3)$$

where $N_p = 170$ is the number of turns of the excitation (primary) coil, $i(t)$ is the excitation current and $l = 176$ mm is the equivalent magnetic length of the toroidal core. The magnetic flux density B can be calculated from the measured induced voltage of the measuring (secondary) coil $u_s(t)$ as

$$B(t) = B_0 + \frac{1}{S N_s} \int_0^t u_s(\tau) d\tau, \quad (3.4)$$

where B_0 is an integration constant, $S = 20 \text{ mm}^2$ is the cross-section of the core and $N_s = 182$ is the number of turns of the measuring coil. The measured signals, the calculated waveform of the magnetic field intensity and of the magnetic flux density and the resulted hysteresis characteristic are visualized in the user interface (see Fig. 3.6).

Measurements are performed by using the LabVIEW environment. The computer communicates with the measuring instruments through an NI-DAQ (National Instruments, Data Acquisition Device) BNC-2090 panel which is connected to the DAQ

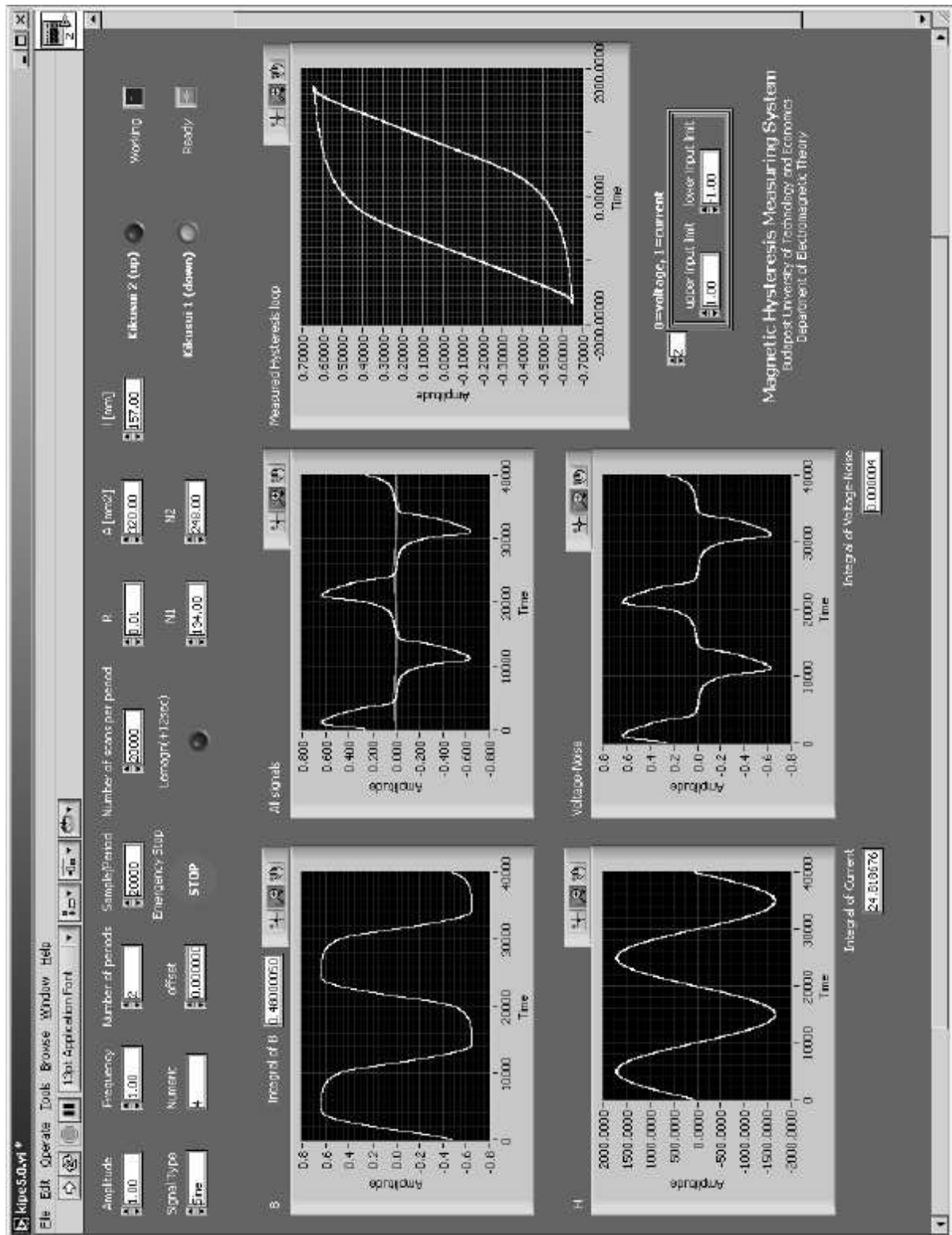


Fig. 3.6. LabVIEW GUI example

card. The bipolar power supply KIKUSUI PBX 20–20 (power limit is approximately 100W [22]) is applied to generate the excitation of the primary coil. KIKUSUI is controlled by the constant-current mode (CC mode) [22], since current is proportional to the magnetic field intensity. The excitation signal is derived by LabVIEW functions and

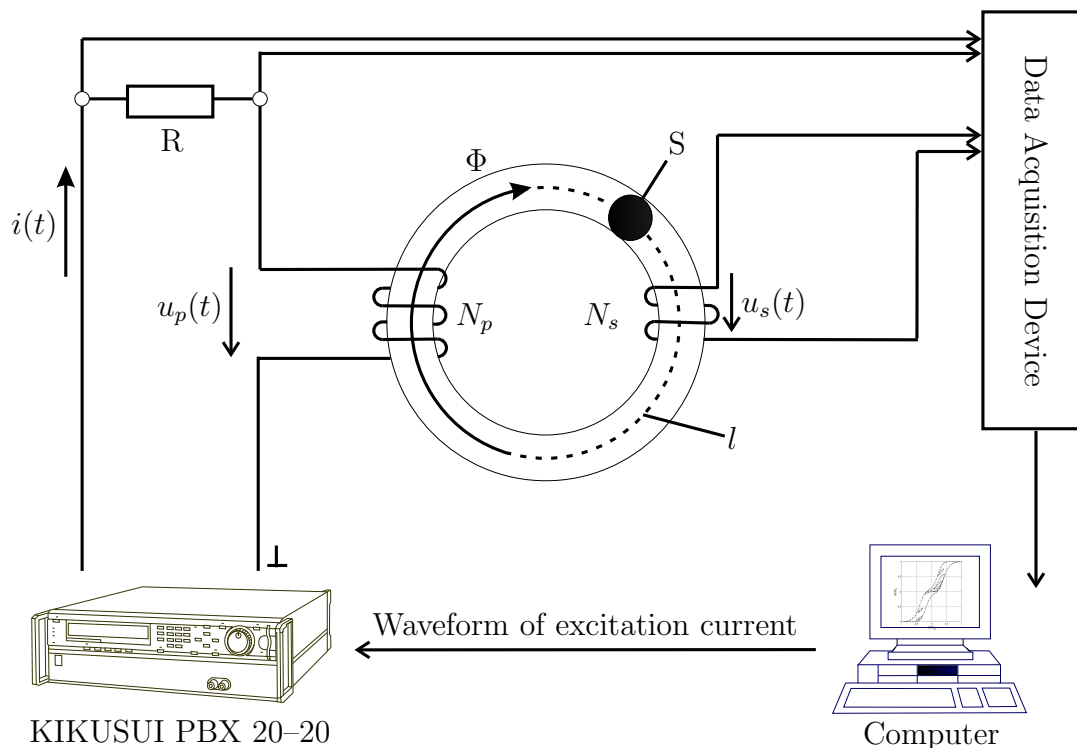


Fig. 3.7. Schematic view of the scalar hysteresis measurement set-up

the power supply can follow this signal by the analog output of the BNC panel. The induced voltage is measured by using the same DAQ card. Data acquisition and generation of the excitation current can be performed simultaneously by using the intermediate virtual instruments (circular buffered waveform generation and measurement) [38].

Measured curves are saved to a file, for further use of the measured data using other software or for a report. The waveform, the amplitude and the frequency of the excitation current, the number of measured periods and of measured samples in one period, and other parameters (N_p , N_s , S , l , R) can be set through the graphical user interface.

Computer-aided measurements can only be performed by sampling using A/D and D/A converters (acquisition) [38]. This can be carried out through general DAQ devices, GPIB interfaces, RS-232 instruments and so on. This may be a weak point of the measurement process if very steep signals must be measured (e.g. induced voltage in the secondary coil), but it can be eliminated by the appropriate choice of the sampling rate. The main advantage of applying computer controlled measurement is the data analysis, such as curve fitting, frequency response, filtering, Fourier analysis and many other numerical operations realized by a software.

3.2 The isotropic vector hysteresis operator

3.2.1 Description of the model

The vector NN based model of the magnetic hysteresis is constructed as a superposition of scalar NN based models. The magnetization vector \mathbf{M} can be expressed in two dimensions as

$$\mathbf{M} = \int_{-\pi/2}^{\pi/2} \mathbf{e}_\varphi \mathcal{H}\{H_\varphi\} d\varphi, \quad (3.5)$$

where $M_\varphi = \mathcal{H}\{H_\varphi\}$ is the scalar magnetization in the direction \mathbf{e}_φ , and the projected magnetic field intensity is $H_\varphi = |\mathbf{H}| \cos(\vartheta_H - \varphi)$ with the direction of the magnetic field intensity vector \mathbf{H} , denoted by ϑ_H . First, I have analyzed the isotropic vector hysteresis characteristic, when the same NN based scalar hysteresis operator $\mathcal{H}\{\cdot\}$ has been used in all directions.

In computer realization, it is useful to discretize the interval $\varphi \in [-\pi/2, \pi/2]$ as $\varphi_i = -\pi/2 + (i-1)\pi/n'$, where $i = 1, \dots, n'$, and n' is the number of directions. The magnetization vector is the vectorial sum of the scalar magnetization yielded by the individual scalar hysteresis models, i.e. (see Fig. 3.8)

$$\mathbf{M} \cong \sum_{i=1}^{n'} \mathbf{e}_{\varphi_i} M_{\varphi_i} = \sum_{i=1}^{n'} \mathbf{e}_{\varphi_i} \mathcal{H}\{H_{\varphi_i}\}. \quad (3.6)$$

In three dimensions, the following expression can be obtained,

$$\mathbf{M} = \int_{-\pi/2}^{\pi/2} \int_{-\pi/2}^{\pi/2} \mathbf{e}_{\varphi, \vartheta} \mathcal{H}\{H_{\varphi, \vartheta}\} d\varphi d\vartheta, \quad (3.7)$$

where the projected magnetic field intensity is $H_{\varphi, \vartheta} = [a_1 \ a_2 \ a_3]_{\varphi, \vartheta} [H_x \ H_y \ H_z]^T$, and the directions are given as $\mathbf{a} = a_1 \mathbf{e}_x + a_2 \mathbf{e}_y + a_3 \mathbf{e}_z$, $|\mathbf{a}| = 1$ corresponding to the given directions allocated by the angles φ and ϑ as shown in Fig. 3.9(a) and generated by an icosahedron (see Fig. 3.9(b)). The angles φ and ϑ are measured from the x -axis and from the $x-y$ plane, respectively. Any kind of regular 3D formation can be used (like polyhedrons, e.g. cube, octahedron, dodecahedron and so on), but I have found that, the icosahedron gives the best results. The applied scalar hysteresis operator is also unique for all directions. The integral formula (3.7) can be realized by a numerical sum in the discrete form

$$\mathbf{M} \cong \sum_{i=1}^{n'} \mathbf{e}_{\varphi_i, \vartheta_i} M_{\varphi_i, \vartheta_i} = \sum_{i=1}^{n'} \mathbf{e}_{\varphi_i, \vartheta_i} \mathcal{H}\{H_{\varphi_i, \vartheta_i}\}, \quad (3.8)$$

where n' is the number of directions in the 3D space.

3.2.2 The identification process

I have measured the Everett function in the x direction, then the following well known trivial condition can be obtained between the measured scalar Everett function $F(\alpha, \beta)$ and the unknown 2D vector Everett function $E(\alpha, \beta)$ [67]:

$$F(\alpha, \beta) = \int_{-\pi/2}^{\pi/2} \cos \varphi E(\alpha \cos \varphi, \beta \cos \varphi) d\varphi. \quad (3.9)$$

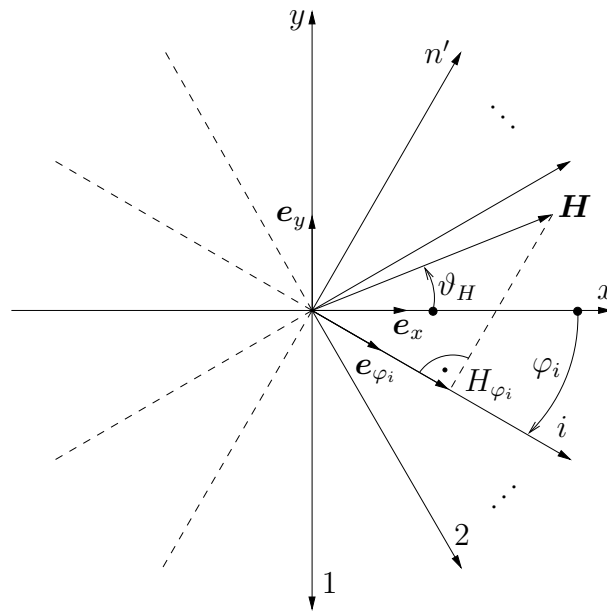
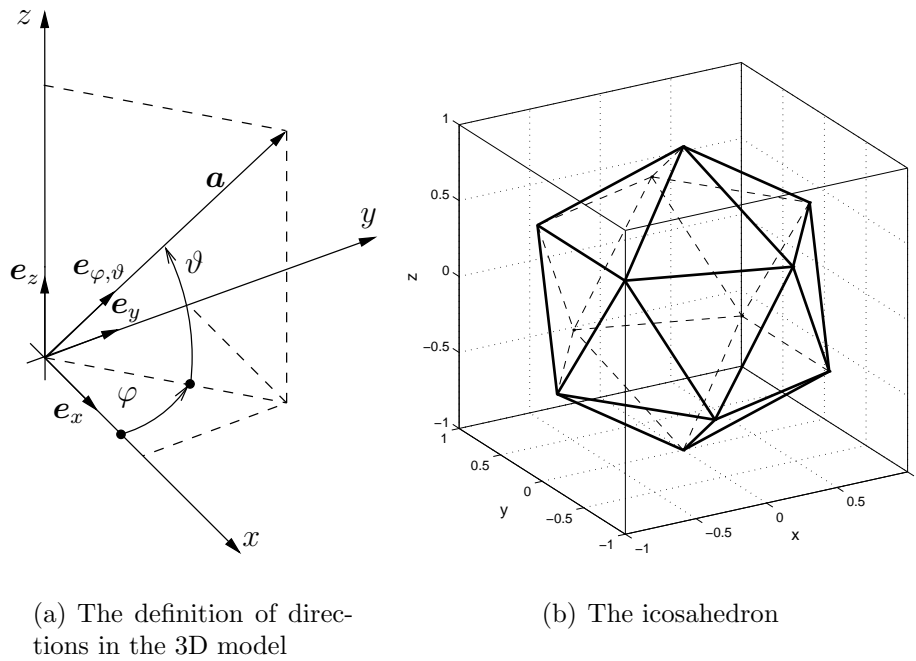


Fig. 3.8. The definition of directions in the 2D model



(a) The definition of directions in the 3D model

(b) The icosahedron

Fig. 3.9. Directions of the 3D model are generated by the icosahedron

This expression can be written by skipping the constant $\Delta\varphi = \pi/n'$ in a discretized form as

$$F(\alpha_k, \beta_l) \cong \sum_{i=1}^{n'} \cos \varphi_i E(\alpha_k \cos \varphi_i, \beta_l \cos \varphi_i). \quad (3.10)$$

If assuming isotropic magnetic material, then the measured Everett function $F(\alpha, \beta)$ is unique for every direction [67]. Expression (3.10) can only be solved numerically during the optimization process. The Everett tables $F(\alpha_k, \beta_l)$ and $E(\alpha_k, \beta_l)$ have been

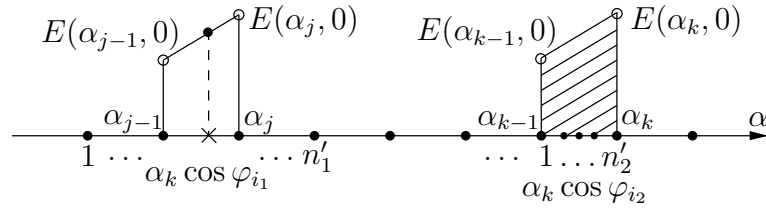


Fig. 3.10. Illustration for the first step of the identification, when $\alpha \geq 0$ and $\beta = 0$

divided into $(N + 1) \times (N + 1)$ parts, with $k, l = 1, \dots, N + 1$, $\alpha_k = \frac{2}{N} \left(k - \frac{N+1}{2}\right) - \frac{1}{N}$, $\beta_l = \frac{2}{N} \left(\frac{N+1}{2} - l\right) + \frac{1}{N}$. In this case $\alpha \in [-1, \dots, +1]$, $\beta \in [+1, \dots, -1]$ and N must be an even number.

In the 3D case, the expression (3.10) can also be applied, but φ_i is then the spatial angle between the directions generated by the icosahedron and the x -axis.

The identification process is divided into two main parts. In the first step, the part of the Everett function can be identified where $\beta = 0$ and $\alpha = -\beta$. In the second step, the other parts can be calculated step by step by using values from the first step and some points from the second step.

The first step: starting the identification process

I have developed the identification technique on the basis of the above process as described in the following.

A part of the Everett function is independent of one of the two variables α and β along the line $\alpha \geq 0$ and $\beta = 0$, i.e. $k = \frac{N}{2} + 1, \dots, N + 1$ and $l = \frac{N}{2} + 1$,

$$F(\alpha_k, 0) \cong \sum_{i=1}^{n'} \cos \varphi_i E(\alpha_k \cos \varphi_i, 0). \tag{3.11}$$

In this case, the Everett function can be divided into two parts. The first n'_1 points are known, but the other n'_2 points contain the unknown part of the vector Everett function $E(\alpha_k, 0)$,

$$F(\alpha_k, 0) \cong \sum_{i_1=1}^{n'_1} \cos \varphi_{i_1} E(\alpha_k \cos \varphi_{i_1}, 0) + \sum_{i_2=1}^{n'_2} \cos \varphi_{i_2} E(\alpha_k \cos \varphi_{i_2}, 0). \tag{3.12}$$

When $\alpha_{j-1} < \alpha_k \cos \varphi_{i_1} \leq \alpha_j$ and $\alpha_{j-1} < \alpha_j \leq \alpha_{k-1}$ and assuming linear interpolation between known points of the vector Everett function $(\alpha_{j-1}, E(\alpha_{j-1}, 0))$ and $(\alpha_j, E(\alpha_j, 0))$, the following formula –illustrated in Fig. 3.10– can be applied to interpolate a given value,

$$\frac{E(\alpha_j, 0) - E(\alpha_{j-1}, 0)}{\alpha_j - \alpha_{j-1}} = \frac{E(\alpha_k \cos \varphi_{i_1}, 0) - E(\alpha_{j-1}, 0)}{\alpha_k \cos \varphi_{i_1} - \alpha_{j-1}}, \tag{3.13}$$

from which

$$E(\alpha_k \cos \varphi_{i_1}, 0) = E(\alpha_{j-1}, 0) + \frac{\alpha_k \cos \varphi_{i_1} - \alpha_{j-1}}{\alpha_j - \alpha_{j-1}} \times (E(\alpha_j, 0) - E(\alpha_{j-1}, 0)). \tag{3.14}$$

This expression contains known values of the vector Everett function calculated in the previous steps. The number of known points increases with the index k . When $\alpha_{k-1} < \alpha_k \cos \varphi_{i_2} \leq \alpha_k$, then a similar expression can be used:

$$\frac{E(\alpha_k, 0) - E(\alpha_{k-1}, 0)}{\alpha_k - \alpha_{k-1}} = \frac{E(\alpha_k \cos \varphi_{i_2}, 0) - E(\alpha_{k-1}, 0)}{\alpha_k \cos \varphi_{i_2} - \alpha_{k-1}}, \quad (3.15)$$

from which

$$E(\alpha_k \cos \varphi_{i_2}, 0) = E(\alpha_{k-1}, 0) + \frac{\alpha_k \cos \varphi_{i_2} - \alpha_{k-1}}{\alpha_k - \alpha_{k-1}} \times (E(\alpha_k, 0) - E(\alpha_{k-1}, 0)). \quad (3.16)$$

This contains the only one unknown point of the vector Everett function $E(\alpha_k, 0)$. The following expression can be obtained by substituting the relations (3.14) and (3.16) into the equation (3.12):

$$\begin{aligned} F(\alpha_k, 0) = & \sum_{i_1=1}^{n'_1} \cos \varphi_{i_1} \left\{ E(\alpha_{j-1}, 0) \right. \\ & \left. + \frac{\alpha_k \cos \varphi_{i_1} - \alpha_{j-1}}{\alpha_j - \alpha_{j-1}} (E(\alpha_j, 0) - E(\alpha_{j-1}, 0)) \right\} \\ & + E(\alpha_{k-1}, 0) ((1 + b_k)c_1 - a_k c_2) \\ & + E(\alpha_k, 0) (a_k c_2 - b_k c_1), \end{aligned} \quad (3.17)$$

where $a_k = \frac{\alpha_k}{\alpha_k - \alpha_{k-1}}$, $b_k = \frac{\alpha_{k-1}}{\alpha_k - \alpha_{k-1}}$, $c_1 = \sum_{i_2=1}^{n'_2} \cos \varphi_{i_2}$, and $c_2 = \sum_{i_2=1}^{n'_2} \cos^2 \varphi_{i_2}$ and $E(\alpha_k, 0)$ can be expressed.

A similar mathematical formulation can be obtained along the line $\alpha = -\beta$. In this case, the indices k and l are in the interval $[\frac{N}{2} + 1, \dots, N + 1]$. According to the linear interpolation between two points, the following expressions can be obtained after some mathematical manipulations. If $\alpha_{j-1} = \beta_{j-1} < \alpha_k \cos \varphi_{i_1} = \beta_l \cos \varphi_{i_1} \leq \alpha_j = \beta_j$ and $\alpha_{j-1} = \beta_{j-1} < \alpha_j = \beta_j \leq \alpha_{k-1} = \beta_{k-1}$, then the known point in the Everett function can be expressed as

$$\begin{aligned} E(\alpha_k \cos \varphi_{i_1}, \beta_l \cos \varphi_{i_1}) = & E(\alpha_{j-1}, \beta_{j-1}) \\ & + \frac{\sqrt{\alpha_k^2 \cos^2 \varphi_{i_1} + \beta_l^2 \cos^2 \varphi_{i_1}} - \sqrt{\alpha_{j-1}^2 + \beta_{j-1}^2}}{\sqrt{\alpha_j^2 + \beta_j^2} - \sqrt{\alpha_{j-1}^2 + \beta_{j-1}^2}} \\ & \times (E(\alpha_j, \beta_j) - E(\alpha_{j-1}, \beta_{j-1})). \end{aligned} \quad (3.18)$$

If $\alpha_{k-1} = \beta_{k-1} < \alpha_k \cos \varphi_{i_2} = \beta_l \cos \varphi_{i_2} \leq \alpha_k = \beta_k$, then the unknown point in the Everett function can be expressed as

$$\begin{aligned} E(\alpha_k \cos \varphi_{i_2}, \beta_l \cos \varphi_{i_2}) = & E(\alpha_{k-1}, \beta_{l-1}) \\ & + \frac{\sqrt{\alpha_k^2 \cos^2 \varphi_{i_2} + \beta_l^2 \cos^2 \varphi_{i_2}} - \sqrt{\alpha_{k-1}^2 + \beta_{l-1}^2}}{\sqrt{\alpha_k^2 + \beta_l^2} - \sqrt{\alpha_{k-1}^2 + \beta_{l-1}^2}} \\ & \times (E(\alpha_k, \beta_l) - E(\alpha_{k-1}, \beta_{l-1})). \end{aligned} \quad (3.19)$$

Here $E(\alpha_k, \beta_l)$ is the only unknown, and it can be expressed after substituting the relations (3.18) and (3.19) into (3.10). This generates some points in the vector Everett function and gives an initiative step to determine the other values.

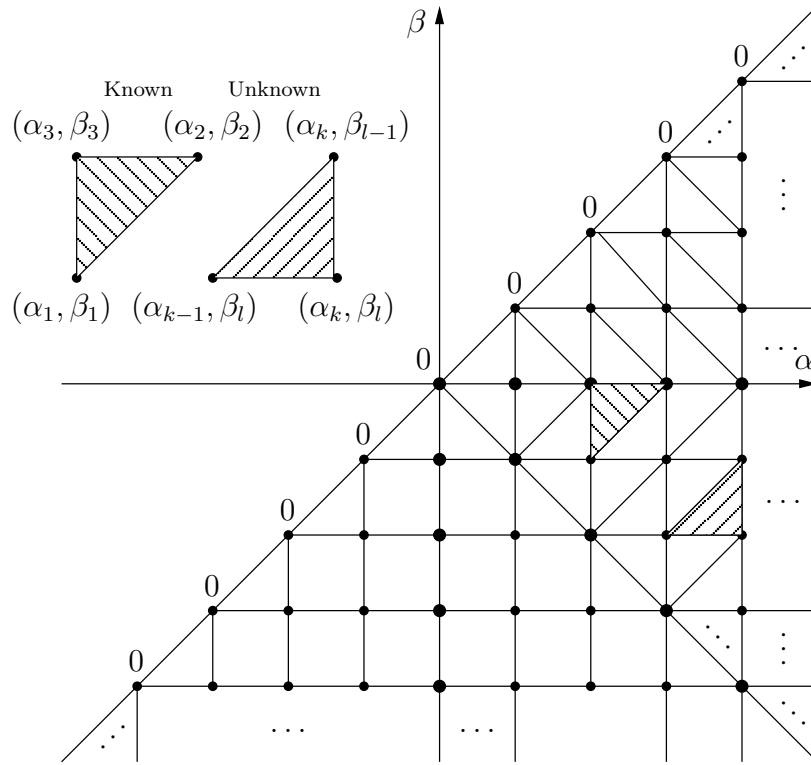


Fig. 3.11. Illustration for the second step of the identification process

The second step: the other points on the vector Everett plane

I have divided the vector Everett function into triangles and I have applied linear interpolation on these triangles to calculate the values on the Everett functions corresponding to the coordinates $(\alpha_k \cos \varphi, \beta_l \cos \varphi)$. An explanatory plot with notations can be seen in Fig. 3.11.

In this case, the Everett function can also be divided into two parts. The first n'_1 points are known, but the other n'_2 points contain the unknown part of the vector Everett function $E(\alpha_k, \beta_l)$,

$$\begin{aligned}
 F(\alpha_k, \beta_l) \cong & \sum_{i_1=1}^{n'_1} \cos \varphi_{i_1} E(\alpha_k \cos \varphi_{i_1}, \beta_l \cos \varphi_{i_1}) \\
 & + \sum_{i_2=1}^{n'_2} \cos \varphi_{i_2} E(\alpha_k \cos \varphi_{i_2}, \beta_l \cos \varphi_{i_2}).
 \end{aligned} \tag{3.20}$$

If $\alpha > 0$ and $\beta < 0$ ($k = l + 1, \dots, N + 1$, $l = \frac{N}{2} + 2, \dots, N + 1$) and the point $(\alpha_k \cos \varphi_{i_1}, \beta_l \cos \varphi_{i_1})$ is on a triangle with known node values, then the equation of a plane with three points e.g. $(\alpha_{k-1}, \beta_l, E_1)$, $(\alpha_k, \beta_{l-1}, E_2)$ and $(\alpha_{k-1}, \beta_{l-1}, E_3)$ can be applied as

$$\begin{vmatrix}
 \alpha_k \cos \varphi_{i_1} - \alpha_1 & \beta_l \cos \varphi_{i_1} - \beta_1 & E - E_1 \\
 \alpha_2 - \alpha_1 & \beta_2 - \beta_1 & E_2 - E_1 \\
 \alpha_3 - \alpha_1 & \beta_3 - \beta_1 & E_3 - E_1
 \end{vmatrix} = 0, \tag{3.21}$$

where $\alpha_1 = \alpha_{k-1}$, $\beta_1 = \beta_l$, $\alpha_2 = \alpha_k$, $\beta_2 = \beta_{l-1}$, $\alpha_3 = \alpha_{k-1}$, $\beta_3 = \beta_{l-1}$, $E_1 = E(\alpha_{k-1}, \beta_l)$, $E_2 = E(\alpha_k, \beta_{l-1})$, $E_3 = E(\alpha_{k-1}, \beta_{l-1})$ and $E = E(\alpha_k \cos \varphi_{i_1}, \beta_l \cos \varphi_{i_1})$. From this

equation

$$E(\alpha_k \cos \varphi_{i_1}, \beta_l \cos \varphi_{i_1}) = E_1 - \frac{(\alpha_k \cos \varphi_{i_1} - \alpha_1)(cf - ed)}{(ad - bc)} - \frac{(\beta_l \cos \varphi_{i_1} - \beta_1)(be - af)}{(ad - bc)}, \quad (3.22)$$

where $a = \alpha_2 - \alpha_1$, $b = \alpha_3 - \alpha_1$, $c = \beta_2 - \beta_1$, $d = \beta_3 - \beta_1$, $e = E_2 - E_1$ and $f = E_3 - E_1$. Varying these three points, the equation of any other triangles with known node values can be represented and known points can be calculated.

If point $(\alpha_k \cos \varphi_{i_2}, \beta_l \cos \varphi_{i_2})$ is on a triangle which contains the unknown value of the vector Everett function $E(\alpha_k, \beta_l)$, then the equation of a plane with the three points $(\alpha_{k-1}, \beta_l, E_1)$, (α_k, β_l, E_2) and $(\alpha_k, \beta_{l-1}, E_3)$ can be applied as

$$\begin{vmatrix} \alpha_k \cos \varphi_{i_2} - \alpha_{k-1} & \beta_l \cos \varphi_{i_2} - \beta_l & E - E_1 \\ \alpha_k - \alpha_{k-1} & \beta_l - \beta_l & E_2 - E_1 \\ \alpha_k - \alpha_{k-1} & \beta_{l-1} - \beta_l & E_3 - E_1 \end{vmatrix} = 0, \quad (3.23)$$

where $E_1 = E(\alpha_{k-1}, \beta_l)$, $E_2 = E(\alpha_k, \beta_l)$, $E_3 = E(\alpha_k, \beta_{l-1})$ and $E = E(\alpha_k \cos \varphi_{i_2}, \beta_l \cos \varphi_{i_2})$. From this equation

$$E(\alpha_k \cos \varphi_{i_2}, \beta_l \cos \varphi_{i_2}) = E_1 + \frac{(\beta_{l-1} - \beta_l)(\alpha_k \cos \varphi_{i_2} - \alpha_{k-1})(E_2 - E_1)}{(\alpha_k - \alpha_{k-1})(\beta_{l-1} - \beta_l)} - \frac{(\alpha_k - \alpha_{k-1})(\beta_l \cos \varphi_{i_2} - \beta_l)(E_2 - E_3)}{(\alpha_k - \alpha_{k-1})(\beta_{l-1} - \beta_l)} \quad (3.24)$$

can be obtained which contains the unknown value E_2 . Substituting (3.22) and (3.24) into (3.20) E_2 can be expressed for all indices k and l .

If $\alpha > 0$ and $\beta > 0$ ($k = N + 3 - l, \dots, N + 1$, $l = \frac{N}{2}, \dots, 1$), then a similar procedure can be applied, but the shape of the triangles is different.

The Everett function is symmetrical with respect to the line $\alpha = -\beta$, so it is enough to identify only the half of the vector Everett function.

3.2.3 Verification of the model

To illustrate the above process, I have assumed that, the measured Everett function is given in the x direction and it is plotted in Fig. 3.12(a). The identified 2D vector Everett function, and the identified 3D vector Everett function are shown in Fig. 3.12(b) and Fig. 3.12(c).

Identification has been performed by the method described above, 20 directions and 9 directions have been used in the 2D and in the 3D model, respectively. The measured scalar Everett surface can be approximated with a relative error below 0.3% and 0.4% by the 2D and the 3D models by substituting into the trivial condition (3.10). The resulting vector Everett functions –as highlighted in the figures– do not have the usual shape, meaning that, the first order reversal curves also do not have the usual descending shape, but they can be approximated easily by the scalar NN based hysteresis model.

First order reversal curves can be derived from the identified vector Everett function, and NNs can be trained as well as models can be built by trained NNs. A comparison

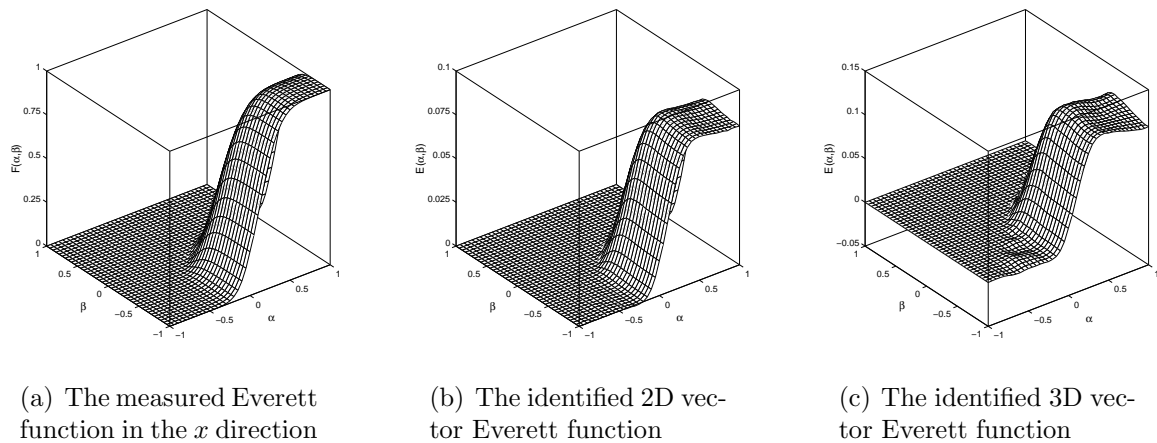


Fig. 3.12. Identification results of the isotropic vector hysteresis model

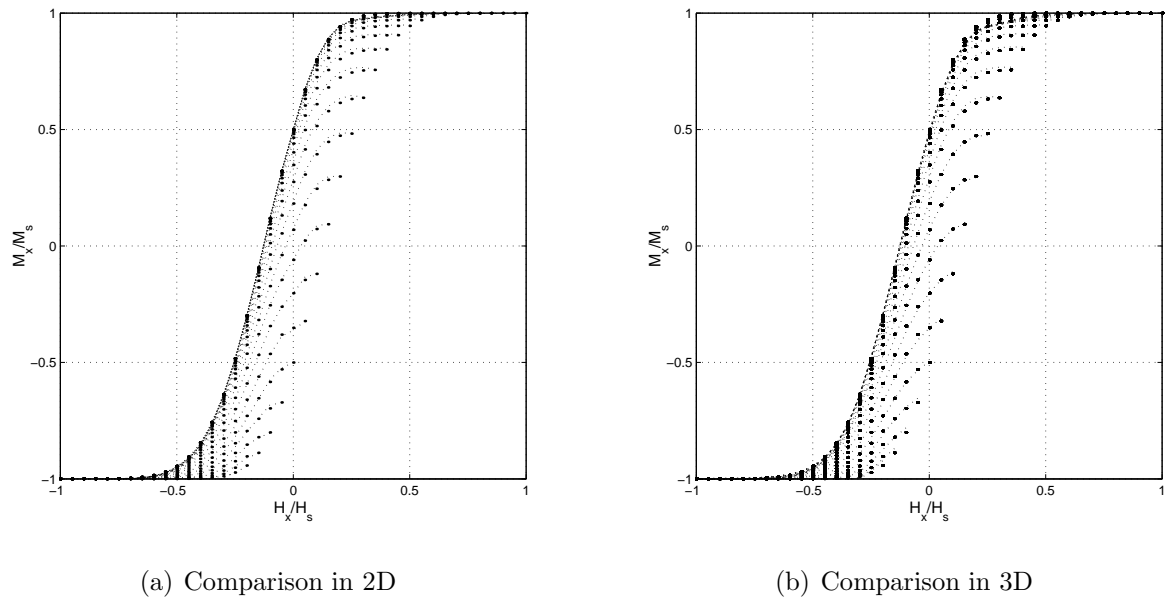


Fig. 3.13. Identification results for isotropic case

between measured (denoted by points) and simulated first order reversal curves by the identified 2D and 3D models (denoted by dotted line) can be seen in Fig. 3.13(a) and Fig. 3.13(b).

Some other verification and comparisons with the anisotropic model are presented at the end of this chapter.

3.3 The anisotropic vector hysteresis operator

The anisotropic vector NN based model of magnetic hysteresis is also constructed as a superposition of scalar NN based models in the directions \mathbf{e}_φ , but these scalar hysteresis characteristics are not the same. The magnetization vector \mathbf{M} can be expressed in two dimensions as (see Fig. 3.8)

$$\mathbf{M} = \int_{-\pi/2}^{\pi/2} \mathbf{e}_\varphi \mathcal{H}_\varphi\{H_\varphi\} d\varphi. \quad (3.25)$$

In three dimensions a similar expression can be obtained (see Fig. 3.9(a)):

$$\mathbf{M} = \int_{-\pi/2}^{\pi/2} \int_{-\pi/2}^{\pi/2} \mathbf{e}_{\varphi,\vartheta} \mathcal{H}_{\varphi,\vartheta}\{H_{\varphi,\vartheta}\} d\varphi d\vartheta. \quad (3.26)$$

The main point of my research was to handle the angular dependence of the hysteresis characteristics, and applying the same identification process with minor modifications as used in the isotropic case. The Fourier expansion on the Everett surfaces can be used efficiently, when assuming uniaxial anisotropy.

3.3.1 Anisotropic model in 2D

I have assumed that, the scalar Everett function can be measured in any given direction. This is the scalar characterization of the vector hysteresis property. In this case, the following condition can be obtained between the measured scalar Everett function $F(\alpha, \beta, \varphi)$ and the unknown vector Everett function $E(\alpha, \beta, \varphi)$:

$$F(\alpha, \beta, \varphi) = \int_{-\pi/2}^{\pi/2} \cos \psi E(\alpha \cos \psi, \beta \cos \psi, \psi + \varphi) d\psi, \quad (3.27)$$

and this expression can be derived in a discretized form as

$$F(\alpha_k, \beta_l, \varphi_j) \cong \sum_{i=1}^{n'} \cos \psi_i E(\alpha_k \cos \psi_i, \beta_l \cos \psi_i, \varphi_i), \quad (3.28)$$

where $\psi_i = \varphi_i - \varphi_j$ is the angle between the direction of the measured scalar Everett function in the direction \mathbf{e}_{φ_j} and the unknown vector Everett function in the direction \mathbf{e}_{φ_i} . The identification process is based on n' directions, $\varphi_i \in [-\pi/2, \dots, \pi/2]$, selected as $\varphi_i = -\pi/2 + (i-1)\pi/n'$, where $i = 1, \dots, n'$. Assuming that the material has uniaxial anisotropy, the measured scalar Everett function must be π -periodic and an even function with respect to φ , if $\varphi = 0$ represents the rolling direction and $\varphi = \pi/2$ is perpendicular to the rolling direction (transverse direction), i.e.

$$F(\alpha_k, \beta_l, \varphi_j + \pi) = F(\alpha_k, \beta_l, \varphi_j), \quad (3.29)$$

and

$$F(\alpha_k, \beta_l, -\varphi_j) = F(\alpha_k, \beta_l, \varphi_j). \quad (3.30)$$

I supposed that, there are $n + 1$ measured Everett functions $F(\alpha_k, \beta_l, \varphi_j)$ in the interval $\varphi_j \in [0, \dots, \pi/2]$, $\varphi_j = j\Delta\varphi$, $\Delta\varphi = \pi/2n$ and $j = 0, \dots, n$, and n' is chosen as $n' = 2n$ as plotted in Fig. 3.14.

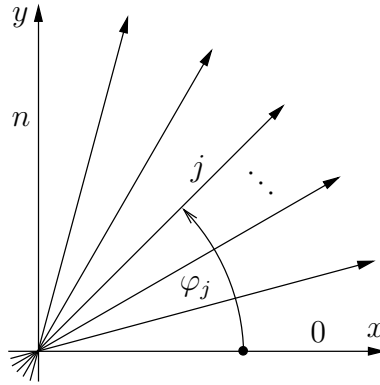
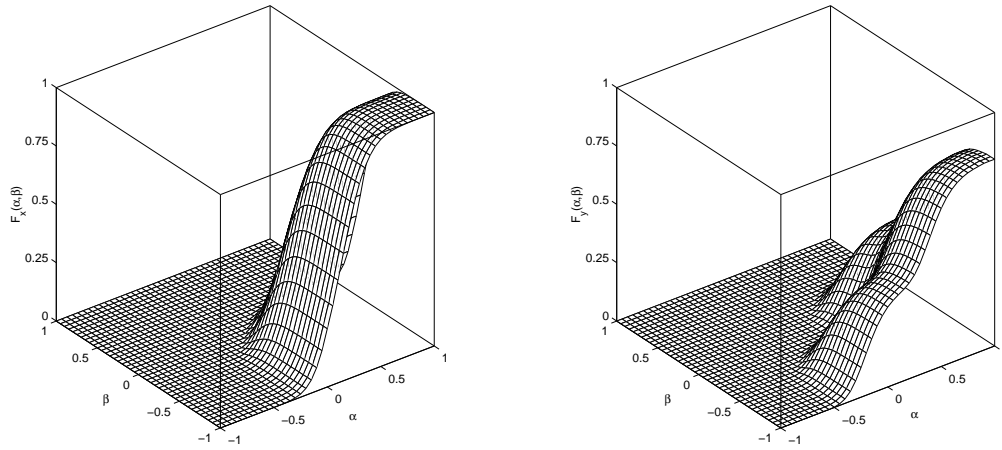


Fig. 3.14. The directions of the measured Everett functions $F(\alpha, \beta, \varphi)$



(a) The Everett function in the rolling direction, $\varphi = 0$

(b) The Everett function in the transverse direction, $\varphi = \pi/2$

Fig. 3.15. The measured Everett functions to build the 2D anisotropic vector hysteresis model in (3.31)

In my experiments, I assumed to have $n + 1 = 10$ scalar hysteresis characteristics, i.e. $\varphi_0 = 0^\circ$, $\varphi_1 = 10^\circ$, \dots , $\varphi_9 = 90^\circ$, generated by the elliptical interpolation function

$$F(\varphi) = F_x^2 \cos^2 \varphi + F_y^2 \sin^2 \varphi, \quad (3.31)$$

where $F(\varphi) = F(\alpha, \beta, \varphi)$, $F_x = F(\alpha, \beta, 0)$ and $F_y = F(\alpha, \beta, \pi/2)$ are the assumed normalized Everett functions in the rolling and in the transverse directions, respectively, and plotted in Fig. 3.15(a) and Fig. 3.15(b).

Due to the periodicity of the measured Everett function, it can be approximated by its Fourier series. It is difficult to take into account the angular dependence of the measured Everett function during the identification process, but the Fourier expansion is an accurate method to handle this phenomenon. Since $F(\alpha, \beta, \varphi)$ is an even function with respect to φ , only the real part of the complex Fourier series must be calculated (to make the equations below shorter, the following notation will be used: $F(\varphi_j) = F(\alpha_k, \beta_l, \varphi_j)$),

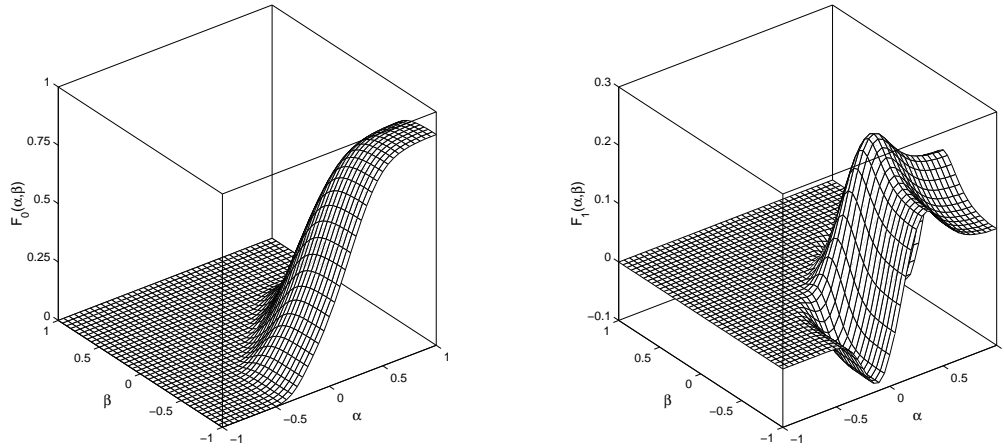
(a) The zeroth order harmonic component, F_0 (b) The first order harmonic component, F_1

Fig. 3.16. The Fourier coefficients of the measured 2D Everett surfaces

i.e.

$$F(\varphi_j) \simeq \sum_m F_m \cos(2m\varphi_j), \quad (3.32)$$

where $\omega = \frac{2\pi}{\pi} = 2$ is the angular frequency and the Fourier coefficients $F_m = F_m(\alpha_k, \beta_l)$ must be calculated. The subscript m is the number of Fourier coefficients and it can be maximum n . The Fourier coefficients have been calculated by their definition. The zeroth order component can be calculated as

$$F_0 = \frac{1}{\pi} \int_{-\pi/2}^{\pi/2} F(\varphi) d\varphi = \frac{2}{\pi} \int_0^{\pi/2} F(\varphi) d\varphi. \quad (3.33)$$

Integration has been performed numerically by the trapezoidal rule, i.e.

$$F_0 \simeq \frac{\Delta\varphi}{\pi} \left\{ F(0) + F\left(\frac{\pi}{2}\right) + 2 \sum_{j=1}^{n-1} F(\varphi_j) \right\}. \quad (3.34)$$

The higher order harmonics can be calculated as

$$F_m = \frac{2}{\pi} \int_{-\pi/2}^{\pi/2} F(\varphi) e^{-jm\omega\varphi} d\varphi = \frac{4}{\pi} \int_0^{\pi/2} F(\varphi) \cos(2m\varphi) d\varphi, \quad (3.35)$$

and applying numerical integration:

$$F_m \simeq \frac{2\Delta\varphi}{\pi} \left\{ F(0) + (-1)^m F\left(\frac{\pi}{2}\right) + 2 \sum_{j=1}^{n-1} F(\varphi_j) \cos(2m\varphi_j) \right\}. \quad (3.36)$$

By applying this approach, the angular dependence of the measured scalar Everett function has been handled, since the Fourier coefficients F_m are independent of the polar

angle. The second step is to find a relation between the measurement and the theoretical expressions, which can be found in the section 3.3.3.

By applying the zeroth (Fig. 3.16(a)) and only the first order (Fig. 3.16(b)) Fourier coefficients, the measured Everett functions in the directions of measurements can be approximated with a relative error as small as about 4% (this is the maximum value).

Increasing the number of directions of the measured scalar Everett functions results in better approximation between the directions of measurements. In this case, the relative error is smaller than 5 – 6% (e.g. in the direction 45°).

3.3.2 Anisotropic model in 3D

The 3D anisotropic vector hysteresis model is a theoretical generalization of the 2D anisotropic vector model, since there exists no well applicable method and measurement equipment to measure the 3D vector hysteresis property.

I have assumed that, the scalar Everett function can be measured in any directions, then the following condition (in discretized form) can be obtained between the measured scalar Everett function $F(\alpha_k, \beta_l, \varphi_{j_1}, \vartheta_{j_2})$ and the unknown vector Everett function $E(\alpha_k, \beta_l, \varphi_{i_1}, \vartheta_{i_2})$:

$$F(\alpha_k, \beta_l, \varphi_{j_1}, \vartheta_{j_2}) \cong \sum_{i_1=1}^{n'} \sum_{i_2=1}^{m'} \cos \psi_{i_1, i_2} E(\alpha_k \cos \psi_{i_1, i_2}, \beta_l \cos \psi_{i_1, i_2}, \varphi_{i_1}, \vartheta_{i_2}), \quad (3.37)$$

where ψ_{i_1, i_2} is the angle between the direction of the measured Everett function with direction φ_{j_1} and ϑ_{j_2} and the vector Everett function in the given direction signed by the angles φ_{i_1} and ϑ_{i_2} .

I have assumed the following properties while developing the model and the identification procedure. I supposed that, there are $(n + 1) \times (m + 1)$ measured scalar Everett functions $F(\varphi_{j_1}, \vartheta_{j_2}) = F(\alpha_k, \beta_l, \varphi_{j_1}, \vartheta_{j_2})$ in the interval $\varphi \in [0, \dots, \pi/2]$, $\varphi_{j_1} = j_1 \Delta\varphi$, $\Delta\varphi = \pi/2n$ and $j_1 = 0, \dots, n$, moreover $\vartheta \in [0, \dots, \pi/2]$, $\vartheta_{j_2} = j_2 \Delta\vartheta$, $\Delta\vartheta = \pi/2m$ and $j_2 = 0, \dots, m$, since the identification is constructed on $n' = 2n$ and $m' = 2m$ directions. The angles φ and ϑ are measured from the x -axis and from the $x - y$ plane, respectively. The measured scalar Everett function is π -periodic with respect to angles φ and ϑ , i.e.

$$F(\varphi_{j_1} + \pi, \vartheta_{j_2}) = F(\varphi_{j_1}, \vartheta_{j_2}), \quad (3.38)$$

$$F(\varphi_{j_1}, \vartheta_{j_2} + \pi) = F(\varphi_{j_1}, \vartheta_{j_2}). \quad (3.39)$$

The measured scalar Everett function is symmetrical with respect to the x -axis and the $x - y$ plane, i.e.

$$F(-\varphi_{j_1}, \vartheta_{j_2}) = F(\varphi_{j_1}, \vartheta_{j_2}), \quad (3.40)$$

$$F(\varphi_{j_1}, -\vartheta_{j_2}) = F(\varphi_{j_1}, \vartheta_{j_2}). \quad (3.41)$$

These are the simplest assumptions, and can be generalized.

I have assumed 5×5 measured scalar hysteresis characteristics, generated by the elliptical interpolation function

$$F(\varphi, \vartheta) = \cos^2 \vartheta (F_x^2 \cos^2 \varphi + F_y^2 \sin^2 \varphi) + F_z^2 \sin^2 \vartheta, \quad (3.42)$$

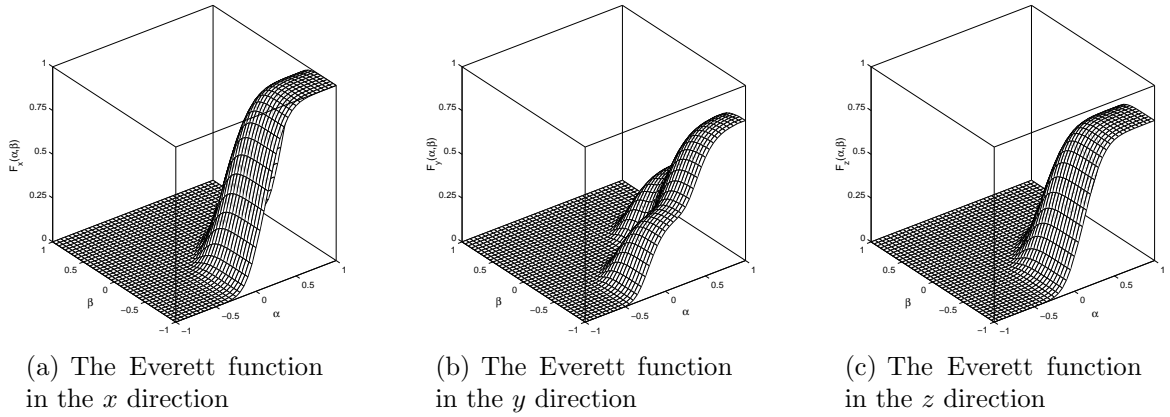


Fig. 3.17. The measured Everett functions to build the 3D anisotropic model in (3.42)

where $F(\varphi, \vartheta) = F(\alpha, \beta, \varphi, \vartheta)$, moreover $F_x = F(\alpha, \beta, 0, 0)$, $F_y = F(\alpha, \beta, \pi/2, 0)$, and $F_z = F(\alpha, \beta, 0, \pi/2)$ are the assumed normalized Everett functions in the x , y and z directions, and plotted in Fig. 3.17(a)–3.17(c).

The measured Everett function can also be approximated by its Fourier series due to the assumed periodicity. The measured Everett function is an even function with respect to the angles φ and ϑ , therefore only the real part of the complex Fourier series must be calculated as

$$F(\varphi_{j_1}, \vartheta_{j_2}) \simeq \sum_{n_1} \sum_{m_1} F_{n_1 m_1} \cos(2n_1 \varphi_{j_1}) \cos(2m_1 \vartheta_{j_2}), \quad (3.43)$$

where $F_{n_1 m_1} = F_{n_1 m_1}(\alpha_k, \beta_l)$ are the Fourier coefficients. The maximum value of n_1 and m_1 can be n and m .

The zeroth order component F_{00} can be calculated by the integral

$$F_{00} = \frac{1}{\pi^2} \int_{-\pi/2}^{\pi/2} \int_{-\pi/2}^{\pi/2} F(\varphi, \vartheta) d\varphi d\vartheta = \frac{4}{\pi^2} \int_0^{\pi/2} \int_0^{\pi/2} F(\varphi, \vartheta) d\varphi d\vartheta. \quad (3.44)$$

The following expression can be obtained by applying the trapezoidal rule:

$$\begin{aligned} F_{00} \simeq & \frac{\Delta\varphi\Delta\vartheta}{\pi^2} \left\{ F(0, 0) + F\left(0, \frac{\pi}{2}\right) + F\left(\frac{\pi}{2}, 0\right) + F\left(\frac{\pi}{2}, \frac{\pi}{2}\right) \right. \\ & + 2 \sum_{j_1=1}^{n-1} \left(F(\varphi_{j_1}, 0) + F\left(\varphi_{j_1}, \frac{\pi}{2}\right) \right) \\ & \left. + 2 \sum_{j_2=1}^{m-1} \left(F(0, \vartheta_{j_2}) + F\left(\frac{\pi}{2}, \vartheta_{j_2}\right) \right) + 4 \sum_{j_1=1}^{n-1} \sum_{j_2=1}^{m-1} F(\varphi_{j_1}, \vartheta_{j_2}) \right\}. \end{aligned} \quad (3.45)$$

The harmonic components can be calculated by the definition as well, i.e.

$$\begin{aligned} F_{n_1 m_1} &= \frac{2}{\pi^2} \int_{-\pi/2}^{\pi/2} \int_{-\pi/2}^{\pi/2} F(\varphi, \vartheta) e^{-jn_1\omega\varphi} e^{-jm_1\omega\vartheta} d\varphi d\vartheta \\ &= \frac{8}{\pi^2} \int_0^{\pi/2} \int_0^{\pi/2} F(\varphi, \vartheta) \cos(2n_1\varphi) \cos(2m_1\vartheta) d\varphi d\vartheta, \end{aligned} \quad (3.46)$$

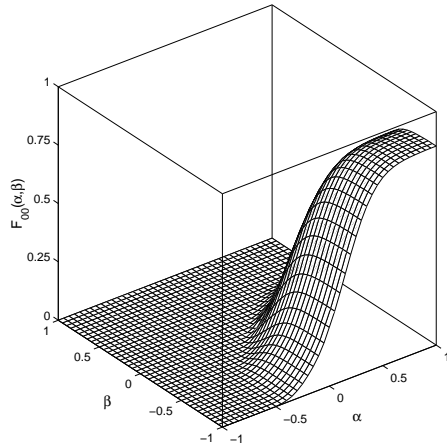
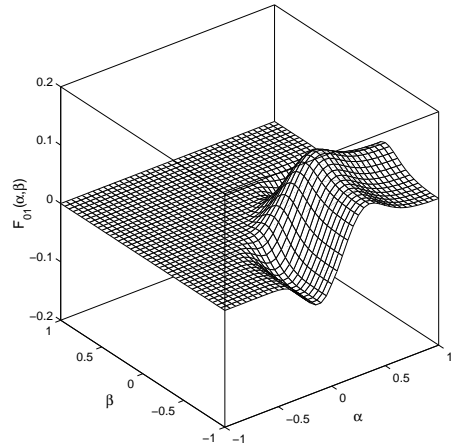
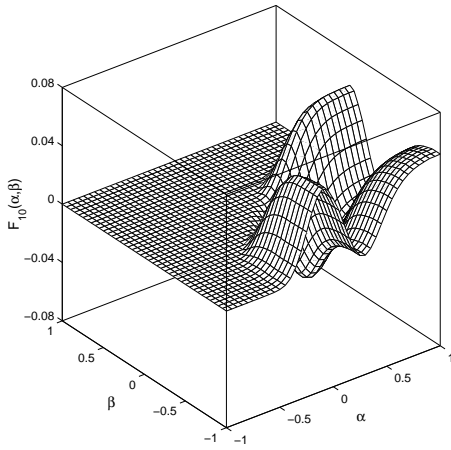
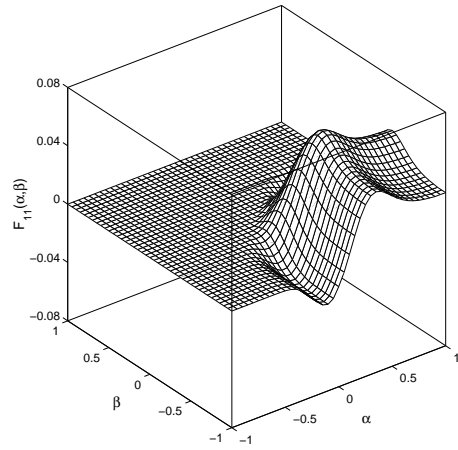
(a) The zeroth order harmonic component, F_{00} (b) The first order harmonic component, F_{01} (c) The first order harmonic component, F_{10} (d) The first order harmonic component, F_{11}

Fig. 3.18. The Fourier coefficients of the measured 3D Everett surfaces

and numerically

$$\begin{aligned}
 F_{n_1 m_1} \simeq & 2 \frac{\Delta\varphi\Delta\vartheta}{\pi^2} \left\{ F(0,0) + F\left(0, \frac{\pi}{2}\right) (-1)^{n_1} \right. \\
 & + F\left(\frac{\pi}{2}, 0\right) (-1)^{m_1} + F\left(\frac{\pi}{2}, \frac{\pi}{2}\right) (-1)^{n_1+m_1} \\
 & + 2 \sum_{j_1=1}^{n-1} \left(F(\varphi_{j_1}, 0) + F\left(\varphi_{j_1}, \frac{\pi}{2}\right) (-1)^{m_1} \right) \cos(2n_1\varphi_{j_1}) \\
 & + 2 \sum_{j_2=1}^{m-1} \left(F(0, \vartheta_{j_2}) + F\left(\frac{\pi}{2}, \vartheta_{j_2}\right) (-1)^{n_1} \right) \cos(2m_1\vartheta_{j_2}) \\
 & \left. + 4 \sum_{j_1=1}^{n-1} \sum_{j_2=1}^{m-1} F(\varphi_{j_1}, \vartheta_{j_2}) \cos(2n_1\varphi_{j_1}) \cos(2m_1\vartheta_{j_2}) \right\}. \tag{3.47}
 \end{aligned}$$

The Fourier coefficients $F_{n_1 m_1}$ are independent of the angles φ and ϑ .

By applying the zeroth F_{00} and only the first order Fourier coefficients F_{01} , F_{10} and F_{11} , the measured Everett functions along the directions of the measurements can be approximated with a relative error as small as about maximum 5 – 6%. The calculated Fourier coefficients are plotted in Fig. 3.18(a)–3.18(d).

3.3.3 The relation between the scalar and the vector Everett functions

The angle dependence of the measured scalar Everett function can be handled by applying the Fourier series, but a relation between the scalar and the vector Fourier coefficients must be developed. This gives the basic expression of the identification procedure.

Authors of [78] used the distribution function of the classical Preisach model. Here, I use the Everett function, because this is the basis of the NN based vector hysteresis model.

The identification task of the 2D model is based on the integral equation

$$F(\alpha, \beta, \varphi) = \int_{-\pi/2}^{\pi/2} \cos \psi E(\alpha \cos \psi, \beta \cos \psi, \psi + \varphi) d\psi, \quad (3.48)$$

where the measured scalar Everett function along an angle φ , $F(\alpha, \beta, \varphi)$ must be equal to the projected sum of the vector Everett functions $E(\alpha, \beta, \psi + \varphi)$. Unfortunately, the unknown vector Everett function is placed on the right hand side of this integral equation.

The 2D vector Everett function $E(\varphi) = E(\alpha, \beta, \varphi)$ also depends on the polar angle φ , and it can also be approximated by its Fourier series by assuming the same conditions as used for the measured Everett function $F(\alpha, \beta, \varphi)$, i.e.

$$E(\varphi) \simeq \sum_m E_m \cos(2m\varphi). \quad (3.49)$$

Substituting the Fourier series (3.32) and (3.49) into the integral equation (3.48), the following equation can be obtained:

$$\begin{aligned} \sum_m F_m(\alpha, \beta) \cos(2m\varphi) &= \int_{-\pi/2}^{\pi/2} \cos \psi \sum_m E_m(\alpha \cos \psi, \beta \cos \psi) \\ &\times \cos(2m(\psi + \varphi)) d\psi, \end{aligned} \quad (3.50)$$

and this equation can be rewritten in the form

$$\begin{aligned} \sum_m F_m(\alpha, \beta) \cos(2m\varphi) &= \int_{-\pi/2}^{\pi/2} \cos \psi \sum_m E_m(\alpha \cos \psi, \beta \cos \psi) \\ &\times \cos(2m\psi) \cos(2m\varphi) d\psi \\ &- \int_{-\pi/2}^{\pi/2} \cos \psi \sum_m E_m(\alpha \cos \psi, \beta \cos \psi) \\ &\times \sin(2m\psi) \sin(2m\varphi) d\psi \end{aligned} \quad (3.51)$$

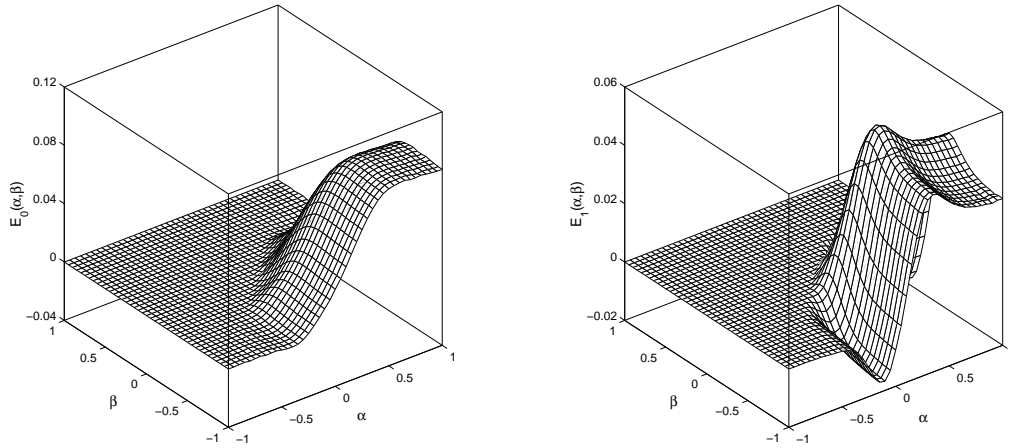
(a) The zeroth order harmonic component, E_0 (b) The first order harmonic component, E_1

Fig. 3.19. The identified vector Fourier coefficients in 2D

by applying the mathematical formulation $\cos(2m(\psi + \varphi)) = \cos(2m\psi) \cos(2m\varphi) - \sin(2m\psi) \sin(2m\varphi)$. The second term is equal to zero, because the integrand is an odd function with respect to ψ , i.e.

$$\sum_m F_m(\alpha, \beta) \cos(2m\varphi) = \sum_m \left\{ \int_{-\pi/2}^{\pi/2} \cos \psi \cos(2m\psi) \times E_m(\alpha \cos \psi, \beta \cos \psi) d\psi \right\} \cos(2m\varphi). \quad (3.52)$$

The identification procedure is then based on the following integral equation which links the m^{th} harmonic components of the unknown vector Everett function to the corresponding scalar one, i.e.

$$F_m(\alpha, \beta) = \int_{-\pi/2}^{\pi/2} \cos \psi \cos(2m\psi) E_m(\alpha \cos \psi, \beta \cos \psi) d\psi. \quad (3.53)$$

In this case, the identification procedure developed for the isotropic vector model can also be applied, but the $\cos(2m\psi)$ term must be included. Identification results of the zeroth and the first order harmonics of the 2D vector Everett function can be seen in Fig. 3.19(a) and Fig. 3.19(b).

In the 3D case, a similar mathematical formulation can be used which leads to the following equation, that is the basis of the identification task,

$$F_{n_1 m_1}(\alpha, \beta) \cong \sum_{i=1}^{n'} \cos \psi_i \cos(2n_1 \varphi_i) \cos(2m_1 \vartheta_i) \times E_{n_1 m_1}(\alpha \cos \psi_i, \beta \cos \psi_i), \quad (3.54)$$

where angle ψ_i is the angle between a direction generated by the icosahedron and the

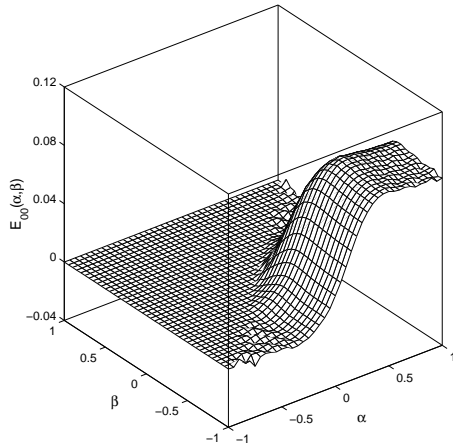
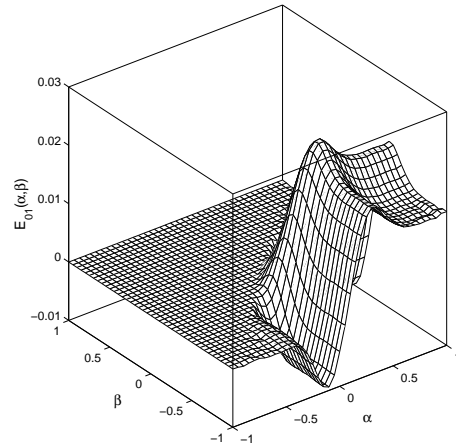
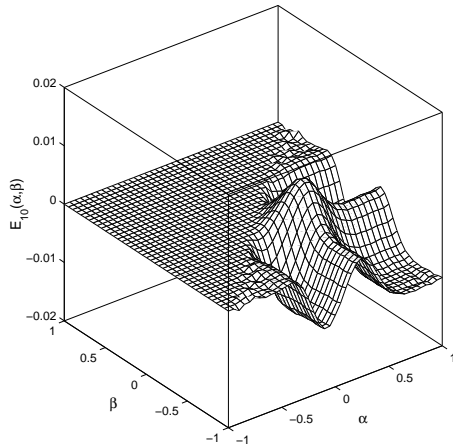
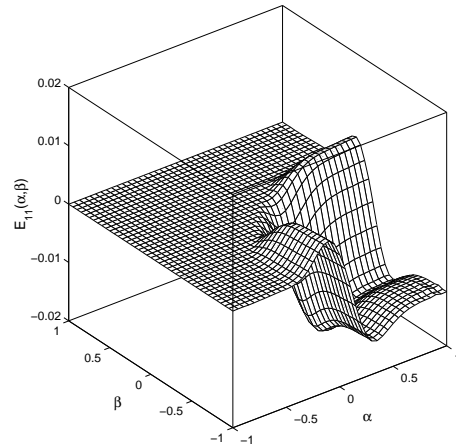
(a) The zeroth order harmonic component, E_{00} (b) The first order harmonic component, E_{01} (c) The first order harmonic component, E_{10} (d) The first order harmonic component, E_{11}

Fig. 3.20. The identified vector Fourier coefficients in 3D

x -axis. In this case, equation (3.37) should be rewritten in a simplified form,

$$F(\alpha_k, \beta_l, \varphi_j, \vartheta_j) \cong \sum_{i=1}^{n'} \cos \psi_i E(\alpha_k \cos \psi_i, \beta_l \cos \psi_i, \varphi_i, \vartheta_i), \quad (3.55)$$

where n' is replaced by $n' \cdot m'$. The four identified Fourier series of the vector Everett function are plotted in Fig. 3.20(a)–3.20(d).

From the Fourier coefficients of the vector Everett function, the Everett functions in all directions (e.g. 9 directions generated by the icosahedron) as well as the first order reversal curves can be calculated, then NNs can be trained. It is obvious that, different NNs must be trained in different directions.

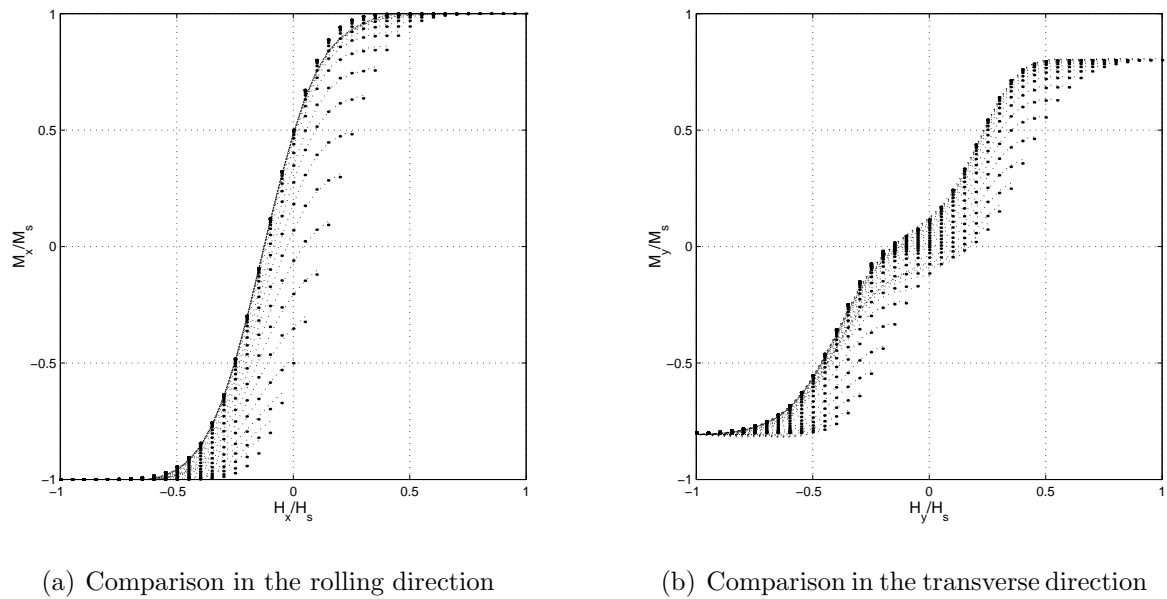


Fig. 3.21. The resulting identification in 2D, anisotropic case

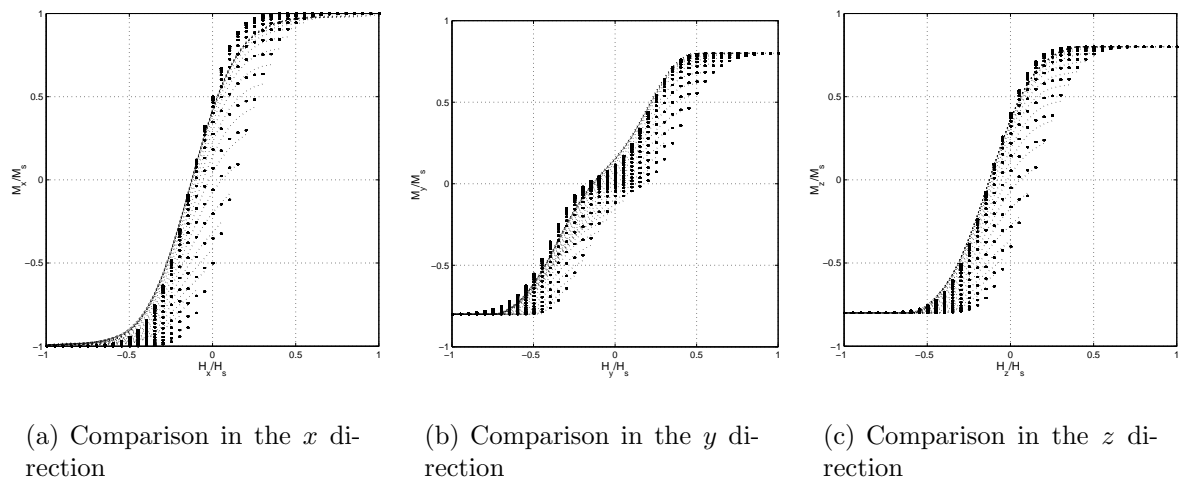
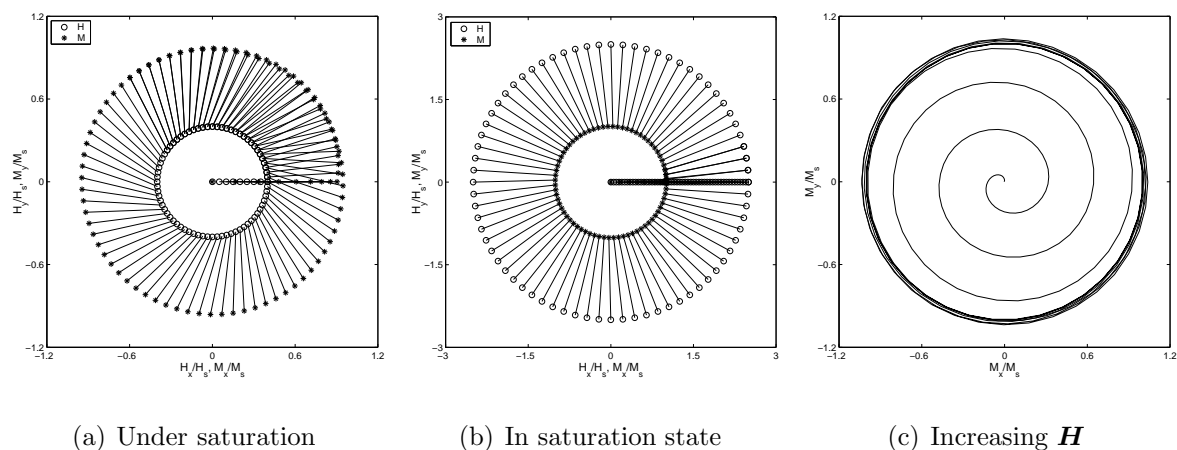
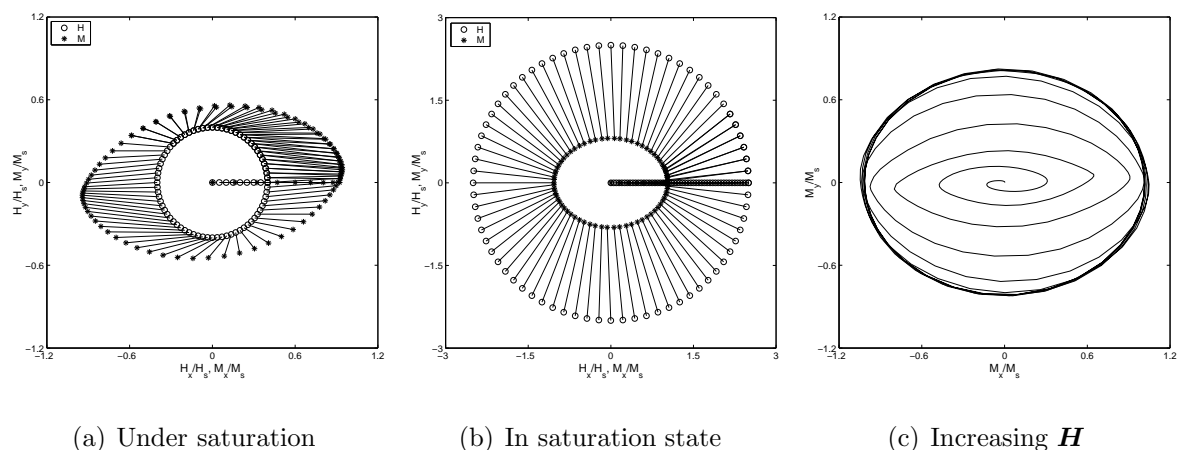


Fig. 3.22. The resulting identification in 3D, anisotropic case

Simulation results –trivial conditions in the directions of the x , of the y and of the z axis– for the reversal curves obtained from the identified Everett functions in two dimensions (18 directions) and in three dimensions (9 directions) can be seen in Fig. 3.21(a), Fig. 3.21(b) and Fig. 3.22(a)–3.22(c). The experimental results are denoted by points, the hysteresis characteristics given by the NN based vector model are denoted by dotted line. Increasing the number of directions results in a better approximation, but at the same time in slower model. If I use the 3D NN based vector hysteresis model in a finite element software, then I have to make a compromise.

Fig. 3.23. Simulated H and M loci of the rotational process in the isotropic caseFig. 3.24. Simulated H and M loci of the rotational process in the anisotropic case

3.4 Some properties of the vector hysteresis characteristics

In this section, I present some cases which can characterize the behavior of the vector model prescribed above.

Applying an anticlockwise rotational magnetic field intensity with different amplitude and with linearly increasing amplitude, the output of the 2D vector models (isotropic and anisotropic models) have been plotted in Fig. 3.23(a)–3.23(c), and in Fig. 3.24(a)–3.24(c). The specimen is magnetized to a given value in the direction of the x -axis, and the magnetic field intensity is then rotated keeping its magnitude constant. In Fig. 3.23(c), and in Fig. 3.24(c), the vector of the magnetization is gradually approaching the regime of the uniform rotation, since the amplitude of the magnetic field intensity is increasing during the polarization cycle. The magnetization vector has some delay in comparison with the angle of the magnetic field intensity vector, especially in the case, when the magnetic field intensity is lower than in the saturation state. Increasing the magnitude of the magnetic field intensity results in decreasing the phase between

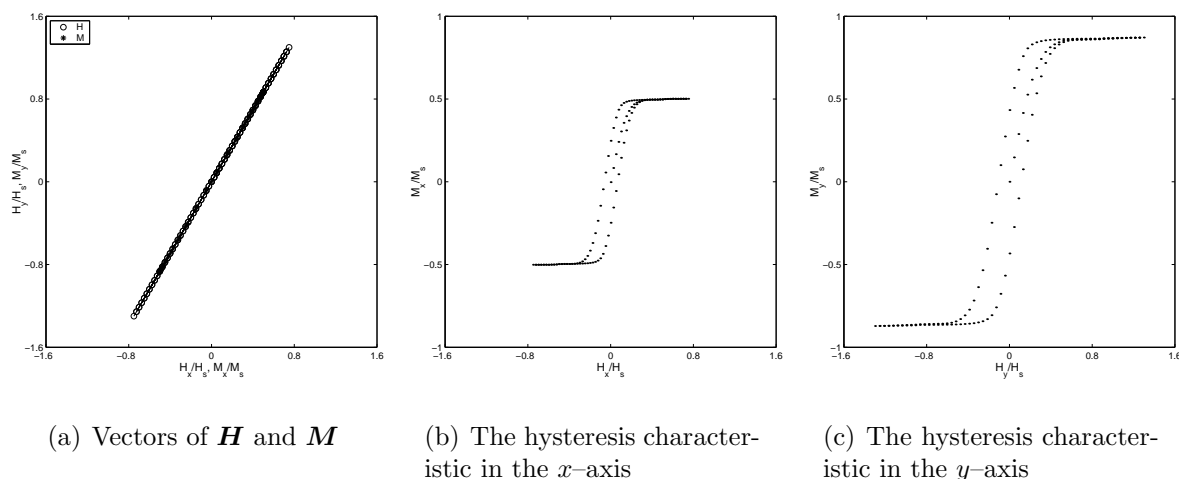


Fig. 3.25. The simulated \mathbf{H} and \mathbf{M} loci of the linear excitation in the isotropic case

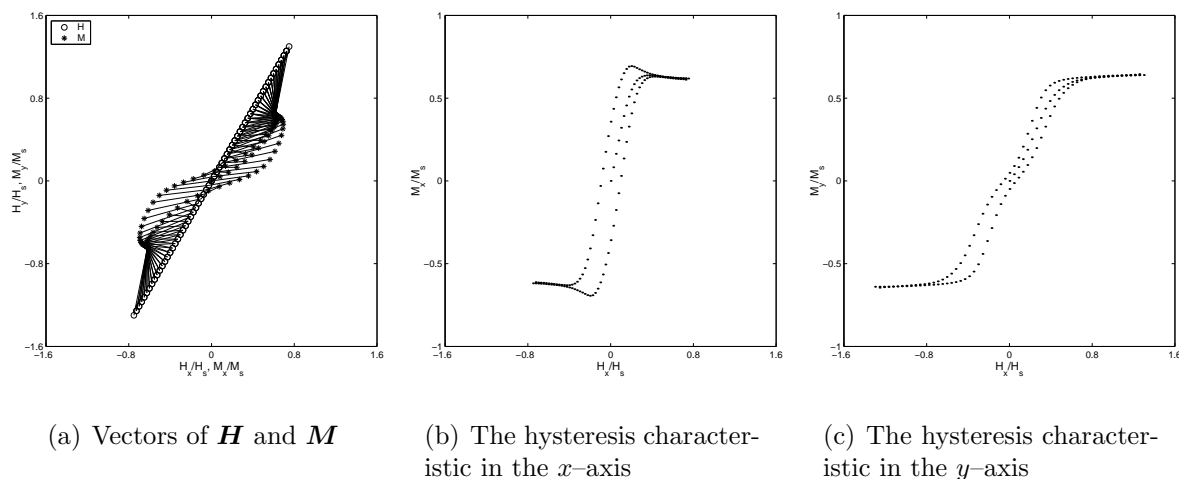


Fig. 3.26. The simulated \mathbf{H} and \mathbf{M} loci of the linear excitation in the anisotropic case

the magnetization and the magnetic field intensity vectors. Higher above the saturation state, they rotate together. In the figures yielded by the anisotropic model, the anisotropic behavior can be seen easily, because the amplitude of magnetization in the y -axis is smaller than in the x -axis and the delay between the magnetic field intensity and magnetization vectors is larger.

In the second test case, the magnetic field intensity vector has applied in a linear variation ($\vartheta_H = 60^\circ$). In isotropic case, the magnetic field intensity and the magnetization vectors are parallel as plotted in Fig. 3.25(a)–3.25(c), but in anisotropic case (see Fig. 3.26(a)–3.26(c)) there is an angle between them, because of the anisotropic behavior: the magnetization vector tries to be close to the x -axis. The projected hysteresis characteristics in the x -axis and in the y -axis are also presented. The hysteresis characteristics in the x -axis and in the y -axis are similar in the isotropic case, but the shape of the characteristics is very different in the anisotropic case.

Anisotropic behavior of the isotropic model induced by the remanent magnetization can be observed as well. Let us suppose that, the magnetic field intensity is first increased

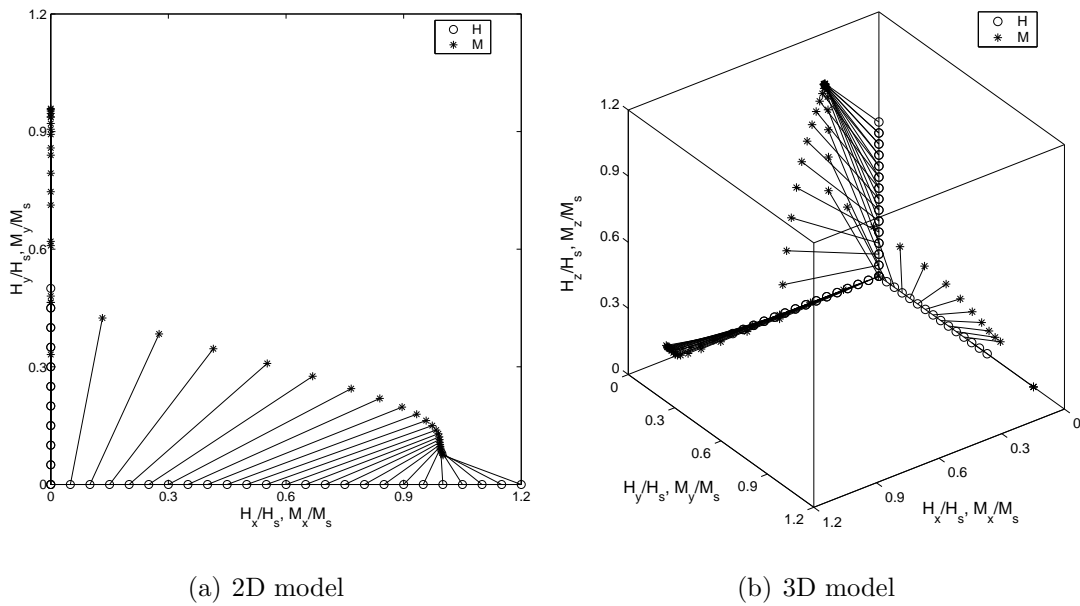


Fig. 3.27. The induced anisotropy in isotropic material

in the y direction to a given value, and then it is decreased to zero. This process results in a remanent magnetization in the y direction. After reaching the remanent magnetization, the magnetic field intensity is increased in the x direction. The orthogonal remanent magnetization can be reduced as presented in the Fig. 3.27(a). In the 3D case, a similar magnetization process can be applied with similar simulation results, e.g. the magnetic field intensity is increased and then decreased in the x direction resulting remanent magnetization in the x direction, then increased and then decreased in the z direction, and finally increased in the y direction. This process can be seen in Fig. 3.27(b).

Using a large number of directions results better approximation, but the calculations may be time consuming. Smaller number of directions gives higher error between measured and simulated curves, however the model is faster. To make a compromise, the presented model with given number of directions can be used in Computer Aided Design software tools (e.g. in the Finite Element Method) with a given accuracy which is acceptable as illustrated in the figures of this chapter.

3.5 New scientific results

1. Thesis I have developed a new scalar hysteresis operator based on the function approximation capability of the neural networks to simulate the behavior of ferromagnetic materials. I have represented the first order reversal curves with a surface by introducing the variable ξ and I have approximated this surface by neural network technique. I have built a knowledge-base which contains if-then type rules about the behavior of the hysteresis characteristics. I have shown the applicability of the model by comparing simulated and measured results. I have taken into account the vectorial behavior of the magnetic field intensity and the magnetic flux density by applying the neural network based vector hysteresis model, and I have recommended a new identification procedure to build up the vector model. I have worked out the three dimensional anisotropic vector

hysteresis model, and I have analyzed the behavior of the developed vector models.

- 1.a I have developed a new neural network based mathematical representation of the scalar hysteresis operator. I have handled the multivalued property of the hysteresis characteristics by introducing the new variable ξ associated with the measured first order reversal curves. This preprocessing can be applied on any kind of hysteresis characteristics. I have built a knowledge-base which contains if-then type rules about the behavior of the hysteresis characteristics. This is the memory mechanism of the model. I have realized the identification procedure by the training of the neural networks. I have built a measurement system to measure hysteresis curves on a toroidal shape C19 structural steel, and I have used these measurements to show the applicability of the neural network based scalar hysteresis model by comparing measurements and simulation results.
- 1.b I have developed the two dimensional and the three dimensional isotropic vector hysteresis models based on the neural network based scalar model. I have worked out an original and new identification procedure based on the measurable Everett function both to predict two dimensional and three dimensional isotropic hysteresis characteristics. I have compared the measured and the predicted curves and I have shown the behavior of the vector model in linear and in rotational magnetic fields.
- 1.c I have developed the two dimensional and the three dimensional neural network based anisotropic vector hysteresis models by the means of Fourier expansion of the measured Everett function of the anisotropic material. I have generalized the two dimensional model in three dimensions as a theoretical expansion of the two dimensional model, and I have recommended an identification procedure to fit to measured curves. I have compared the measured and the predicted curves and I have shown the behavior of the vector model in linear and in rotational magnetic fields, finally I have compared the isotropic and the anisotropic models.

Chapter 4

Nonlinear FEM using edge finite elements

In this chapter, I present the $\mathbf{T}, \Psi - \Psi$ potential formulation [6, 21] in the time domain using the FEM. I have developed the 3D numerical simulation of the built NDT equipment presented in the next chapter. First of all, I have solved a similar 2D problem, then the 3D simulation of the NDT equipment.

This chapter deals with the mathematical formulations of the time varying magnetic field problem and of the eddy current field problem and I present the simulation of a 2D arrangement. The same nonlinear partial differential equations, weak forms, boundary conditions and iteration scheme can be used to solve the 3D problem. The simulated NDT arrangement with measurements and simulation results are presented in the next chapter. The hysteresis characteristic of the magnetic material has been simulated by the introduced NN based isotropic vector hysteresis model. The nonlinear system of equations has been solved by the fixed-point iteration scheme [11, 17, 24, 49, 77]. In 2D triangular finite elements, in 3D tetrahedral finite elements have been used.

4.1 Problem definition and the FEM formulation

I have used the nodal and the edge finite elements to approximate the scalar and the vector potentials. The partial differential equations have been solved in the time domain, because the effect of hysteresis characteristic of the material has been taken into consideration. I have applied the $\mathbf{T}, \Psi - \Psi$ potential formulation, since this directly obtains the magnetic field intensity vector \mathbf{H} , so I could apply the direct vector hysteresis operator, i.e. $\mathbf{B} = \mathcal{H}\{\mathbf{H}\}$.

I have solved the problem through the following steps: first of all, I have solved a time varying magnetic field problem, then an eddy current field problem in linear media, finally I have inserted an identified isotropic NN based vector hysteresis operator into the FEM procedure. I have developed the simulations myself in the frame of MATLAB.

A simple 2D arrangement (see Fig. 4.1) has been examined as a case study [58]. The major steps and equations are presented by this example. The region Ω_c is filled by the yoke's material bounded by the boundary Γ_c . The yoke is in the air, Ω_n , bounded by the artificial far boundary Γ_n . The interface between the yoke and the air is denoted by Γ_{nc} . The excitation current is placed in the air region. The whole problem region is denoted by $\Omega = \Omega_c \cup \Omega_n$.

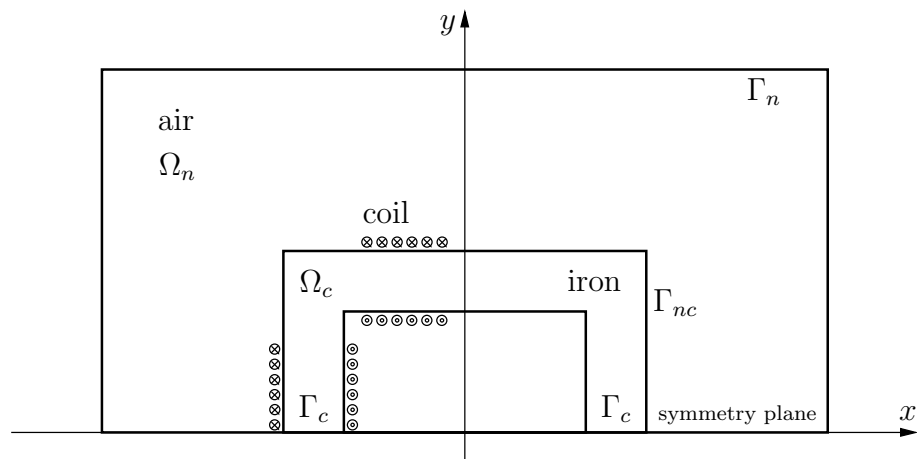


Fig. 4.1. Sketch of the solved 2D problem, a case study

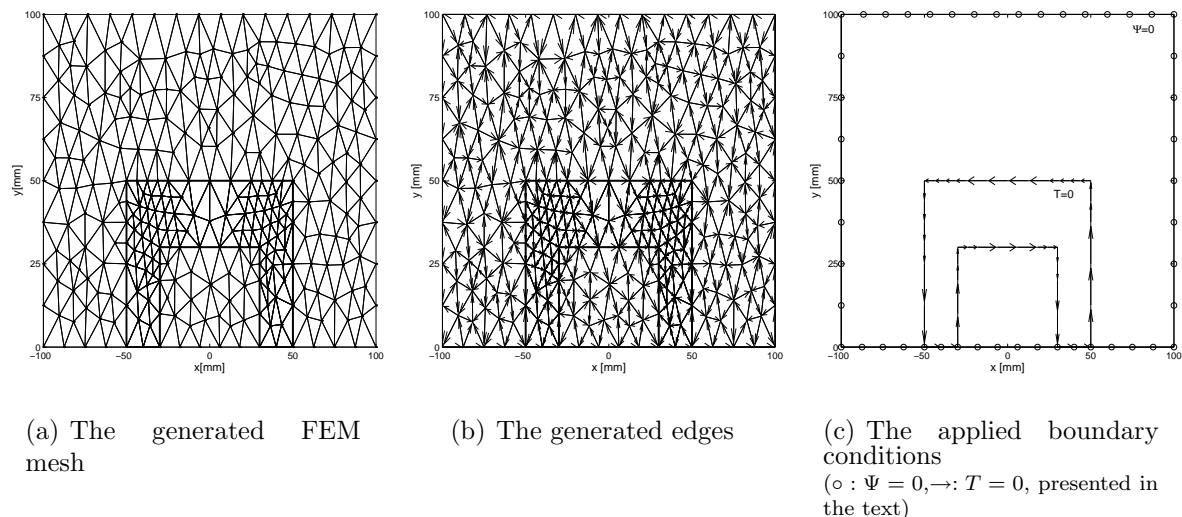


Fig. 4.2. The generated mesh of the 2D problem

The example contains a closed yoke made of iron with excitation coils under a given waveform of current. First, the characteristic of the yoke is linear, then the hysteresis characteristic of the yoke's material has been taken into consideration. Only the half of the arrangement has been analyzed, because this is symmetrical with respect to the line $y = 0$. The generated FEM mesh has been finalized after some preliminary simulations, and it contains 299 nodes, 548 finite elements (Fig. 4.2(a), the size of the arrangement also can be seen in this figure) and 846 edges (Fig. 4.2(b)). The generated mesh is a Delaunay-type mesh. The applied boundary conditions can be seen in Fig. 4.2(c) [6, 21] and presented below in the text.

4.1.1 Time varying magnetic field problem in linear media

As the simplest case, the closed yoke made of linear magnetic material with a given relative permeability μ_r is placed into air. The excitation is a coil wound around the yoke with sinusoidal time function of current $i(t)$.

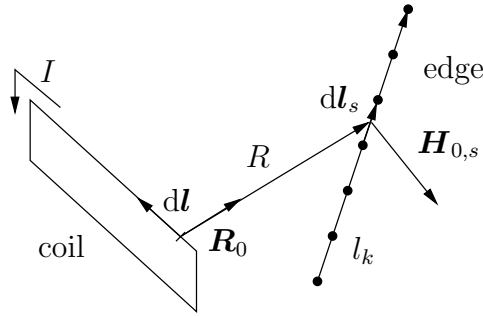


Fig. 4.3. Magnetic field intensity along edges can be determined by the Biot-Savart law

The basic equations of a time varying magnetic field problem to be solved are as follows:

$$\nabla \times \mathbf{H} = \mathbf{J}_0, \quad (4.1)$$

$$\nabla \cdot \mathbf{B} = 0, \quad (4.2)$$

$$\mathbf{B} = \mu \mathbf{H}, \quad (4.3)$$

where \mathbf{H} is the magnetic field intensity, \mathbf{B} is the magnetic flux density, \mathbf{J}_0 is the current density of the exciting current and μ is the permeability (in air, μ is equal to the vacuum permeability $\mu_0 = 4\pi \cdot 10^{-7} \frac{Vs}{Am}$, and $\mu = \mu_0 \mu_r$ inside the linear magnetic material and $\mu_r = 1000$ is used). Field quantities are depending on time and space, i.e. $\mathbf{H} = \mathbf{H}(\mathbf{r}, t)$.

The boundary conditions of the time varying magnetic field problem can be given at the artificial far boundaries of the air region Γ_n , where homogeneous boundary conditions are assumed, i.e. the tangential component of the magnetic field intensity or the normal component of the magnetic flux density is zero, $\mathbf{H} \times \mathbf{n} = \mathbf{0}$ or $\mathbf{B} \cdot \mathbf{n} = 0$, where \mathbf{n} is the outer normal unit vector of the region. Homogeneous boundary conditions can be supposed along the symmetry planes (a part of Γ_n and Γ_c): $\mathbf{H} \times \mathbf{n} = \mathbf{0}$. On the interface between the yoke and the air Γ_{nc} , the interface conditions must be satisfied: $\mathbf{H} \times \mathbf{n}$ and $\mathbf{B} \cdot \mathbf{n}$ must be continuous.

The effect of the current density of the coil \mathbf{J}_0 can be described by an impressed field quantity, i.e. by the known current vector potential \mathbf{T}_0 derived from $\nabla \cdot \mathbf{J}_0 = 0$ as [6,21]

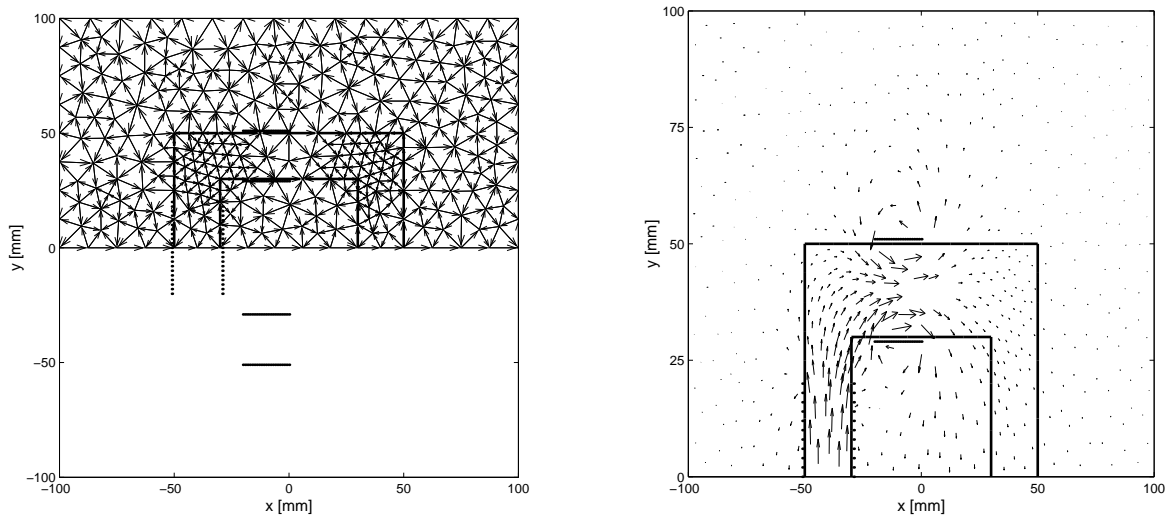
$$\mathbf{J}_0 = \nabla \times \mathbf{T}_0, \quad (4.4)$$

where \mathbf{T}_0 can be obtained by using the Biot-Savart law. The impressed field quantity can be calculated according to the line integral (2.29), i.e. the line integral of the magnetic field intensity in free space \mathbf{H}_0 along an edge l_k gives the line integrals of \mathbf{T}_0 along the k^{th} edge, i.e.

$$T_{0,k} = \int_{l_k} \mathbf{H}_0 \cdot d\mathbf{l}, \quad (4.5)$$

where $k = 1, \dots, N_e$, and N_e is the number of the edges ($\mathbf{T}_0 \equiv \mathbf{H}_0$). This is used in (4.12). Numerically, every edge should be divided into some line segments with the unit vector $d\mathbf{l}_s$ as presented in Fig. 4.3, then the magnetic field intensity $\mathbf{H}_{0,s}$ can be calculated at the center point of such segments, finally the values of scalar products $\mathbf{H}_{0,s} \cdot d\mathbf{l}_s$ have to be summed. The magnetic field intensity can be calculated as

$$\mathbf{H}_{0,s} = \frac{I}{4\pi} \oint_{l_{coil}} \frac{d\mathbf{l} \times \mathbf{R}_0}{R^2}. \quad (4.6)$$



(a) The potential \mathbf{T}_0 must be calculated by using the whole coil's geometry

(b) The magnetic field intensity of the coil in free space satisfies the symmetry conditions

Fig. 4.4. Construction of the current vector potential \mathbf{T}_0

In 2D case, \mathbf{H}_0 can be calculated as the superposition of the magnetic field intensity of infinite long wires, i.e. $H = I/(2r\pi)$, where r is the distance between a given point in the space, where the magnetic field intensity must be calculated and the wire.

This gives an interpolation of \mathbf{T}_0 by applying the edge element based shape functions, so the geometry of the exciting coil need not be included in the FEM mesh. The function \mathbf{T}_0 must satisfy the symmetry conditions on the symmetry planes as illustrated in Fig. 4.4(a), meaning that, the magnetic field intensity of the current of the whole conductor must be calculated. The magnetic field intensity of the exciting current in free space can be seen in Fig. 4.4(b). The exciting current is equal to 1 A, and the resulting function of \mathbf{T}_0 can be applied to determine the effect of currents of any value.

Substituting (4.4) into the Maxwell's equation (4.1), the magnetic scalar potential Ψ can be defined as

$$\mathbf{H} = \mathbf{T}_0 - \nabla\Psi. \quad (4.7)$$

Writing equation (4.7) into (4.2) and using the constitutive relation (4.3), the partial differential equation to be solved can be formulated as

$$\nabla \cdot \{\mu\mathbf{T}_0 - \mu\nabla\Psi\} = 0. \quad (4.8)$$

It must be solved in the problem region Ω .

According to the method of weighted residuals, the partial differential equation (4.8) can be multiplied by the weighting function N_j and must be integrated over the region Ω , i.e.

$$\int_{\Omega} N_j \nabla \cdot \{\mu\mathbf{T}_0 - \mu\nabla\Psi\} d\Omega = 0. \quad (4.9)$$

Applying the mathematical identity $\nabla \cdot (u\mathbf{v}) = \mathbf{v} \cdot \nabla u + u(\nabla \cdot \mathbf{v})$, and substituting

$u = N_j$ and $\mathbf{v} = \mu \mathbf{T}_0 - \mu \nabla \Psi$, and using the Gauss law, leads to the equation

$$- \int_{\Omega} \nabla N_j \cdot \{ \mu \mathbf{T}_0 - \mu \nabla \Psi \} d\Omega + \oint_{\Gamma} N_j \{ \mu \mathbf{T}_0 - \mu \nabla \Psi \} \cdot \mathbf{n} d\Gamma = 0. \quad (4.10)$$

The boundary integral term is equal to zero, because $\mathbf{B} \cdot \mathbf{n} = 0$ on the artificial far boundary Γ_n , so the equation for one finite element is the following:

$$\mu \int_{\Omega_e} \nabla N_j \cdot \nabla \Psi d\Omega = \mu \int_{\Omega_e} \nabla N_j \cdot \mathbf{T}_0 d\Omega, \quad (4.11)$$

where Ω_e represents one finite element. In the case of FEM, the weighting function N_j is equal to the basis function of the nodal FEM.

The unknown magnetic scalar potential Ψ is approximated by linear nodal basis functions N_i , the known current vector potential \mathbf{T}_0 is approximated by linear edge basis functions \mathbf{W}_k as

$$\Psi \simeq \sum_{i=1}^I N_i \Psi_i, \quad \mathbf{T}_0 \simeq \sum_{k=1}^K \mathbf{W}_k T_{0,k}. \quad (4.12)$$

The number of degrees of freedom is $I = 3$, and $K = 3$ using triangular finite elements. For simplicity, the subscript h presented in sections 2.5.1 and 2.5.2 is omitted.

Substituting the approximation functions (4.12) into the weak formulation (4.11), the system of equations of one finite element can be derived as

$$\sum_{i=1}^I \left\{ \mu \int_{\Omega_e} \nabla N_j \cdot \nabla N_i d\Omega \right\} \Psi_i = \sum_{k=1}^K \left\{ \mu \int_{\Omega_e} \nabla N_j \cdot \mathbf{W}_k d\Omega \right\} T_{0,k}. \quad (4.13)$$

This system of equation contains I equations and $j = 1, \dots, I$. After assembling this system of equations, a system of equations (stored by using the sparse technique) can be obtained which contains as many unknowns as the number of nodes of the finite element mesh.

The magnetic scalar potential along the artificial boundary and along the symmetry plane is set to be zero. By using the nodal shape functions to approximate the unknown magnetic scalar potential, the interface conditions can be fulfilled automatically. The solution of this assembled system of equation gives the approximation of the unknown magnetic scalar potential Ψ .

Simulation results as comparisons with the results of the eddy current field problem are presented in the next section.

4.1.2 Eddy current field in linear media

The same closed iron yoke made of linear and conducting magnetic material with relative permeability μ_r and conductivity σ is placed into air ($\mu_r = 1000$ and $\sigma = 1/48 \cdot 10^8 S/m$). The excitation is the current flowing in the coil with sinusoidal function $i(t)$. The displacement current $\partial \mathbf{D} / \partial t$ is neglected. In time-varying case, electric and magnetic fields

are coupled as described by Maxwell's equations

$$\nabla \times \mathbf{H} = \mathbf{J}_0 + \mathbf{J}_e \equiv \mathbf{J}, \quad (4.14)$$

$$\nabla \times \mathbf{E} = -\dot{\mathbf{B}}, \quad (4.15)$$

$$\nabla \cdot \mathbf{B} = 0, \quad (4.16)$$

$$\mathbf{B} = \mu \mathbf{H}, \quad (4.17)$$

$$\mathbf{J} = \sigma \mathbf{E}, \quad (4.18)$$

where \mathbf{H} and \mathbf{E} are the magnetic and the electric field intensities, \mathbf{B} is the magnetic flux density, \mathbf{J}_0 is the current density of the excitation coils, and \mathbf{J} is the current density equal to \mathbf{J}_0 in air, but contains the effect of the eddy currents \mathbf{J}_e in the conducting material. Symbol μ is the permeability and σ is the conductivity of the magnetic material, \cdot denotes the time derivative.

The boundary conditions of the eddy current field problem can be given as follows. At the artificial far boundaries of the nonconducting region (air) Γ_n , homogeneous boundary conditions are assumed, i.e. the tangential component of the magnetic field intensity or the normal component of the magnetic flux density is zero, $\mathbf{H} \times \mathbf{n} = \mathbf{0}$ or $\mathbf{B} \cdot \mathbf{n} = 0$, where \mathbf{n} is the outer normal unit vector of the region. Homogeneous boundary conditions can be supposed along the symmetry planes (a part of Γ_n and Γ_c): $\mathbf{H} \times \mathbf{n} = \mathbf{0}$, i.e. $\mathbf{J} \cdot \mathbf{n} = 0$ and $\mathbf{E} \times \mathbf{n} = \mathbf{0}$. On the interface between the conducting (yoke) and nonconducting (air) regions Γ_{nc} , the interface conditions must be satisfied: $\mathbf{H} \times \mathbf{n}$ and $\mathbf{B} \cdot \mathbf{n}$ must be continuous and $\mathbf{J} \cdot \mathbf{n} = 0$.

Starting from $\nabla \cdot \mathbf{J} = 0$, the current density \mathbf{J} can be described by two current vector potentials [6, 21]: one is the known current vector potential \mathbf{T}_0 , corresponding to the exciting current, the other is the unknown current vector potential \mathbf{T} , defined only in the conducting material, Ω_c , taking into account the effect of the eddy currents, i.e.

$$\mathbf{J} \equiv \mathbf{J}_0 + \mathbf{J}_e = \nabla \times \mathbf{T}_0 + \nabla \times \mathbf{T}, \quad (4.19)$$

that is $\mathbf{J}_0 = \nabla \times \mathbf{T}_0$ and $\mathbf{J}_e = \nabla \times \mathbf{T}$. The magnetic field intensity \mathbf{H} can be approximated by the magnetic scalar potential Ψ and by the current vector potentials \mathbf{T} and \mathbf{T}_0 by substituting equation (4.19) into (4.14), i.e.

$$\mathbf{H} = \begin{cases} \mathbf{T}_0 - \nabla \Psi, & \text{in air containing the coil,} \\ \mathbf{T}_0 + \mathbf{T} - \nabla \Psi, & \text{in conducting material.} \end{cases} \quad (4.20)$$

The problem can be divided into two parts: there is a time varying magnetic field problem in air, and an eddy current field problem in the conducting material. The two parts must be coupled. This is the so called $\mathbf{T}, \Psi - \Psi$ potential formulation.

Substituting (4.19) into the relation (4.18) and using the characteristic (4.17) and the second definition in (4.20), Maxwell's equation (4.15) can be formulated by the partial differential equation

$$\nabla \times \frac{1}{\sigma} \nabla \times \mathbf{T} + \mu \dot{\mathbf{T}} - \mu \nabla \dot{\Psi} = -\nabla \times \frac{1}{\sigma} \nabla \times \mathbf{T}_0 - \mu \dot{\mathbf{T}}_0. \quad (4.21)$$

The Maxwell's equation (4.16) can be rewritten in the form

$$\nabla \cdot \{ \mu \mathbf{T}_0 + \mu \mathbf{T} - \mu \nabla \Psi \} = 0. \quad (4.22)$$

The partial differential equations to be solved in this case are the equation (4.8) in air (but $\mu = \mu_0$), moreover the equations (4.21) and (4.22) in the conducting material. These equations are coupled through the interface conditions between the air and the conducting material.

According to the method of weighted residuals, the partial differential equation (4.21) can be multiplied by the vector weighting function \mathbf{W}_j and integrated over the region Ω , i.e.

$$\begin{aligned} & \int_{\Omega} \mathbf{W}_j \cdot \nabla \times \frac{1}{\sigma} \nabla \times \mathbf{T} \, d\Omega + \int_{\Omega} \mu \mathbf{W}_j \cdot \dot{\mathbf{T}} \, d\Omega - \int_{\Omega} \mu \mathbf{W}_j \cdot \nabla \dot{\Psi} \, d\Omega \\ &= - \int_{\Omega} \mathbf{W}_j \cdot \nabla \times \frac{1}{\sigma} \nabla \times \mathbf{T}_0 \, d\Omega - \int_{\Omega} \mu \mathbf{W}_j \cdot \dot{\mathbf{T}}_0 \, d\Omega. \end{aligned} \quad (4.23)$$

Applying the mathematical identity $\nabla \cdot (\mathbf{u} \times \mathbf{v}) = \mathbf{v} \cdot \nabla \times \mathbf{u} - \mathbf{u} \cdot \nabla \times \mathbf{v}$, and substituting $\mathbf{u} = \mathbf{W}_j$ and $\mathbf{v} = \frac{1}{\sigma} \nabla \times \mathbf{T}$, and using the Gauss law, the following equation can be obtained:

$$\begin{aligned} & \int_{\Omega} \frac{1}{\sigma} \nabla \times \mathbf{W}_j \cdot \nabla \times \mathbf{T} \, d\Omega - \oint_{\Gamma} \mathbf{W}_j \times \left(\frac{1}{\sigma} \nabla \times \mathbf{T} \right) \cdot \mathbf{n} \, d\Gamma \\ &+ \int_{\Omega} \mu \mathbf{W}_j \cdot \dot{\mathbf{T}} \, d\Omega - \int_{\Omega} \mu \mathbf{W}_j \cdot \nabla \dot{\Psi} \, d\Omega \\ &= - \int_{\Omega} \frac{1}{\sigma} \nabla \times \mathbf{W}_j \cdot \nabla \times \mathbf{T}_0 \, d\Omega + \oint_{\Gamma} \mathbf{W}_j \times \left(\frac{1}{\sigma} \nabla \times \mathbf{T}_0 \right) \cdot \mathbf{n} \, d\Gamma \\ &- \int_{\Omega} \mu \mathbf{W}_j \cdot \dot{\mathbf{T}}_0 \, d\Omega. \end{aligned} \quad (4.24)$$

The boundary integral terms can be neglected, because $\mathbf{E} \times \mathbf{n} = \mathbf{0}$ at the boundary of the conducting material Γ_c , i.e.

$$\begin{aligned} & \int_{\Omega} \frac{1}{\sigma} \nabla \times \mathbf{W}_j \cdot \nabla \times \mathbf{T} \, d\Omega + \int_{\Omega} \mu \mathbf{W}_j \cdot \dot{\mathbf{T}} \, d\Omega - \int_{\Omega} \mu \mathbf{W}_j \cdot \nabla \dot{\Psi} \, d\Omega \\ &= - \int_{\Omega} \frac{1}{\sigma} \nabla \times \mathbf{W}_j \cdot \nabla \times \mathbf{T}_0 \, d\Omega - \int_{\Omega} \mu \mathbf{W}_j \cdot \dot{\mathbf{T}}_0 \, d\Omega. \end{aligned} \quad (4.25)$$

The approximating functions can also be introduced as the weighted sum of the potential values in nodes and along edges, i.e.

$$\Psi \simeq \sum_{i=1}^I N_i \Psi_i, \quad \mathbf{T}_0 \simeq \sum_{k=1}^K \mathbf{W}_k T_{0,k}, \quad \mathbf{T} \simeq \sum_{k=1}^K \mathbf{W}_k T_k. \quad (4.26)$$

The number of degrees of freedom is $I + K = 6$ using triangular finite elements.

The time derivatives of the variables have been approximated by the Euler backward algorithm, $\dot{\mathbf{T}} \simeq \frac{\mathbf{T}^{(n+1)} - \mathbf{T}^{(n)}}{\Delta t_n}$ at a given discrete time of the simulation t_n . Using this formula and substituting equations in (4.26) into (4.25), then the following system of

equations can be obtained in one finite element placed in the conducting material:

$$\begin{aligned}
& \sum_{k=1}^K \left\{ \frac{1}{\sigma} \int_{\Omega_e} \nabla \times \mathbf{W}_j \cdot \nabla \times \mathbf{W}_k \, d\Omega + \frac{\mu}{\Delta t} \int_{\Omega_e} \mathbf{W}_j \cdot \mathbf{W}_k \, d\Omega \right\} T_k^{(n+1)} \\
& - \sum_{i=1}^I \left\{ \frac{\mu}{\Delta t} \int_{\Omega_e} \mathbf{W}_j \cdot \nabla N_i \, d\Omega \right\} \Psi_i^{(n+1)} \\
& = \sum_{k=1}^K \left\{ \frac{\mu}{\Delta t} \int_{\Omega_e} \mathbf{W}_j \cdot \mathbf{W}_k \, d\Omega \right\} T_k^{(n)} - \sum_{i=1}^I \left\{ \frac{\mu}{\Delta t} \int_{\Omega_e} \mathbf{W}_j \cdot \nabla N_i \, d\Omega \right\} \Psi_i^{(n)} \\
& - \sum_{k=1}^K \left\{ \frac{1}{\sigma} \int_{\Omega_e} \nabla \times \mathbf{W}_j \cdot \nabla \times \mathbf{W}_k \, d\Omega \right\} T_{0,k}^{(n+1)} \\
& - \sum_{k=1}^K \left\{ \frac{\mu}{\Delta t} \int_{\Omega_e} \mathbf{W}_j \cdot \mathbf{W}_k \, d\Omega \right\} \left\{ T_{0,k}^{(n+1)} - T_{0,k}^{(n)} \right\}.
\end{aligned} \tag{4.27}$$

The partial differential equation (4.22), similarly as in the time varying magnetic field problem, can be weighted by the scalar weighting function N_j and must be integrated over the region Ω , i.e.

$$\int_{\Omega} N_j \nabla \cdot \{ \mu \mathbf{T}_0 + \mu \mathbf{T} - \mu \nabla \Psi \} \, d\Omega = 0. \tag{4.28}$$

Applying similar mathematical formulations as in the time varying magnetic field problem, the following system of linear equations can be obtained in one finite element:

$$\begin{aligned}
& - \sum_{k=1}^K \left\{ \mu \int_{\Omega_e} \nabla N_j \cdot \mathbf{W}_k \, d\Omega \right\} T_k^{(n+1)} + \sum_{i=1}^I \left\{ \mu \int_{\Omega_e} \nabla N_j \cdot \nabla N_i \, d\Omega \right\} \Psi_i^{(n+1)} \\
& = \sum_{k=1}^K \left\{ \mu \int_{\Omega_e} \nabla N_j \cdot \mathbf{W}_k \, d\Omega \right\} T_{0,k}^{(n+1)}.
\end{aligned} \tag{4.29}$$

The boundary conditions are the following: the magnetic scalar potential along the boundary and the symmetry plane as well as the tangential component of the unknown current vector potential along the symmetry plane and along the interface between the conducting and the nonconducting material are set to be zero.

Unfortunately, the system of linear equations generated by the edge elements of the FEM is singular which can only be solved by iterative solvers. I used the stabilized biconjugate gradient method (`bicgstab`, implemented in MATLAB [26, 99]). This iteratively finds an accurate solution of the system of equations starting from an initial guess. The solution is depending on the starting vector. The stopping criterion is based on the error

$$\varepsilon = \frac{\|\mathbf{b} - \mathbf{K}\mathbf{x}\|}{\|\mathbf{b}\|} \tag{4.30}$$

to reach $\varepsilon < 10^{-12}$, and \mathbf{K} is the system matrix, \mathbf{b} is the right hand side of the assembled equations and \mathbf{x} contains the unknown potentials. The initial guess of the iteration at a time instant is the stable solution of the previous time instant.

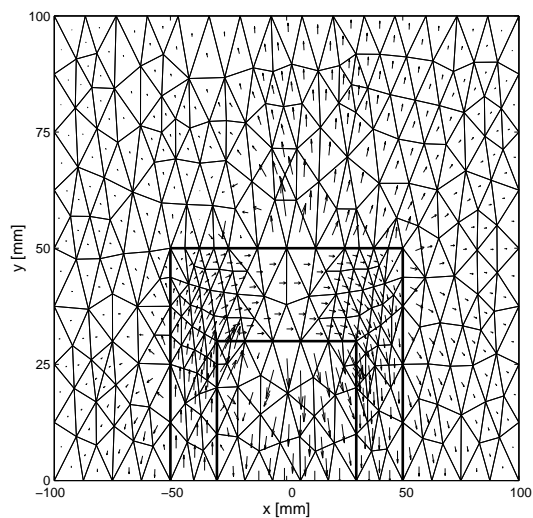
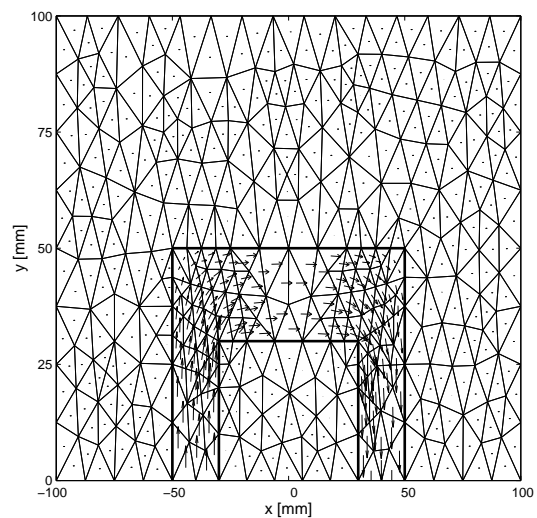
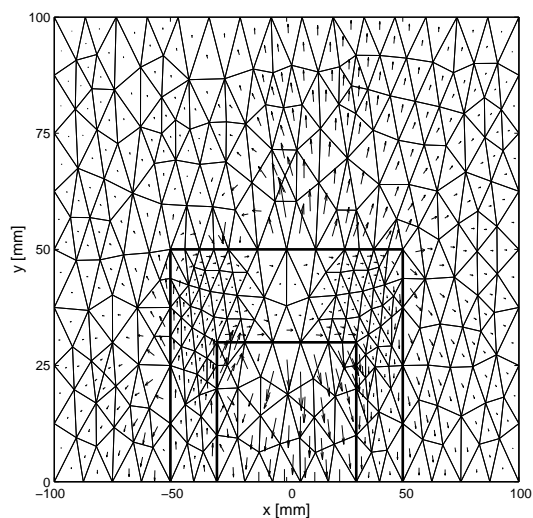
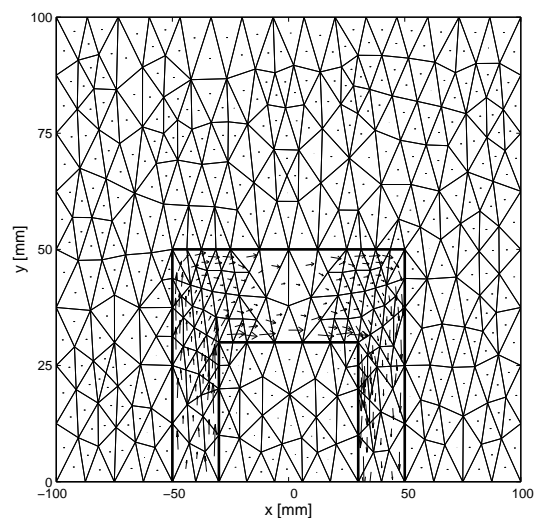
(a) The magnetic field intensity, \mathbf{H} (b) The magnetic flux density, \mathbf{B}

Fig. 4.5. Results of the time varying magnetic field simulations

(a) The magnetic field intensity, \mathbf{H} (b) The magnetic flux density, \mathbf{B} Fig. 4.6. Results of the eddy current field simulations, $f = 2$ Hz

The solution of the resulting system of linear equations gives the unknown potentials \mathbf{T} and Ψ at the time instant t_{n+1} .

The test example has been studied with the following parameters: the eddy current field problem in linear media has been run for four periods to reach the stationary state, one period has been divided into 40 time steps and the peak value and the frequency of the exciting current have been 1 A and 2 Hz, respectively. The following figures compare the results of the time varying magnetic field problem and the results of the eddy current field problem. The vectors of the magnetic field intensity and of the magnetic flux density can be seen in Fig. 4.5(a) and Fig. 4.5(b), and in Fig. 4.6(a) and Fig. 4.6(b) for the time

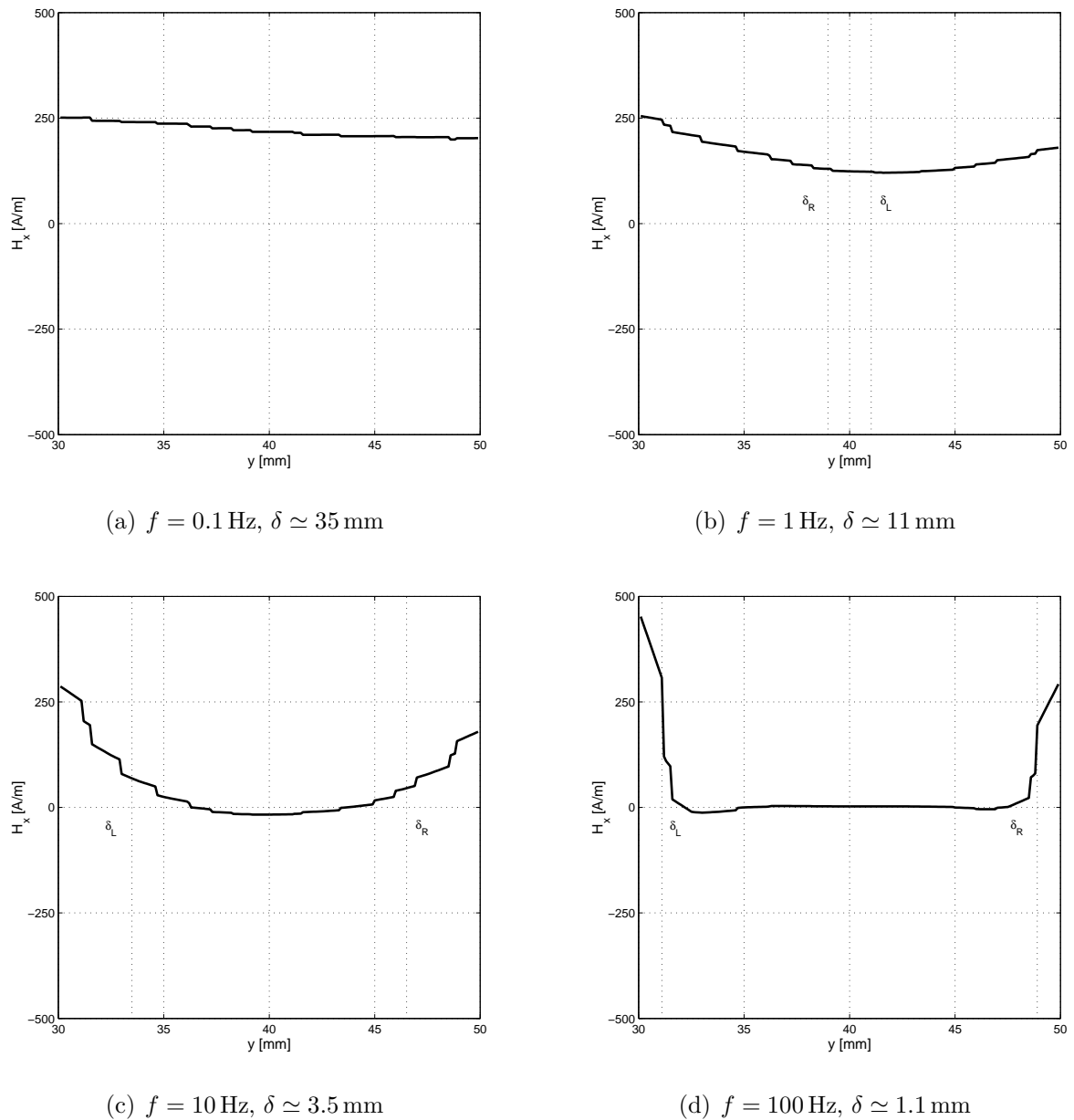


Fig. 4.7. The effect of extrusion of current v.s. increasing the frequency

varying case and for the eddy current case, respectively. The figures show the vectors at the time instant, when the current has a maximum value. The effect of the eddy currents is unambiguous in the pictures, let us compare the figures: the value of \mathbf{H} and of \mathbf{B} are smaller inside the magnetic material in the case of the eddy current field problem than in the case of the time varying magnetic field problem. This effect can be associated with the skin effect. The effect of frequency of the exciting current can be seen in Fig. 4.7(a)–4.7(d). These figures illustrate the x component of the magnetic field intensity H_x inside the yoke, along the line $x = 20 \text{ mm}$, and $y \in [30, \dots, 50] \text{ mm}$. The value of the skin depth has been calculated by $\delta = \delta_L = \delta_R = \sqrt{\frac{1}{\pi f \mu \sigma}}$. Applying linear shape functions results in staircase like functions as can be seen in the figures.

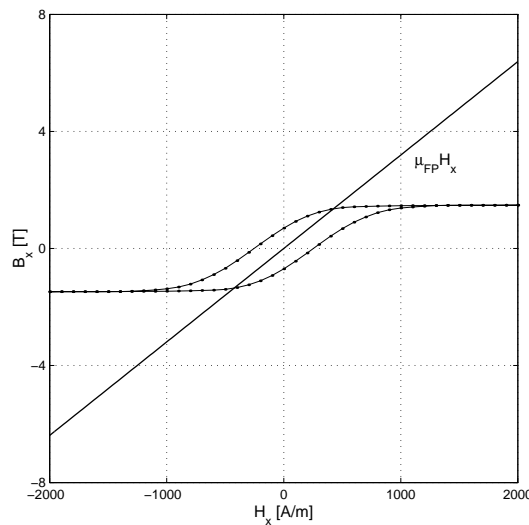


Fig. 4.8. The projected hysteresis characteristic in the x direction and the linear term $\mu_{FP}H_x$

4.1.3 The $\mathbf{T}, \Psi - \Psi$ formulation in hysteretic media

In this section, the time varying magnetic field and the eddy current field problems are explained taking into account the hysteretic relationship between the magnetic field intensity \mathbf{H} and the induction \mathbf{B} , i.e. $\mathbf{B} = \mathcal{H}\{\mathbf{H}\}$.

First, I present the partial differential equations and the weak form of the time varying magnetic field and of the eddy current field problems, then the simulation results are described.

The constitutive relation between the magnetic field intensity \mathbf{H} and the magnetization \mathbf{M} or the magnetic flux density \mathbf{B} can be linearized by the polarization method [11, 17, 24, 49, 58, 77]. The isotropic NN based $\mathbf{B} = \mathcal{H}\{\mathbf{H}\}$ relation is used,

$$\mathbf{B} = \mathcal{H}\{\mathbf{H}\} = \mu_{FP}\mathbf{H} + \mathbf{R}_{FP}, \quad (4.31)$$

where μ_{FP} is an ideal permeability, illustrated in Fig. 4.8 and selected by the relation

$$\mu_{FP} = \frac{\mu_{max} + \mu_{min}}{2}, \quad (4.32)$$

where μ_{max} and μ_{min} are the maximum and the minimum slope of the major hysteresis loop of the hysteresis characteristic, and \mathbf{R}_{FP} is the nonlinear residual term (in this example $\mu_{min} \simeq 0$). The value of μ_{FP} is constant during the calculations. The residual term \mathbf{R}_{FP} is derived iteratively during the nonlinear iteration scheme at every time step.

Time varying magnetic field problem in hysteretic media

Changing the linear constitutive relation $\mathbf{B} = \mu\mathbf{H}$ to the nonlinear, but linearized relation (4.31) and using the potential formulation (4.7) in the Maxwell's equation (4.2), the following partial differential equation can be obtained:

$$\nabla \cdot \{\mu_{FP}\mathbf{T}_0 - \mu_{FP}\nabla\Psi + \mathbf{R}_{FP}\} = 0. \quad (4.33)$$

This equation is valid in the magnetic material Ω_c . The partial differential equation in the air region Ω_n is (4.8), but $\mu = \mu_0$. The boundary conditions are the same as prescribed in section 4.1.1.

Applying the method of weighted residuals, the following system of equations for one finite element can be obtained in the nonlinear medium:

$$\begin{aligned} & \sum_{i=1}^I \left\{ \mu_{FP} \int_{\Omega_e} \nabla N_j \cdot \nabla N_i \, d\Omega \right\} \Psi_i \\ &= \sum_{k=1}^K \left\{ \mu_{FP} \int_{\Omega_e} \nabla N_j \cdot \mathbf{W}_k \, d\Omega \right\} T_{0,k} + \int_{\Omega_e} \nabla N_j \cdot \mathbf{R}_{FP} \, d\Omega. \end{aligned} \quad (4.34)$$

This system of equations is coupled with the weak form (4.13) with $\mu = \mu_0$.

Only one NN based hysteresis operator is defined in the barycenter of one finite element, therefore the nonlinear residual term \mathbf{R}_{FP} is supposed to be constant in a finite element.

Eddy current field problem in hysteretic media

Using the linearized constitutive relation (4.31) in nonlinear media, Ω_c , and the second potential formulation in (4.20) in the Maxwell's equations (4.15) and (4.16) with the relation (4.18) leads to the following partial differential equations:

$$\nabla \times \frac{1}{\sigma} \nabla \times \mathbf{T} + \mu_{FP} \dot{\mathbf{T}} - \mu_{FP} \nabla \dot{\Psi} = -\nabla \times \frac{1}{\sigma} \nabla \times \mathbf{T}_0 - \mu_{FP} \dot{\mathbf{T}}_0 - \dot{\mathbf{R}}_{FP}, \quad (4.35)$$

$$\nabla \cdot \{ \mu_{FP} \mathbf{T}_0 + \mu_{FP} \mathbf{T} - \mu_{FP} \nabla \Psi + \mathbf{R}_{FP} \} = 0. \quad (4.36)$$

The partial differential equation (4.8) valid in the air region Ω_n with $\mu = \mu_0$ must be coupled with the above partial differential equations (4.35) and (4.36) applying the same boundary conditions as prescribed in section 4.1.2.

After using the method of weighted residuals and the Euler backward algorithm, the following system of linear equations can be obtained for one finite element from the partial differential equations (4.35) and (4.36):

$$\begin{aligned} & \sum_{k=1}^K \left\{ \frac{1}{\sigma} \int_{\Omega_e} \nabla \times \mathbf{W}_j \cdot \nabla \times \mathbf{W}_k \, d\Omega + \frac{\mu_{FP}}{\Delta t} \int_{\Omega_e} \mathbf{W}_j \cdot \mathbf{W}_k \, d\Omega \right\} T_k^{(n+1)} \\ & - \sum_{i=1}^I \left\{ \frac{\mu_{FP}}{\Delta t} \int_{\Omega_e} \mathbf{W}_j \cdot \nabla N_i \, d\Omega \right\} \Psi_i^{(n+1)} \\ &= \sum_{k=1}^K \left\{ \frac{\mu_{FP}}{\Delta t} \int_{\Omega_e} \mathbf{W}_j \cdot \mathbf{W}_k \, d\Omega \right\} T_k^{(n)} - \sum_{i=1}^I \left\{ \frac{\mu_{FP}}{\Delta t} \int_{\Omega_e} \mathbf{W}_j \cdot \nabla N_i \, d\Omega \right\} \Psi_i^{(n)} \\ & - \sum_{k=1}^K \left\{ \frac{1}{\sigma} \int_{\Omega_e} \nabla \times \mathbf{W}_j \cdot \nabla \times \mathbf{W}_k \, d\Omega \right\} T_{0,k}^{(n+1)} \\ & - \sum_{k=1}^K \left\{ \frac{\mu_{FP}}{\Delta t} \int_{\Omega_e} \mathbf{W}_j \cdot \mathbf{W}_k \, d\Omega \right\} \{ T_{0,k}^{(n+1)} - T_{0,k}^{(n)} \} \\ & - \frac{1}{\Delta t} \int_{\Omega_e} \mathbf{W}_j \cdot \{ \mathbf{R}_{FP}^{(n)} - \mathbf{R}_{FP}^{(n-1)} \} \, d\Omega, \end{aligned} \quad (4.37)$$

and

$$\begin{aligned}
& - \sum_{k=1}^K \left\{ \mu_{FP} \int_{\Omega_e} \nabla N_j \cdot \mathbf{W}_k \, d\Omega \right\} T_k^{(n+1)} + \sum_{i=1}^I \left\{ \mu_{FP} \int_{\Omega_e} \nabla N_j \cdot \nabla N_i \, d\Omega \right\} \Psi_i^{(n+1)} \\
& = \sum_{k=1}^K \left\{ \mu_{FP} \int_{\Omega_e} \nabla N_j \cdot \mathbf{W}_k \, d\Omega \right\} T_{0,k}^{(n+1)} + \int_{\Omega_e} \nabla N_j \cdot \mathbf{R}_{FP}^{(n)} \, d\Omega.
\end{aligned} \tag{4.38}$$

The fixed–point iteration method

Handling the nonlinearity of the hysteresis characteristics can be worked out by the polarization method. An iterative solution of the governing system of linear equations leads to an approximate solution of the time varying magnetic field and of the eddy current field problems at the time instant t_n [11, 17, 24, 49, 58, 77].

The initial conditions (when $t_0 = 0$) are as follows: the magnetic field intensity, the magnetic flux density and the residual term are set to be zero in all finite elements, i.e. $\mathbf{H} = \mathbf{0}$, $\mathbf{B} = \mathbf{0}$, $\mathbf{R}_{FP} = \mathbf{0}$. This is the demagnetized state of the magnetic material.

During the fixed–point iteration, the time does not change, so for simplicity, superscript n does not label. The steps of the j^{th} fixed–point iteration step are illustrated in Fig. 4.9 and are the following:

1. Generating and solving the actual –above described– system of linear equations ($\mathbf{K}\mathbf{x}_j = \mathbf{b}_j$, where \mathbf{K} is the constant system matrix, \mathbf{b}_j is the right hand side of the assembled equations and the vector \mathbf{x}_j contains the unknown potentials, i.e. $\mathbf{x}_j = [\mathbf{T}_j \, \Psi_j]^T$) which gives the new iteration of the potentials Ψ_j and/or \mathbf{T}_j .
2. The actual value of the magnetic field intensity \mathbf{H}_j inside the magnetic material can be calculated by the equation (4.7) or by the second expression in (4.20) according to the time varying magnetic field or the eddy current field problem. The value of vector \mathbf{H}_j is calculated only in the barycenter of all finite elements.
3. An under relaxation method has been applied to speed up the convergence of the iteration,

$$\mathbf{H}_j \leftarrow (1 - \alpha)\mathbf{H}_{j-1} + \alpha\mathbf{H}_j,$$

where $\alpha = 0.5^j$. It generates an always convergent method [65].

4. The value of the magnetic flux density vector of all finite elements \mathbf{B}_j can be obtained by the NN based vector hysteresis operator according to the vector \mathbf{H}_j . These $\mathbf{H}_j - \mathbf{B}_j$ pairs are stored. Only one vector hysteresis operator has been applied in one finite element, and the residual term is supposed to be constant over it.
5. Updating the residual term $\mathbf{R}_{FP_{j+1}}$ in every finite element placed in the magnetic material,

$$\mathbf{R}_{FP_{j+1}} = \mathbf{B}_j - \mu_{FP}\mathbf{H}_j.$$

6. Convergence can be controlled by the norm

$$\varepsilon = \|\mathbf{H}_j - \mathbf{H}_{j-1}\|.$$

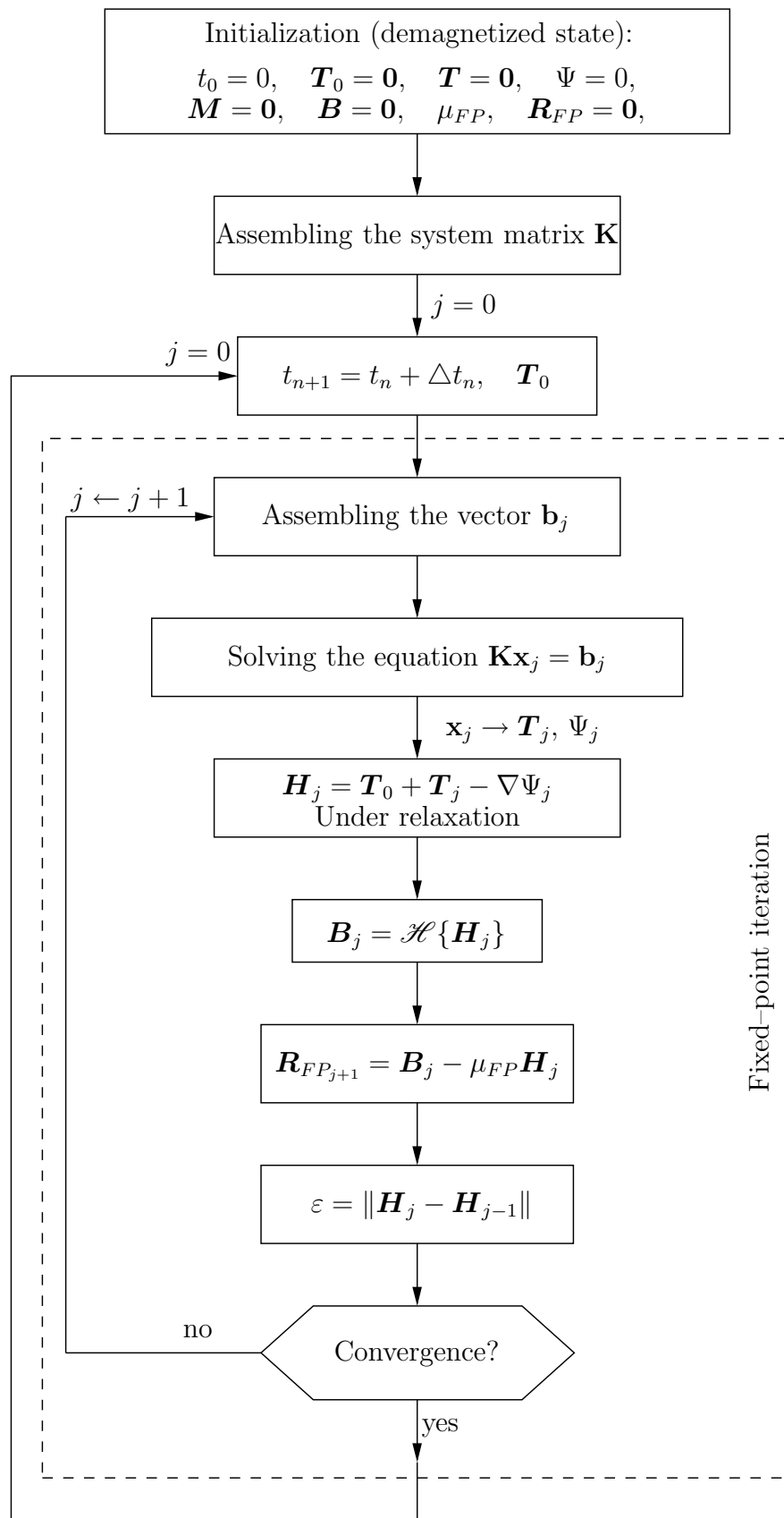


Fig. 4.9. Block diagram of the fixed-point iteration scheme

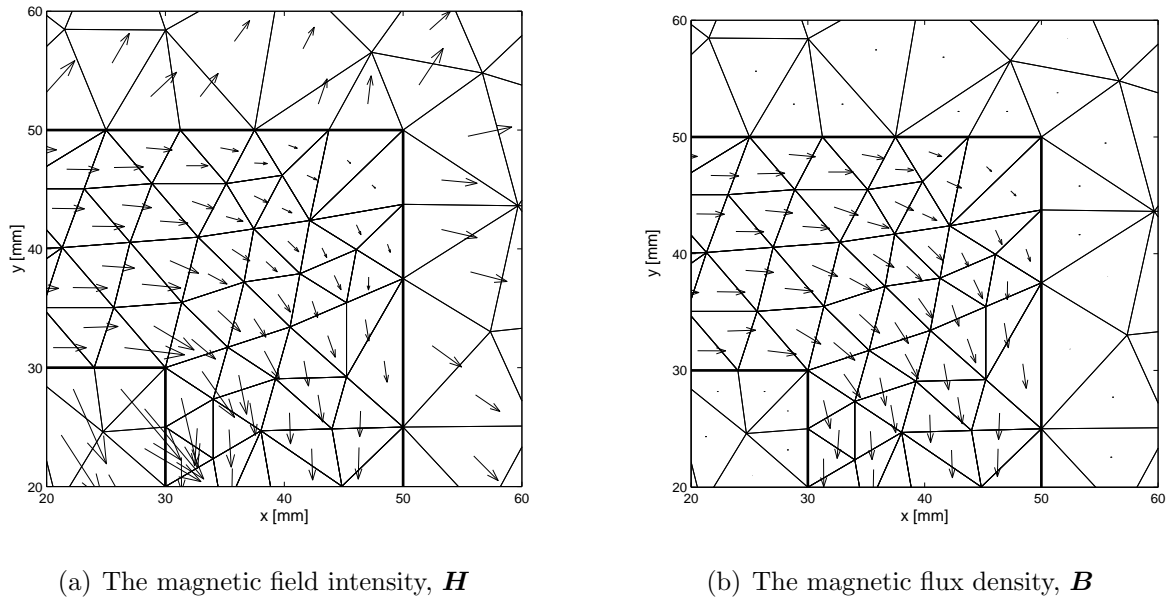


Fig. 4.10. Results of the nonlinear time varying magnetic field simulations

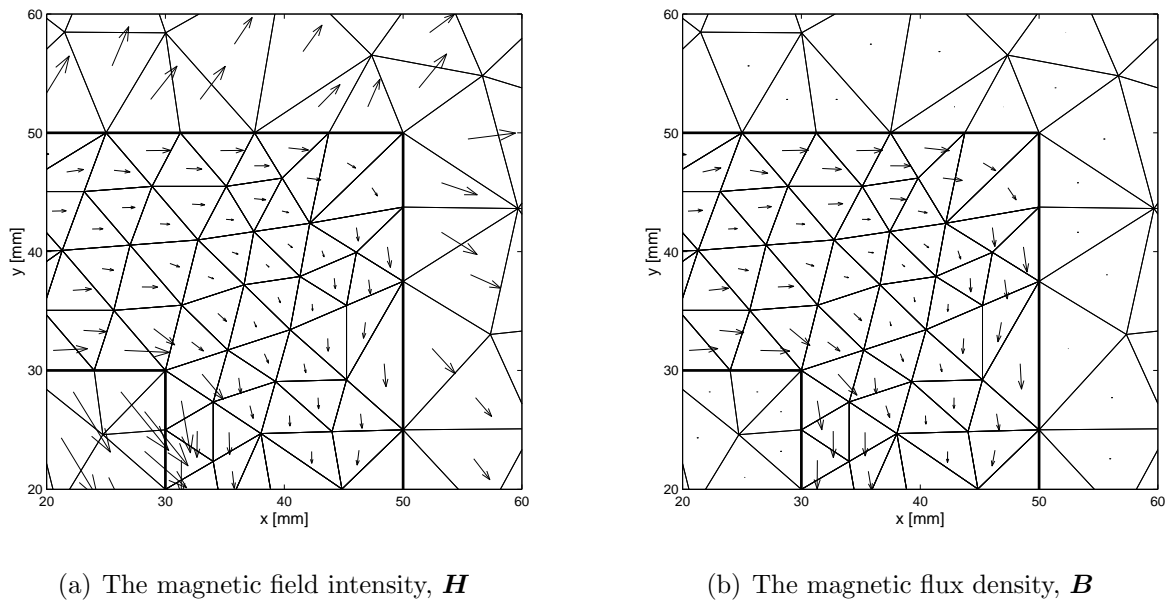
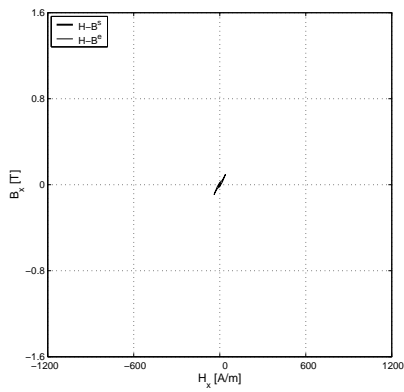


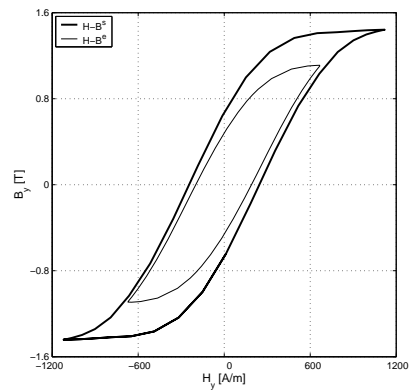
Fig. 4.11. Results of the nonlinear eddy current field simulations, $f = 1$ Hz

If it is fulfilled in every finite element, then the iteration step is convergent (in my experiments $\varepsilon = 10^{-4}$ has been used after some trials). In this case, the new time instant can be applied ($t_{n+1} = t_n + \Delta t$, and $j = 0$), otherwise the iteration must be repeated from the 1st step ($j \leftarrow j + 1$). The new iteration step uses the new, updated residual term.

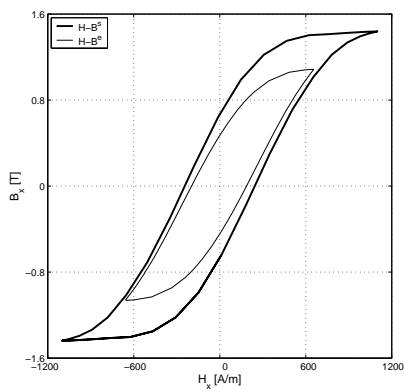
Iteration has no physical meaning, i.e. every iteration step must be started from the previous stable point on the hysteresis characteristic and $\mathbf{R}_{FP}^{(n-1)}$ does not change, but $\mathbf{R}_{FP}^{(n)} = \mathbf{R}_{FP}^{(j+1)}$.



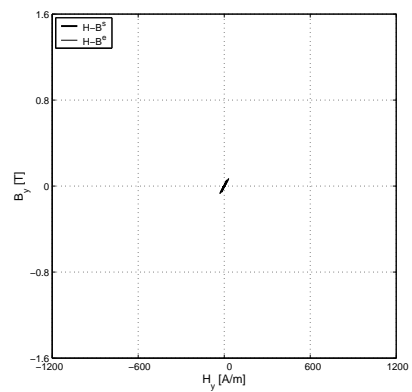
(a) Point 1, hysteresis curve $H_x - B_x$



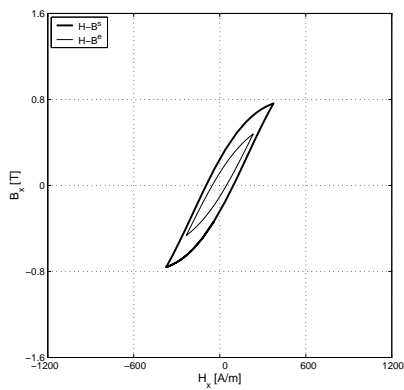
(b) Point 1, hysteresis curve $H_y - B_y$



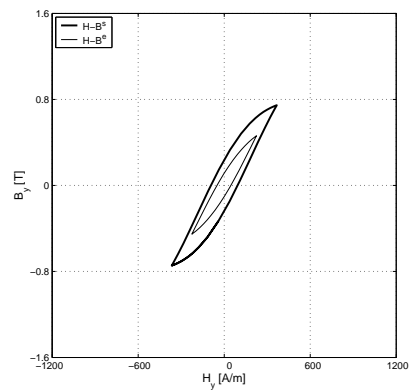
(c) Point 2, hysteresis curve $H_x - B_x$



(d) Point 2, hysteresis curve $H_y - B_y$



(e) Point 3, hysteresis curve $H_x - B_x$



(f) Point 3, hysteresis curve $H_y - B_y$

Fig. 4.12. Comparison of the projected hysteresis characteristics in the x and y directions obtained from the time varying magnetic field (s) and eddy current field (e) problems

The 2D nonlinear time varying magnetic field and the eddy current field problems have been applied to study the fixed–point technique in the FEM. The steady state of the eddy current field problem can be reached after the second period of the excitation, but four periods has been calculated. The magnetic field intensity and the magnetic flux density vectors are plotted in Fig. 4.10(a), Fig. 4.10(b) and in Fig. 4.11(a), Fig. 4.11(b) at the steady state when the exciting current has a maximum value ($\hat{I} = 5 \text{ A}$). The effect of eddy currents inside the magnetic material is unambiguous in the figures: the magnetic field intensity and the magnetic flux density inside the magnetic material are smaller in the case of the eddy current field problem than in the case of the time varying magnetic field problem. The figures show only the corner of the magnetic yoke.

I have worked out an other comparison between the time varying magnetic field and the eddy current field problems: the projected hysteresis characteristics in the x and in the y directions resulting by the orthogonal components of the magnetic field intensity and of the magnetic flux density have been analyzed. Three points have been selected; *Point 1* is at the vertical left leg of the yoke, where the magnetic field intensity has only vertical, y directed component, *Point 2* is at the center of the horizontal part, where the magnetic field intensity has only horizontal, x directed component and *Point 3* is at the corner. Results are plotted in Fig. 4.12(a)–4.12(f). The result of skin effect can be seen easily in the figures: the amplitude of the magnetic field intensity is smaller when eddy currents are taken into account than in the time varying magnetic field problem. Hysteresis characteristics projected in the x and in the y directions are plotted at the steady state. In the case of eddy current field problem, the hysteresis curves are smaller, since the magnetic field intensity is smaller according to the skin effect.

4.2 Summary

This 2D example shows the applicability of the $\mathbf{T}, \Psi - \Psi$ potential formulation with taking into account the hysteresis characteristic of the magnetic material in the frame of the FEM using nodal and edge shape functions.

The same formulations can be used to solve the nonlinear 3D simulation of the measuring test equipment introduced in the next chapter.

4.3 New scientific results

2. Thesis I have implemented the developed neural network based vector hysteresis model to the finite element method. I have applied the Ψ and the $\mathbf{T}, \Psi - \Psi$ potential formulations, because these directly give the magnetic field intensity vector which is the input variable of the direct vector hysteresis model. I have used the nodal and the edge shape functions for the approximation of the potentials. I have handled the neural network based vector hysteresis model by applying the B –scheme of the polarization method, and I have solved the linearized system of equations by the fixed–point iteration technique. I have used an under–relaxation scheme to speed up the convergence of the method. This results in a convergent and a well applicable method to solve both time varying magnetic field problem and eddy current field problem.

Chapter 5

Simulation of the built NDT measurement system

I have manufactured a nondestructive testing equipment in our Magnetic Laboratory. My aim was not to work out a new measurement system, but to allow the checking of the finite element based software presented in the previous chapter. The description of the measurement set-up with measured crack signals can be found in this chapter. Comparisons between the results of the 3D simulations and the measurements are presented at the end of this chapter.

5.1 Description of the measurement system

A photo of the installed NDT arrangement can be seen in Fig. 5.1.

The U-shaped yoke can be magnetized by the excitation coils (number of turns is $N = 129$). A specimen with well defined artificial surface cracks can be inserted among the legs of the yoke. In my experiments, I have applied the FluxSet sensor and the Hall-type sensor to measure the leakage magnetic field above the tested specimen. The applied sensor has measured the three orthogonal components of the magnetic field. The yoke and the specimen are made of the same magnetic material with the thickness of 5 mm (the size of the whole arrangement is $320 \times 240 \times 5$ mm). In this case, the specimen is magnetized by a longitudinal magnetic flux.

I have experienced the well known and obvious measurement result, i.e. increasing the distance between the surface of the specimen and the sensor (it is the so called lift-off) results in decreasing measured signal. I put the sensors as close to the surface as possible.

The schematic view of the built measurement set-up can be seen in Fig. 5.2 and described here.

The measuring arrangement contains a positioning device controlled by a Pulse Width Modulation signal ($f_{PWM} = 10$ kHz). The duty cycle of the PWM signal controls the position of the applied sensor above the tested specimen on the $x - y$ plane. The measurement of the x , the y and the z components of the magnetic field intensity vector can be picked out by using a 3D sensor which contains 3 orthogonal sensors with appropriate electronics. All tasks have been handled by the software package LabVIEW on a user-friendly graphical user interface [38] developed by me.

The excitation signal represented by its discrete set has been generated by a software

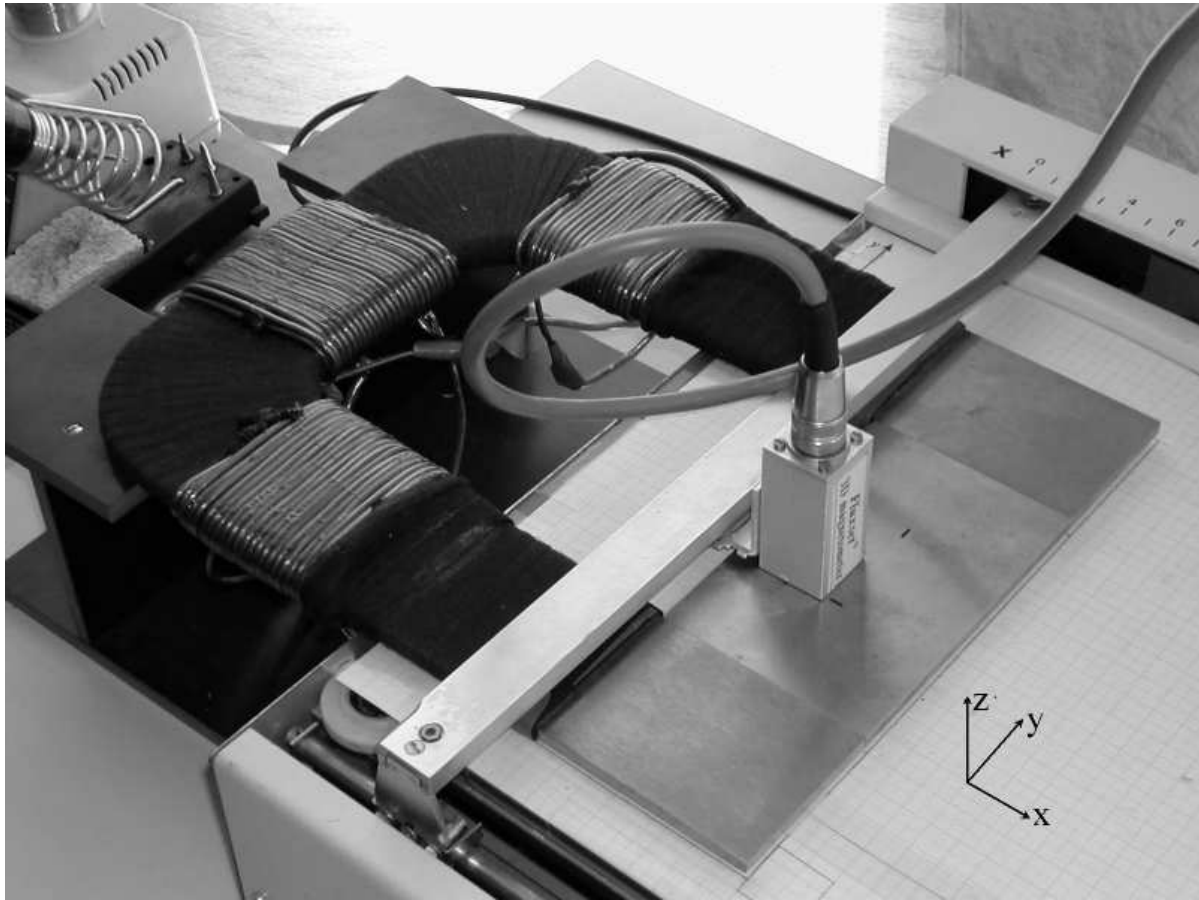


Fig. 5.1. The installed measuring arrangement

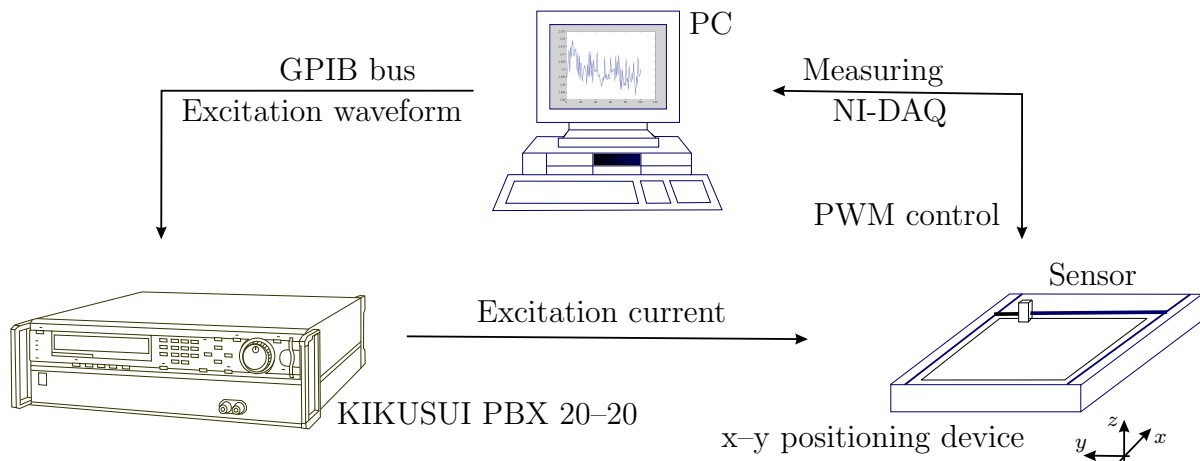


Fig. 5.2. The schematic view of the measurement set-up

based on the Instrument Control Toolbox of MATLAB [99] and has been downloaded into the memory of the power supply KIKUSUI using the GPIB bus [22, 100] (remote-control in high speed fast sequence, in CC mode). KIKUSUI can follow this signal continuously. The current generation and the measurements can be separated by this method.

At the scanning points, measurements have been performed through the NI-DAQ card built in the PC [38]. The basis of the measurements is very similar which used in the scalar hysteresis measurement system. After measuring some points, the average

of the measured signal (in DC case), or the amplitude and the phase, or the effective value of the measured signal (in AC case with sinusoidal excitation) can be calculated. Acquired data are stored and saved to a file automatically during the scanning and measuring process.

First, in section 5.2, I present my measurements with the FluxSet sensor, then in section 5.3, I show the results applying the Hall-type sensor. I present calibration techniques both to calibrate the FluxSet and the Hall sensors via simple measuring arrangements. I conclude my experiments in section 5.4.

5.2 Applying the FluxSet sensor

The FluxSet sensor is a high sensitivity sensor which is suitable for measuring DC and middle AC frequency ($f \leq 100$ Hz) magnetic field. This device has a very good sensitivity, stability, linearity and frequency independence as presented in [33, 75, 97].

The sensing element of the probe is an amorphous alloy ribbon with high initial permeability and low saturation. The probe of the sensor is made of two solenoids wound on each other. The inner solenoid and the outer solenoid are called the driving and the pick-up coils, respectively. The length of the sensor is about 14 mm. The core has an elliptical shape to decrease the air gap between the core and the coils. This core is periodically saturated by a triangle-shaped magnetic field produced by the driving coil, and the signal of the pick-up coil is transformed into pulses. The edges of these pulses control the counting clock converting the magnetic field intensity measurements into precise time measurements. Without any external magnetic field, the time intervals between the pulses are equal, but if an external field is applied, then the time intervals will be no longer symmetrical [33, 75, 97].

The probe has a so called compensation input. This can be used to set the zero point of the sensor. The compensation has to be performed beforehand in all scanning points and has to be stored in a file. In this case, the value of the output voltage of the sensor without any excitation is equal to 2.5 V, because the range of the output voltage is $[0, \dots, 5]$ V. Unfortunately, it has to be performed at every scanning points, because of the magnetic field of the positioning device, the arrangement and other unknown noises. This compensation process has also been worked out by using LabVIEW functions [55, 59].

5.2.1 Preliminary measurements

First of all, I have analyzed the linearity and the frequency independence of the FluxSet sensor, and I have demonstrated them with comparisons between measurements and calculations based on a simple arrangement as presented here.

The homogeneous and inhomogeneous magnetic fields have been generated by a simple test arrangement. This consists of 5 straight and parallel wires with the diameter of 1.4 mm, and they can be connected on any kind of variations. The axis of the wires is parallel to the x coordinate of the frame of reference. DC or AC current can be supplied through the wires, then the generated magnetic field has been measured by the FluxSet sensor on a scanning line perpendicular to the wires (y direction). The current flowing in the wires has only x component, i.e. the magnetic field intensity has y and z components. The frame of reference can be seen in Fig. 5.1.

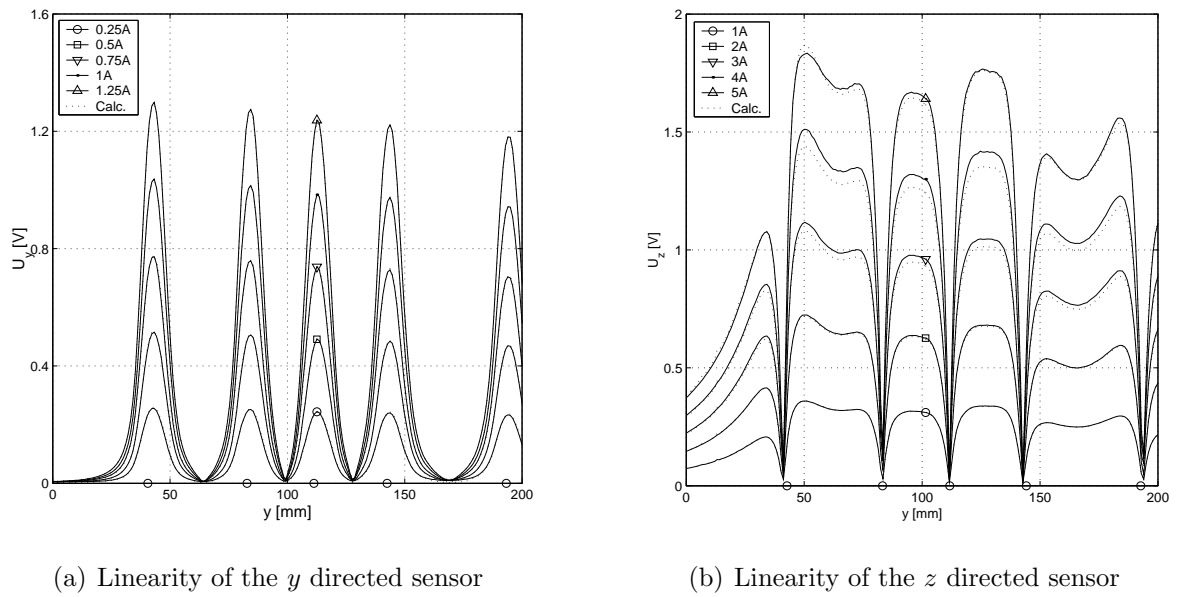


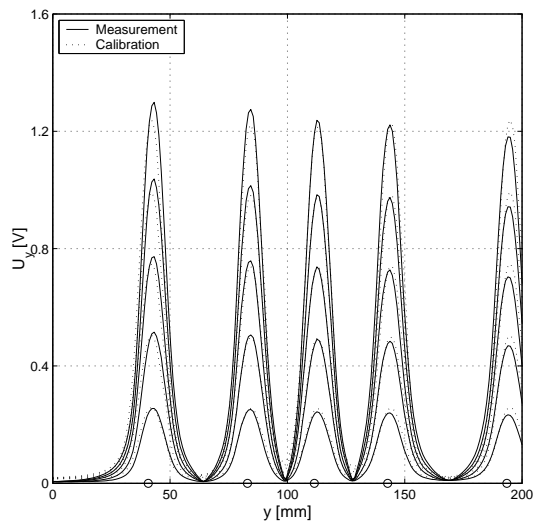
Fig. 5.3. Linearity of the two orthogonal sensors

The output voltage of the FluxSet sensor depends on the magnetic field intensity and this dependence is linear. I have checked this very important property, and the results of a test measurement can be seen in Fig. 5.3(a) and Fig. 5.3(b). The position of the wires is denoted by circles. It is obvious that, the y component of the magnetic field intensity has a maximum value, and the z component has zero value just above the wire. According to my measurements, the relative linearity error of the z directed sensor is maximum about 3 – 4%, however there is no difference between the measured and the calculated signals of the y directed sensor. In this case, the reference signal is the curve according to the current $\hat{I} = 1$ A, and the other curves have been determined by using these values multiplied by the value of the appropriate current. These measurements have been performed supplying a current with sinusoidal waveform ($f = 10$ Hz), then the effective value of the sensor output has been measured. My experiment is that, the z directed sensor is loaded by a higher noise than the y directed sensor. The lift-off (the distance between the sensor and the wire) of the y directed sensor is about 1.5 mm and the lift-off of the center point of the z directed sensor is about 8 mm. That is why the z directed sensor can measure magnetic field intensity generated by higher currents, and this may be the reason of the higher noise as well.

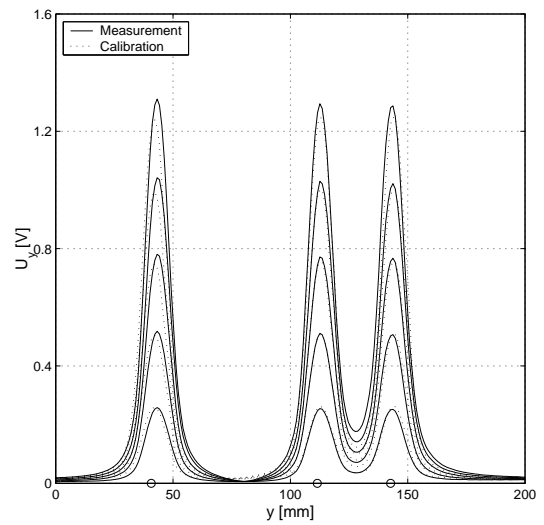
The output voltage is independent of the frequency of the excitation, if $f \leq 100$ Hz. This measurement has been performed on the same arrangement, and I have found that, the difference in the frequency range $f \in [0, \dots, 100]$ Hz is maximum about 5% relative to the DC measurements. Increasing the frequency results decreasing effective value, e.g. if $f = 160$ Hz, the relative difference is about 15%.

5.2.2 Calibration of the sensor

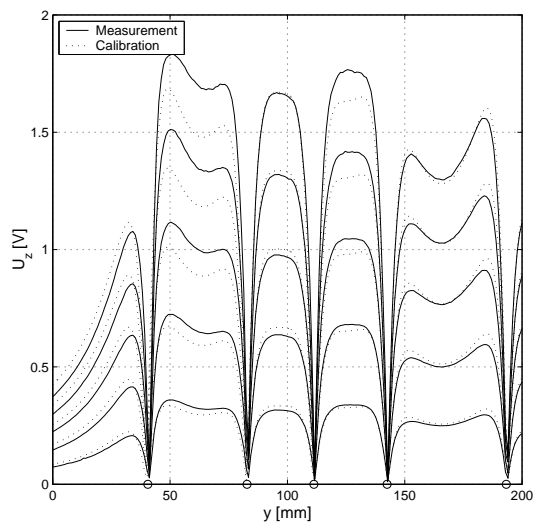
The magnetic field generated by the above system of wires is inhomogeneous. A model must be built to simulate the behavior of the sensor. This is the calibration of the FluxSet sensor.



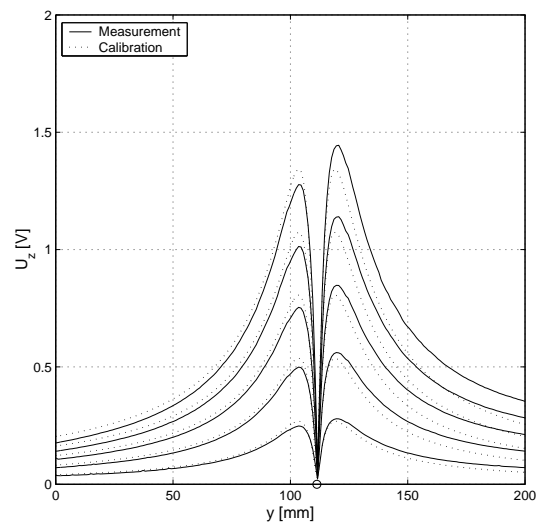
(a) The calibration set-up and comparison for the y directed sensor



(b) Comparison of signal of 3 wires, verification of the y directed sensor



(c) The calibration set-up and comparison for the z directed sensor



(d) Comparison of signal of 1 wire, verification of the z directed sensor

Fig. 5.4. Comparison between calculated and measured signals

For homogeneous fields, it is enough to measure and to calculate the magnetic field intensity along the axis of a Helmholtz-type core, then a calibrating factor can be calculated.

I have found that, the magnetic field intensity generated by the above measurement system can be calculated analytically as the superposition of magnetic field intensities of $H = I/(2r\pi)$. Here, I is the effective value of the current flowing in the wires, r is the distance between the wire and a point of the space where the effective value of the magnetic field intensity H is calculated. The vector components H_y and H_z of the magnetic field intensity can be obtained. The calculated signals can be fitted to the

measured ones using several calibration parameters.

The length of the sensor coil is about 14 mm, and it cannot be assumed that the sensor is a pointwise instrument. It is supposed that, the measured signal can be predicted by the weighted sum of the calculated magnetic field intensities obtained in the axis of the sensor, because the sensor is linear. The weighting coefficients are calculated by finding the best fit to the actually measured curves during the optimization process in the least square sense. The magnetic field is calculated in L locations along the sensor and in P sensor positions ($P > L$) [55, 59, 73]. According to this process the

$$\mathbf{A}\mathbf{w} = \mathbf{b} \quad (5.1)$$

system of linear equations can be generated, where \mathbf{A} is a $P \times L$ matrix storing the calculated magnetic field intensities, \mathbf{b} is a column vector containing the effective value of the measured voltages in P positions and \mathbf{w} is the unknown weighting vector. The optimal solution of (5.1) can be obtained as

$$\mathbf{w} = (\mathbf{A}^T \mathbf{A})^{-1} (\mathbf{A}^T \mathbf{b}), \quad (5.2)$$

because the number of equations is larger than the number of unknowns.

This calibration technique has been applied to approximate measured curves. The system of linear equations (5.1) has been built with $P = 201$ sensor positions, and $L = 9$ locations (y directed sensor) and $L = 3$ locations (z directed sensor). After some trials, this set-up has given the best results as plotted in Fig. 5.4(a) and in Fig. 5.4(c).

My experiment is that, the resulting weights can be used to simulate the sensors when measuring the magnetic field intensity generated by less wires or other configurations (see Fig. 5.4(b) and Fig. 5.4(d)) with the maximum relative error 10 – 15%. This is the verification of the calibration method.

It can be clearly seen in the figures that, the y directed sensor can be calibrated much better than the z directed sensor. The y directed sensor is closer to the measured wires (lift-off is about 1.5 mm), and the distance between the center point of the z directed sensor and the wires is about 8 mm. This important difference may be the reason of the worse calibration results. Moreover, the output voltage of the z directed sensor is not symmetrical at the simplest case (1 wire, Fig. 5.4(d)), however the calculation gives symmetrical output voltage, and this is a consequence of the arrangement. I think, the motor of the positioning device, or the whole mechanics disturb the measurements. A more precise positioning servo would be better, where the servo is far enough from the measuring arrangement, but this is a cheap equipment prepared from an old, redone $x - y$ plotter.

In the NDT measurements, I have used only the y directed sensor which is parallel to the surface of the specimen. My experiment is that, the output voltage of the y directed sensor gives the best and the most attractive results for this NDT arrangement.

5.2.3 The lock-in amplifier

I have used a lock-in amplifier implemented in LabVIEW for precise measurement of the AC signals [100]. The block diagram of the lock-in amplifier can be seen in Fig. 5.5. The reference signal with frequency ω_r (the signal of the excitation current) is fed into an internal reference synthesizer (PLL) that extracts the frequency and the phase

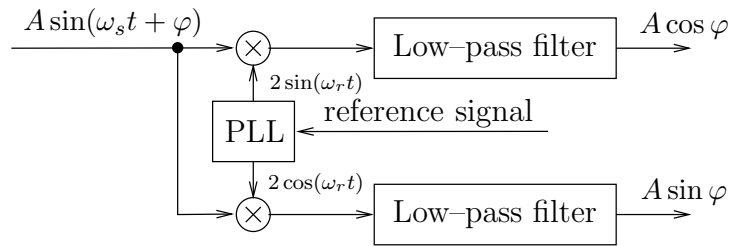


Fig. 5.5. Simplified lock-in block diagram

information from the reference signal and generates a pure sine wave. This signal is then mixed with the measured signal with frequency ω_s . It results two output components with the frequency equal to the difference and the sum of the internal reference signal and the measured one. For the component of the input signal with frequency equal to the internal reference signal ($\omega_s = \omega_r$), the first mixer component will be a DC signal and the second component will have frequency equal to twice of the reference frequency which can be rejected by a low-pass filter. The two outputs of the lock-in amplifier are the real and the imaginary parts of the measured signal referred to the reference signal. The amplitude A and the relative phase φ also can be determined.

5.2.4 NDT measurements

The winding has been excited by a sinusoidal signal ($\hat{I} = 0.5 \text{ A}$, $f = 1 \text{ Hz}$). My experiment was that, the amplitude of the exciting current must be small generating small magnetic field intensity inside the yoke, otherwise the sensor goes to saturation (the maximum value of the output voltage of the sensor is 2.5 V, above this value the sensor cannot measure variations). In this case, the maximum amplitude of the measured voltage was about 1.8 V.

The effect of hysteresis characteristic of the yoke and of the specimen could not sensed, because the magnetization is depending almost linearly on the applied magnetic field intensity, since the magnetic field intensity is small. By applying demagnetization, the demagnetized state ($H = 0$, $M = 0$, $B = 0$) almost can be reached. Demagnetization has been performed under a sinusoidal signal with decreasing amplitude at low frequency ($f = 0.1 \text{ Hz}$).

I have measured three types of artificial surface cracks scanning the same surface where the crack has been located. The scanning area was $30 \text{ mm} \times 30 \text{ mm}$ around the crack (crack was in the origin) and the measurements have been performed in 31×31 points by using the lock-in amplifier. According to my measurements, the phase of the measured signal was almost constant ($\varphi \simeq -4^\circ$), i.e. the real part was almost equal to the amplitude of the measured signal and the imaginary part was relatively small.

The detection of cracks has been based on a comparison with a crackless specimen (etalon). First of all, a specimen without any cracks has been analyzed, then the measured voltage according to the crackless specimen has been subtracted from the measured voltage belonging to the cracks. The edge effect according to the side of the arrangement also can be decreased.

The output voltage of the sensor had a maximum value just above the crack, because I have measured the y component of the leakage magnetic field.

In the first case, the effect of diameter of the surface hole has been measured and

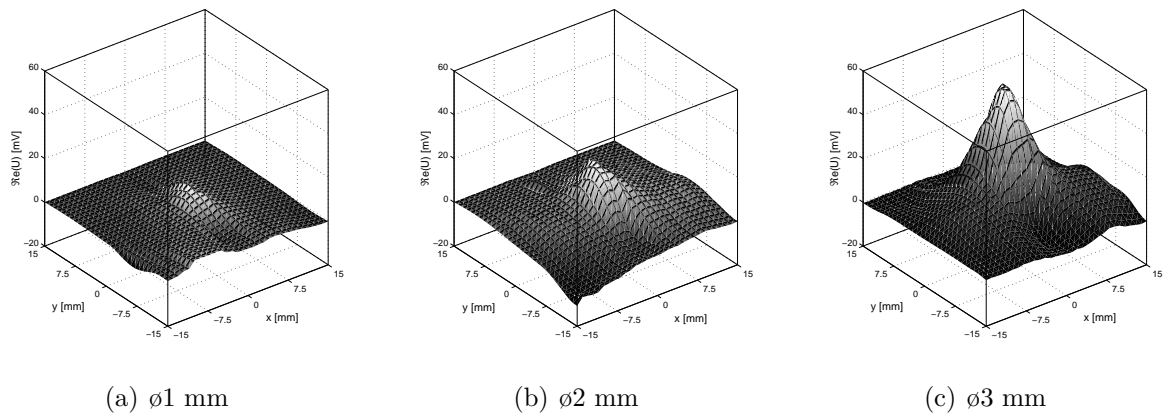


Fig. 5.6. Measurement results I, the effect of diameter of the crack

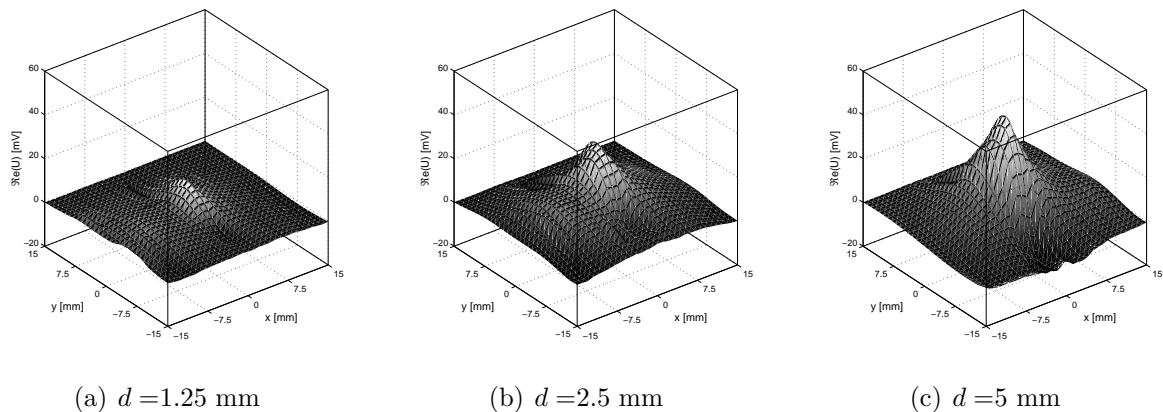


Fig. 5.7. Measurement results II, the effect of depth of the crack

the results are plotted in Fig. 5.6(a)–5.6(c). The diameter of the cracks is given in the figures, the depth of the cracks was 2.5 mm. Increasing the diameter results increasing value of the output voltage of the sensor.

In the second measurement set, the effect of depth of the hole has been analyzed and the diameter was 2 mm (see Fig. 5.7(a)–5.7(c)). A crack with a depth of 0.5 mm could not detect, but increasing the depth of crack results increasing output voltage of the sensor.

Finally, the orientation of the surface slots (see Fig. 5.8) has been detected. The first slot was perpendicular to the direction of the scanning lines, the second one was transversal to this. The contour plot of the surface of the measured voltage can be seen in Fig. 5.9(a) and 5.9(b). The size of the slots was 5 mm \times 1 mm, and the depth was 2.5 mm. The perpendicular slot could be detected easily, because the peak value of the measured sensor voltage was about 80 mV, but the maximum value of the measured voltage according to the transversal slot was just about 15 mV.

My experiment was that, similar results with smaller output voltage can be obtained when analyzing the same cracks, but scanning the opposite surface of the specimen. In this case, the output voltage was about the half of the above results.

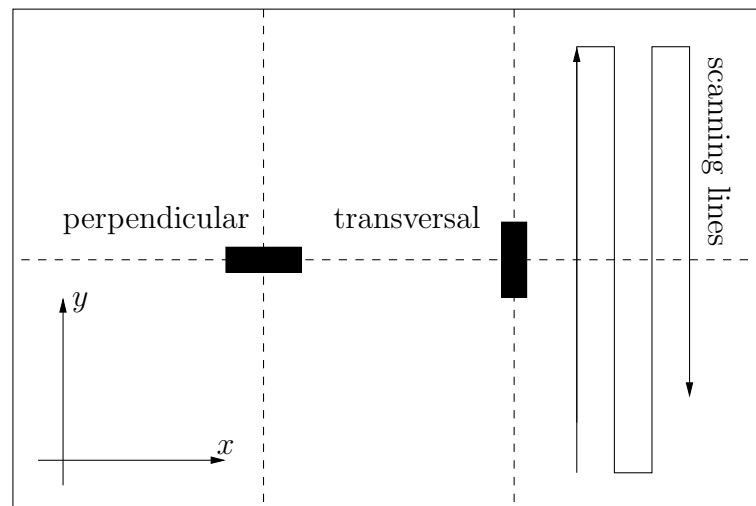
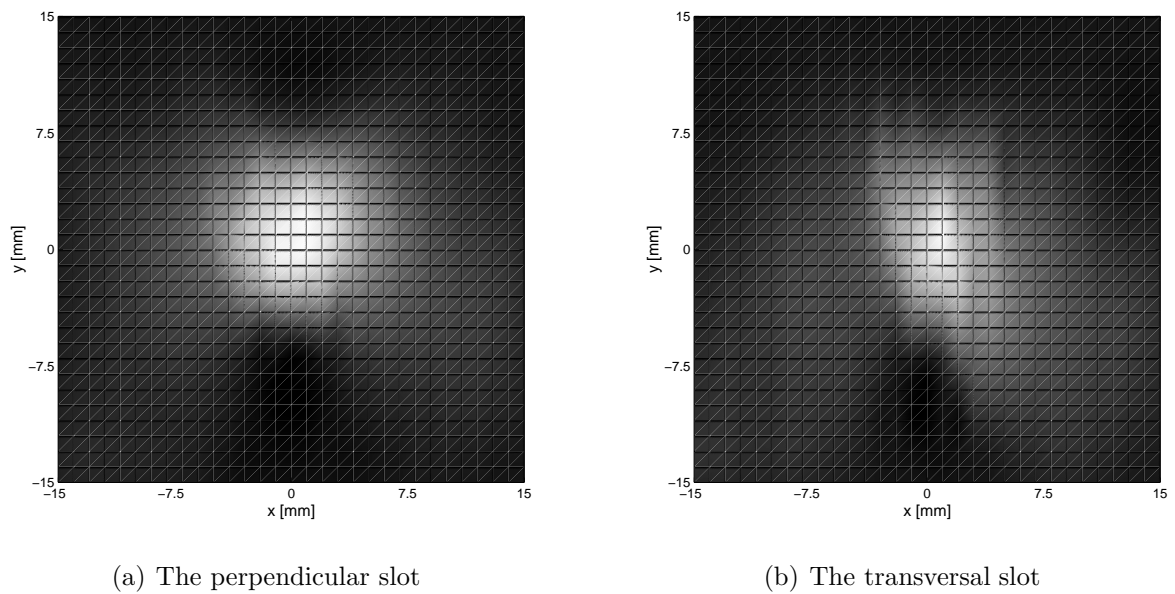


Fig. 5.8. The manufactured perpendicular and transversal slots



(a) The perpendicular slot

(b) The transversal slot

Fig. 5.9. Top view of the measured voltage

A 2D adaptive noise-removal filtering has been performed on measured signals by the Wiener filter implemented in the Image Processing Toolbox of MATLAB [99]. This lowpass filters the intensity image that has been degraded by additive noise and Wiener filtering causes a little smoothing as well.

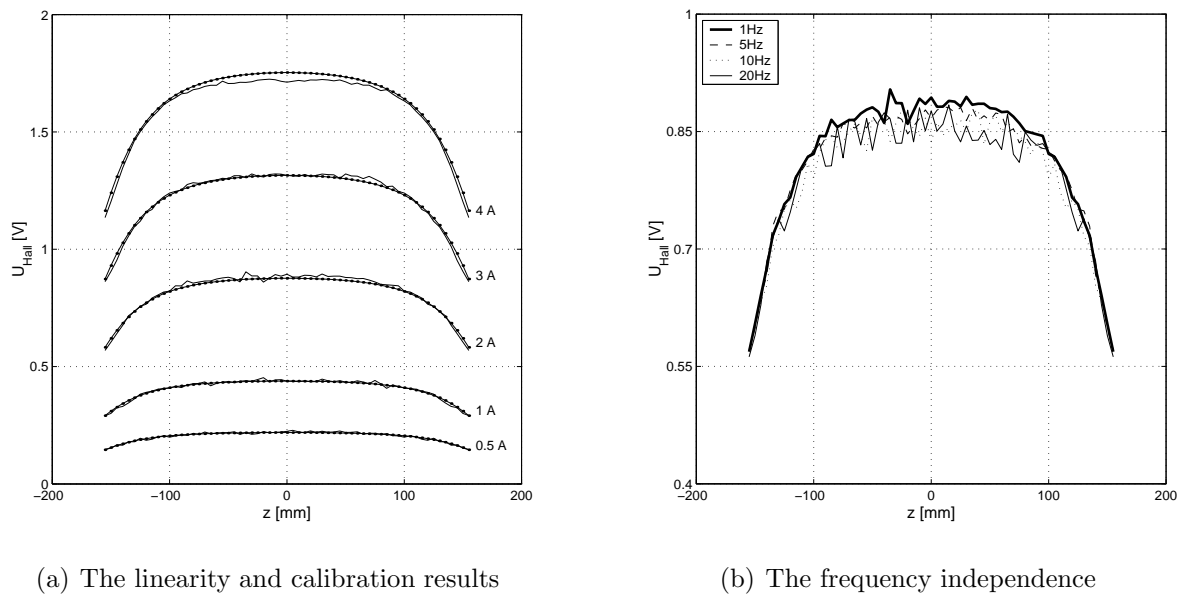


Fig. 5.10. Examination of the Hall-type sensor

5.3 Applying the Hall-type sensor

A 3D Hall-type sensor has been developed in the frame of a student work under my supervisorship [42]. The sensor is a GaAs sensor, and the type is OH10003. The prepared probe contains three orthogonal Hall sensors as close to each others as possible. The output signal of the Hall sensor is very small (in this case, it is in the range of $10 \dots 100 \mu\text{V}$), so it is amplified by an operational amplifier (to the range of $1 \dots 10 \text{ V}$). This is a simpler and cheaper instrument than the FluxSet sensor. The size of the applied Hall sensor is $2.9 \text{ mm} \times 1.5 \text{ mm} \times 1.1 \text{ mm}$, and it is much smaller than the length of the coil in the FluxSet sensor (14 mm).

Classically, the Hall effect in a semiconducting medium is based on the Lorentz force $\mathbf{F} = Q(\mathbf{v} \times \mathbf{B})$ when a particle with charge Q is moving with velocity \mathbf{v} within a magnetic field \mathbf{B} . If a long, flat current-carrying conductor is placed in a magnetic field, the moving charges will experience a force perpendicular to the direction of the current and of the magnetic field. It results an un-even charge distribution and gives rise to an electric field \mathbf{E} which generates a measurable Hall-voltage which is proportional to the magnetic flux density [69, 70].

5.3.1 Preliminary measurements and calibration

However the sensor has satisfactory linearity with respect to the magnetic field intensity and small temperature coefficient according to the catalogue of the sensor, we have analyzed the linearity and the frequency independence of the sensor and its electronics.

Test measurements have been performed by a calibrating coil which length was $l = 340 \text{ mm}$, the radius was about $r = 50 \text{ mm}$ and the number of turns was $N = 305$. The Hall sensor has been placed into the axis of the coil and the output voltage has been measured in the range of $z \in [-155, \dots, 155] \text{ mm}$, if $z = 0$ is the center point of the coil. The magnetic field intensity along the axis of the coil can be calculated easily by the

Biot–Savart law according to the relation [29]

$$H_z(z) = \frac{NI}{2l} \left\{ \frac{l/2 - z}{\sqrt{(l/2 - z)^2 + r^2}} + \frac{l/2 + z}{\sqrt{(l/2 + z)^2 + r^2}} \right\}. \quad (5.3)$$

According to the supposed linearity, the effective value of the output voltage is proportional to the effective value of the magnetic field intensity, i.e. $U_{Hall} = kH_z$, where k is a constant calculated from measurements. In this case $k = 5.095 \cdot 10^{-4} \text{ Vm/A}$, and it can be used as a calibrating factor.

The linearity and the calibration results can be seen in Fig. 5.10(a). The calculated output voltage is denoted by points, the measured signal is denoted by solid line. The calibration error is maximum 4% referred to the signal according to the current $\hat{I} = 1 \text{ A}$.

The frequency independence of the output voltage of the sensor has been analyzed in some given frequency ($1 \text{ Hz} < f < 20 \text{ Hz}$), and the frequency independence of the sensor is illustrated in Fig. 5.10(b) ($\hat{I} = 2 \text{ A}$).

In the NDT measurements, I used only the z directed sensor which is perpendicular to the surface of the specimen. The other two sensors are far away from the surface, however we tried to place them as close to the surface as possible. My experiment is that, the output voltage of the z directed sensor is the most effective for NDT measurements.

5.3.2 NDT measurements

The core has been excited by a sinusoidal signal ($\hat{I} = 8 \text{ A}$, $f = 1 \text{ Hz}$). In this case, the amplitude of the exciting current can be higher, because the saturation of the Hall sensor is higher than the saturation of the FluxSet sensor. The Hall sensor is able to measure higher magnetic field intensity, but it is more sensitive to noise.

The hysteresis characteristics can be sensed, i.e. the magnetization is depending on the hysteresis curve of the yoke. Before measurements, the yoke and the specimen have been demagnetized by a sinusoidal signal with decreasing amplitude.

I have performed some preliminary measurements along a scanning line through a crack to find the best excitation. I have set the amplitude ($\hat{I} = 2 \text{ A}, 4 \text{ A}, 6 \text{ A}, 8 \text{ A}, 10 \text{ A}$), and the frequency ($f = 0.1 \text{ Hz}, 0.5 \text{ Hz}, 1 \text{ Hz}, 5 \text{ Hz}, 10 \text{ Hz}$) of the exciting current to find the best one, since the amplitude and the frequency determine the hysteresis curve of the material. I have experimented that, increasing the amplitude results increasing amplitude of the measured crack signal, but increasing the frequency in the given range results no significant modifications. If the amplitude, and the frequency are chosen as $\hat{I} = 8 \text{ A}$ and $f = 1 \text{ Hz}$, respectively, I can obtain the best results. I tried to use small frequency, because the hysteresis model applied in the simulations is a frequency independent model.

The measured voltage is larger close to the leg of the yoke, and smaller close to the symmetry plane of the arrangement resulting a small rise in the measured signal as illustrated in Fig. 5.11. This rise can be eliminated by subtracting the crackless signal. The peaks in the signal of the z directed sensor denote the crack, but the other two sensors cannot detect the crack exactly. This subtraction results only the signal caused by the crack.

The LabVIEW user–friendly graphical user interface (GUI) can also be seen in Fig. 5.11. The measured components and the spectrum of the measured signals can be seen at the bottom of this window. The effective value of the measured signals is also plotted

and saved in a file. Important data can be set through the GUI: the coordinates of the scanning area, the number of steps above the specimen, the number of samples per periods and the number of periods to be measured.

The bridge, where the sensor is moving in the y direction is made of aluminum, but unfortunately, the mechanics of it disturbs the measured signal. I have prepared a spacer which enables to move the sensor far away from this mechanics. A comparison between the two measurements can be seen in Fig. 5.12, where the 1st measurement is performed without the spacer and the 2nd is with using the spacer. This figure shows the output voltage of the z directed sensor. Measurements are closer to the calculated results when the effect of mechanics has been eliminated. I have realized this problem after developing the FEM software and I have made the measurements again.

I have measured the same artificial surface cracks as analyzed by the FluxSet sensor. In this case, the scanning area was 40 mm×40 mm around the crack and the measurements are performed 41×41 points (the crack is in the origin). After measuring 5 periods, the effective value of the measured voltage has been calculated, then the crackless signal has been subtracted from it.

The output voltage of the sensor had zero value just above the crack and had maximum and minimum values before and after the crack, because I have measured applying the z directed sensor. These two peaks results much accurate contour plots than the one peak of the y component.

In the first case, the effect of diameter of the surface hole has been measured and the results are plotted in Fig. 5.13(a)–5.13(c). The diameter of the cracks is given in the figures, the depth of the cracks was 2.5 mm. Increasing the diameter results increasing value of the output voltage.

In the second measurement set, the effect of depth of the hole has been analyzed, when the diameter was 2 mm (see Fig. 5.14(a)–5.14(c)). A crack with a depth of 0.5 mm could be detected again, but increasing the depth of the crack results in increasing output voltage.

Finally, the orientation of the same surface slots has been detected (see Fig. 5.8). The first slot was perpendicular to the direction of the scanning line, the second one was transversal to this. The top view of the measured voltages can be seen in Fig. 5.15(a) and Fig. 5.15(b). The perpendicular slot could be detected easily, because the peak value of the measured voltage was about 0.15 V, and the maximum value of the measured voltage according to the transversal slot was just about 0.06 V, but the contour plot of the measurements show the orientation of the crack. The orientation and the size of the slots is deducible. Measuring the z component gives more accurate contour plots than measuring the y component.

5.4 Conclusions of the measurements

I have experimented that, the FluxSet sensor is more sensitive than the Hall-type sensor, i.e. the FluxSet sensor can measure small magnetic fields. The Hall sensor is able to measure much higher magnetic fields.

The Hall sensor has a very small size, but I think, a matrix with 3×3, or 5×5 sensors would give better and more accurate measurements. Of course, more sensitive type of sensor should be used. There exists a problem of the demagnetizing process: the power supply can generate a current with the maximum peak value of 20 A. It seems that, it is

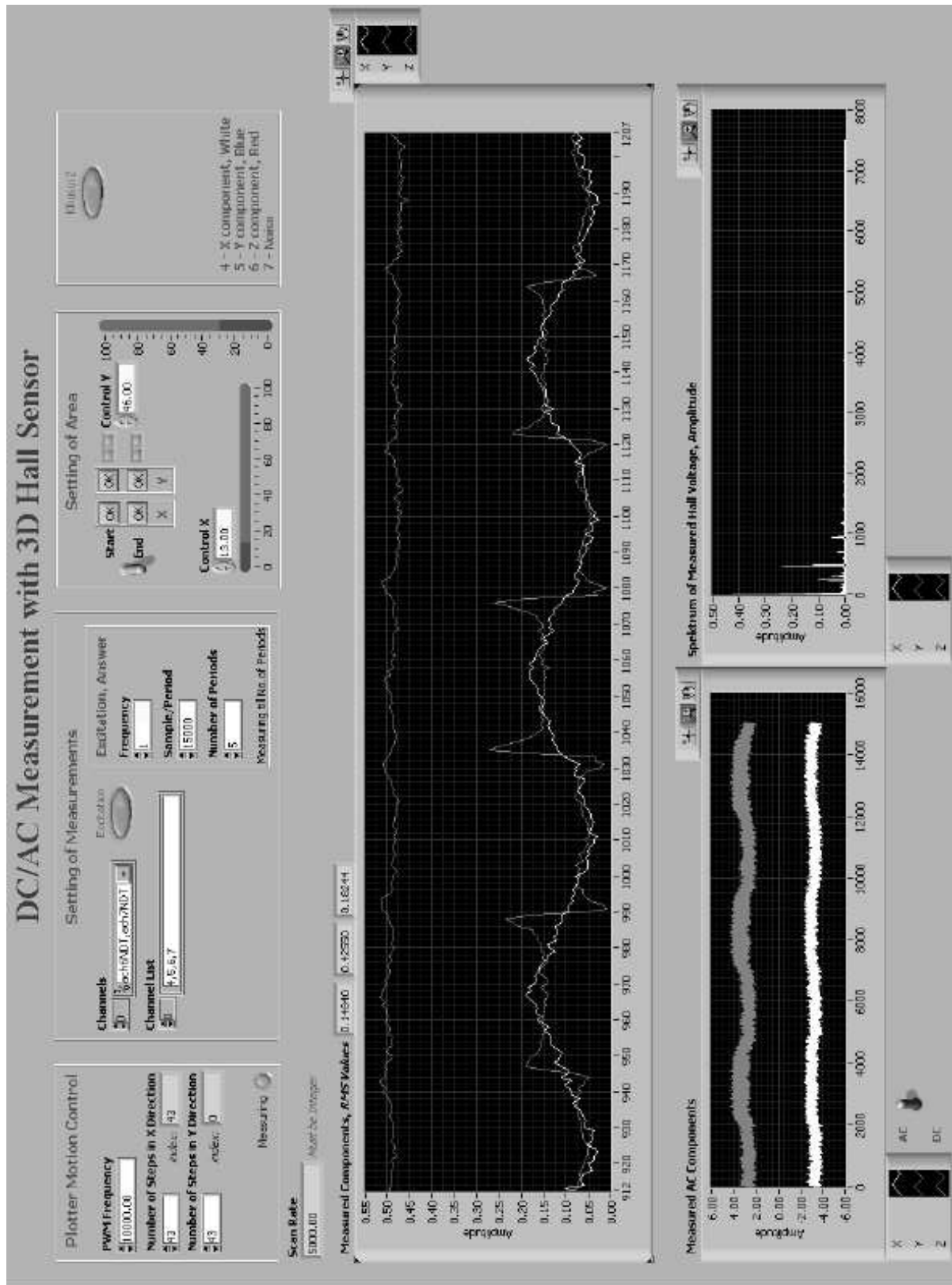


Fig. 5.11. LabVIEW GUI of the measurements

not enough to reach the saturation state of the material with the given number of turns of the exciting coil, i.e. the demagnetizing process is not perfect.

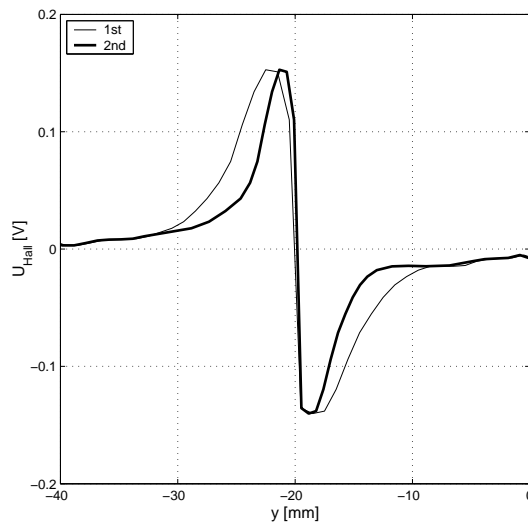
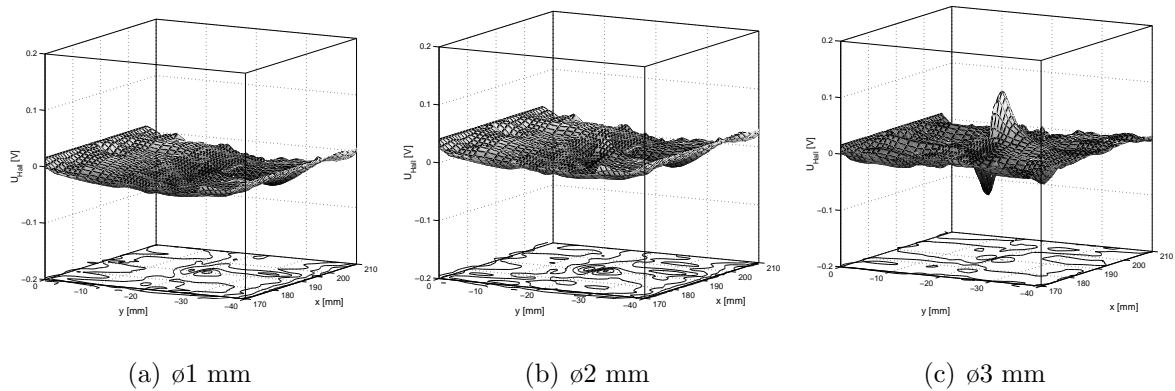


Fig. 5.12. Illustration for the effect of the moving mechanics

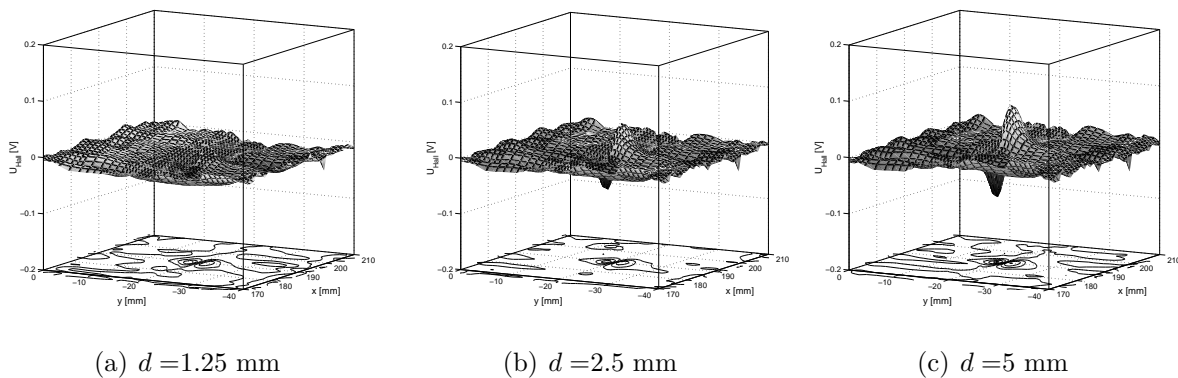


(a) $\phi 1$ mm

(b) $\phi 2$ mm

(c) $\phi 3$ mm

Fig. 5.13. Measurement results I, the effect of diameter of the crack



(a) $d = 1.25$ mm

(b) $d = 2.5$ mm

(c) $d = 5$ mm

Fig. 5.14. Measurement results II, the effect of depth of the crack

An important experiment when applying the Hall sensor is: measuring the z component of the magnetic field intensity gives more accurate contour plots than measuring the y component of the magnetic field intensity. However, the z directed coil of the FluxSet

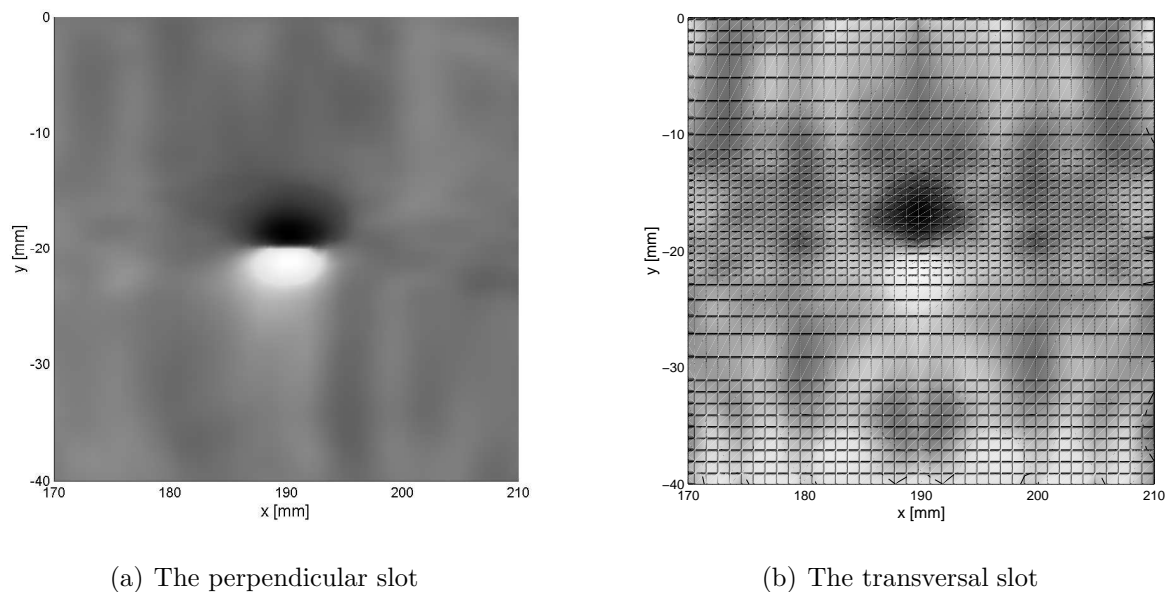


Fig. 5.15. Top view of the measured voltage

sensor is far from the surface of the specimen.

I have developed a 3D nonlinear FEM software to simulate the presented measurement system to compare calculations and the above measurements. I only focus on the measurements performed by the Hall sensor. Other important measured signals with comparisons with the simulated ones are also shown in the next section.

5.5 Simulation of the installed NDT equipment

The same mathematical formulations can be used as described in the previous chapter, but applying the 3D shape functions in tetrahedral finite elements ($I = 4$ and $K = 6$) and the 3D NN based vector hysteresis model [61].

On the basis of the 2D problem presented in the previous chapter, I have developed the 3D numerical simulation of the built NDT equipment. A global to local model has been used: first, a global model has been applied to determine the potential distribution near the crack, then a local domain including the crack has been investigated. The global model has been applied to determine the artificial boundary conditions of the local model.

Comparisons between the measured and the simulated crack signals are presented at the end of this section.

5.5.1 Global–local model in 3D calculations

The generated meshes, the boundary conditions and properties of the calculations

The size of a manufactured crack is very small comparing with the size of the whole arrangement: e.g. the diameter of a surface hole is maximum 2.5 mm and its depth is maximum 5 mm, the size of the U-shaped yoke is $320 \times 240 \times 5$ mm, i.e. the order is

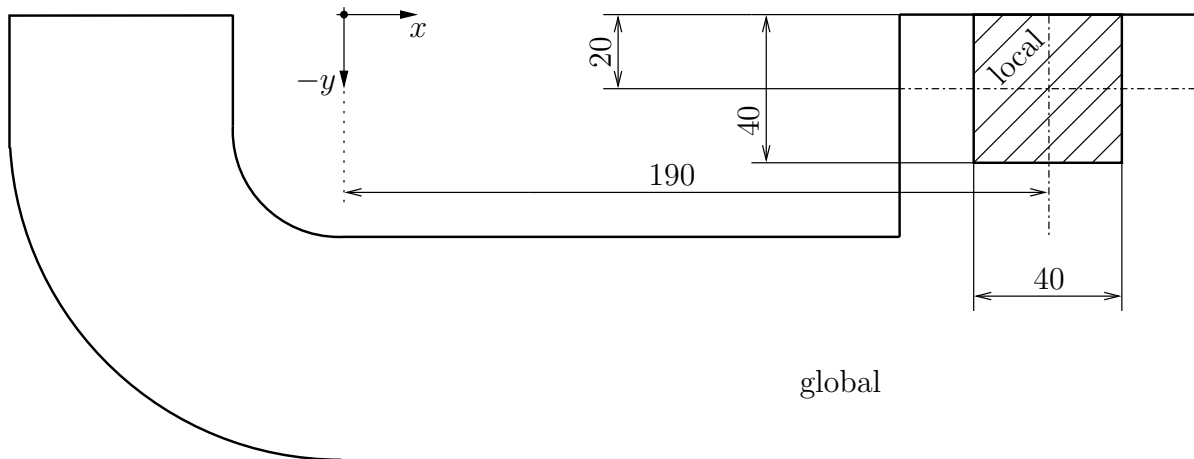


Fig. 5.16. The global to local model (dimensions are in mm)

two. The generated mesh of the whole arrangement is not accurate to simulate the effect of a crack. If a very dense mesh is used, then the number of unknowns is increasing very much (about 80000–120000 elements). On the other hand, if a coarse mesh is applied, then the system of equations is not very large, but the result around the crack is inaccurate, since the number of elements around the crack is very few. Unfortunately, I have experimented that, the iterative solvers of MATLAB cannot solve a system of equations with more than about 20000 unknowns (after solving the system of equations, the allocated memory will not be free).

Therefore, a global to local model (domain–decomposition) has been applied in two steps (see Fig. 5.16). I have generalized the domain–decomposition method in the time domain based on the static electric field calculations in [83]. First, a large–scale model without any crack is used to determine the boundary conditions of the local model, then the local domain including the crack is investigated. The size of the local domain is $40 \times 40 \times 20$ mm, $x \in [170, \dots, 210]$ mm, $y \in [-40, \dots, 0]$ mm, $z \in [-10, \dots, 10]$ mm, and the place of the crack is $x=190$ mm, $y=-20$ mm.

The FEM mesh of the global model can be seen in Fig. 5.17. This mesh consists of 2965 nodes, 15208 elements, and 8442 edges. Because of symmetry, I have analyzed only the half of the whole equipment. This mesh is accurate: I have stopped increasing the number of elements when I have attained no relevant changes in the numerical solution. I have calculated 3 periods, and one period has been divided into 40 time steps. Calculation time of the global model was about 7 days. This very long time can be associated to the large number of hysteresis characteristics, since I used one 3D vector hysteresis model placed in the barycenter of one finite element in iron (5150 element), and one vector model consists of 9 scalar hysteresis models resulting 46350 hysteresis models.

The effect of the current flowing in the exciting coils has been taken into account again by the impressed field quantity \mathbf{T}_0 calculated by the Biot–Savart law. Coils have been modelled with simple filamentary conductors, then \mathbf{T}_0 has been determined along every edge. The advantage of applying \mathbf{T}_0 can be sensed especially in 3D calculations, because the coils must not be meshed and the number of elements is much smaller.

The boundary conditions of the 3D eddy current field problem can be prescribed similarly to the 2D ones. Homogeneous boundary conditions are assumed at the artificial

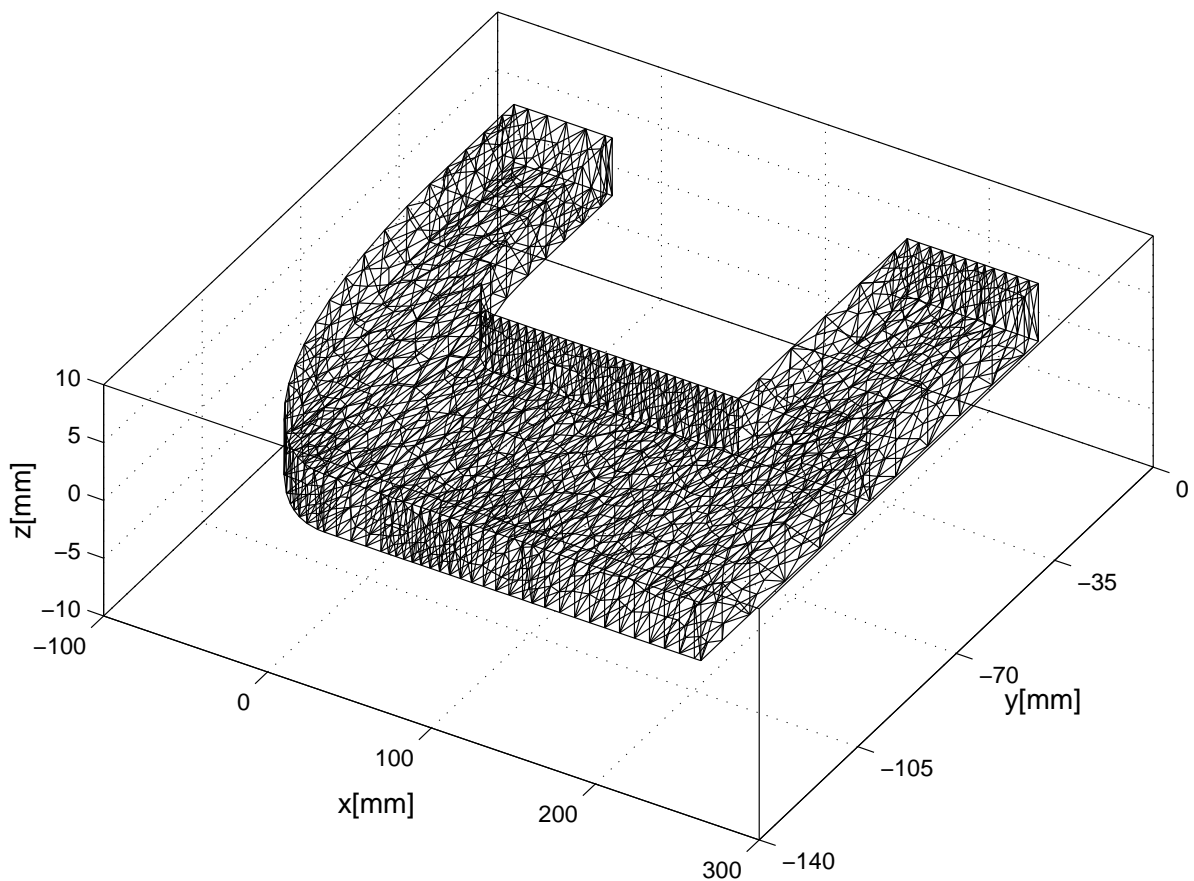


Fig. 5.17. Mesh of the global model; the generated mesh in air is not shown

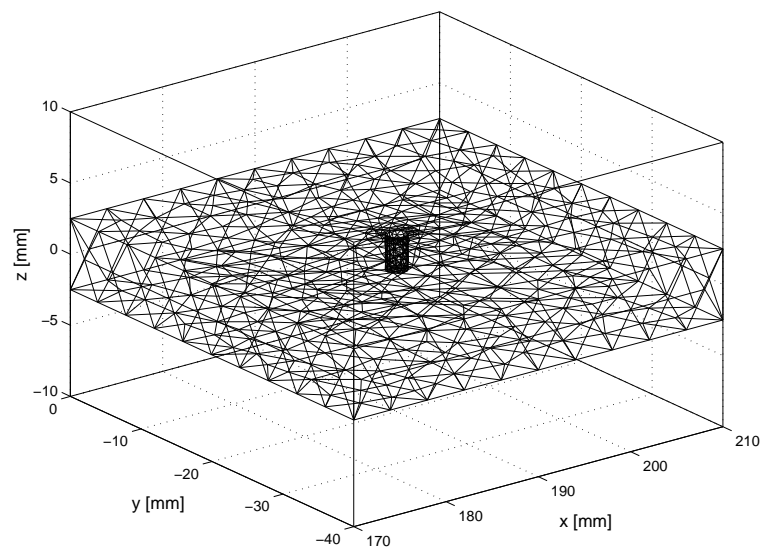


Fig. 5.18. Mesh of the local model with a hole; the generated mesh in air is not shown

far boundaries in air, i.e. the tangential component of the magnetic field intensity or the normal component of the magnetic flux density is zero, $\mathbf{H} \times \mathbf{n} = \mathbf{0}$ or $\mathbf{B} \cdot \mathbf{n} = 0$, where \mathbf{n} is the outer normal unit vector of the region. Homogeneous boundary conditions can be supposed along the symmetry planes: $\mathbf{H} \times \mathbf{n} = \mathbf{0}$, i.e. $\mathbf{J} \cdot \mathbf{n} = 0$ and $\mathbf{E} \times \mathbf{n} = \mathbf{0}$.

On the interface between the yoke and the air regions, the interface conditions must be satisfied: $\mathbf{H} \times \mathbf{n}$ and $\mathbf{B} \cdot \mathbf{n}$ must be continuous and $\mathbf{J} \cdot \mathbf{n} = 0$. The unknown vector potential \mathbf{T} has to set to be zero on the interface and along the symmetry plane. The magnetic scalar potential Ψ is set to be zero at the artificial far boundary and along the symmetry plane.

The global model has been applied on a coarse, but appropriate mesh to calculate the boundary conditions of the local model. The local model around the crack on a dense mesh (relative to the size of the analyzed domain) has been applied to calculate the field quantities more accurately. An example mesh of the local model is shown in Fig. 5.18. Parameters of the generated meshes of the local model (the number of nodes, the number of edges in iron, and the number of finite elements) for simulated cracks can be seen in the following table:

Crack	Nodes	Edges in iron	Element
ø3 mm	830	2503	3997
ø2 mm	1347	3950	6638
Slot1	624	1840	2941
Slot2	1494	4176	7343

For validation, I have performed calculations by applying denser meshes, but the above meshes turn out a success.

The algorithm for calculation of the boundary potentials of the local model is summarized as follows. Every node and every edge at the boundary of the local model must be converted into the space of the global model. Then the finite element of the global domain which contains the given nodes and edges must be found. The value of the potentials \mathbf{T} and Ψ on the boundary of the local domain can be calculated by using the shape functions and calculated potentials from the global model. These boundary potentials are stored at every time instant. Then the local model can be used. The interface condition for the local model is the same: the tangential component of the magnetic field intensity vector $\mathbf{H} \times \mathbf{n}$ must be continuous along the interface between the yoke and the air, i.e. the vector potential \mathbf{T} has been set to be zero on the interface.

Verification of the global model

I have calculated 3 periods to reach the steady state. The resulting magnetic flux density vectors can be seen in Fig. 5.19, when the exciting current has a maximum value of 8 A.

I have verified the global model by two methods. The first one is a simple analytical approach to verify the linear model. The peak value of the magnetic field intensity inside the yoke can be calculated approximately as $\hat{H} = N\hat{I}/l$, where $N = 129$ is the number of turns of the exciting coils, $\hat{I} = 8$ A is the peak value of the exciting current and $l = 0.86$ m is the equivalent magnetic length of the yoke. This calculation results $\hat{H} = 1200$ A/m. The linear time varying magnetic field calculations have resulted $\hat{H} \simeq 1095$ A/m, but the linear eddy current field calculations have resulted $\hat{H} \simeq 905$ A/m in the middle of the iron yoke. The magnetic field generated by the eddy currents decreases the magnetic field intensity. These simple comparisons give reassuring results to validate the linear global model.

Another verification of the global model has been done by the following comparison between the nonlinear simulations and the measurements. Simulations have been performed by applying a single valued inverse tangent type vector characteristic and the

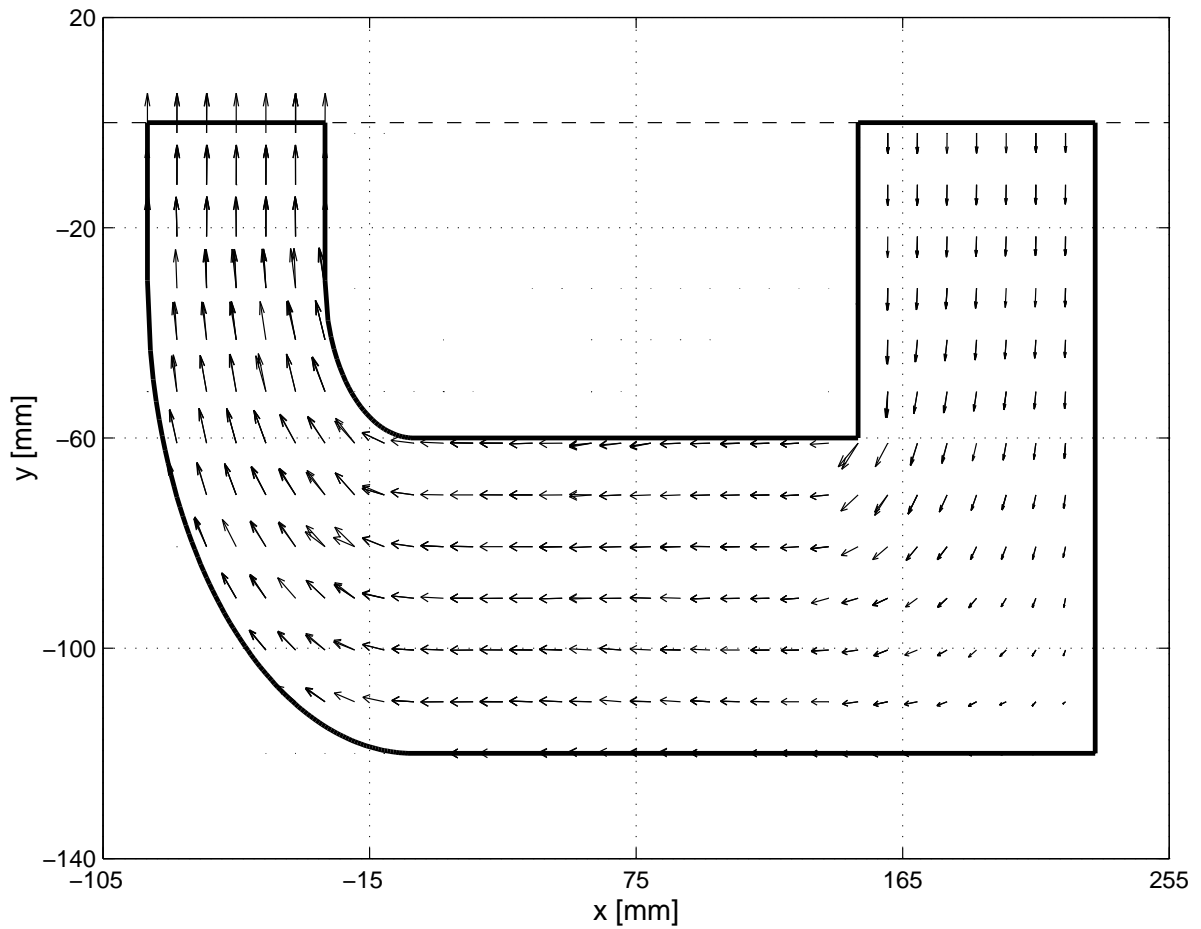


Fig. 5.19. The resulting magnetic flux density vectors inside the yoke simulated by the global model
(there are two layers, where the vectors are drawn: $z = -1.25$ mm and $z = 1.25$ mm)

3D NN based isotropic vector hysteresis model identified by the presented method (see Chapter 3). I have used real measurements applying a toroidal shape coil made of the same material as the specimen and as the yoke. I have supposed that, the material is an isotropic magnetic material. Characteristics are shown Fig. 5.20(a). The measurement was the following: I have measured the induced voltage of a coil wound the yoke's leg and I have calculated it as well. The number of turns of the measurement coil was $N = 100$. The Fig. 5.20(b) shows this comparison. These comparisons show the very good agreement between the simulations and the measurements, especially when I have applied the NN based vector hysteresis characteristic. However, applying the simpler inverse tangent type characteristic has also resulted accurate solution. The induced voltage simulated by the inverse tangent type characteristic is higher than the induced voltage simulated by the NN based vector hysteresis model, because the inverse tangent type characteristic is steeper and the induced voltage depends on the shape of the characteristic, i.e.

$$U_i = -N \frac{d}{dt} \int_S \mathbf{B} \cdot \mathbf{n} dS,$$

where S is the area of the yoke's leg. These simulations show the applicability of the NN based vector hysteresis model and of the proposed identification technique. The correctness of the applied global FEM mesh, the boundary conditions, the iteration

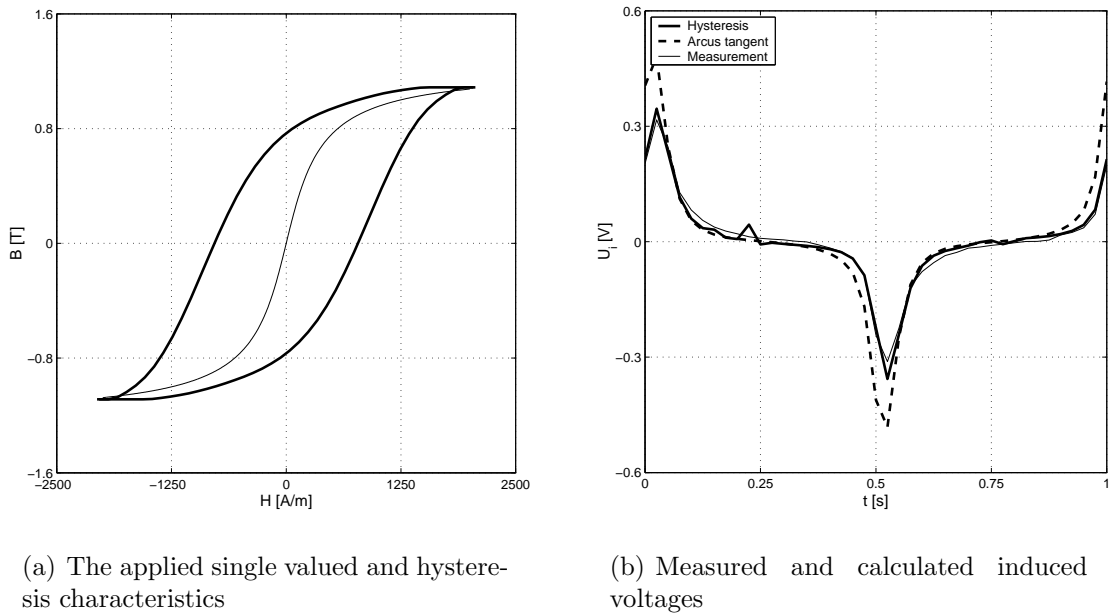


Fig. 5.20. Verification of the global model

scheme have also been validated by these calculations and comparisons.

Surface integrals in the local model

When the global model is applied, the boundary conditions on the artificial far boundary and on the symmetry plane can be subscribed easily. In the case of the local model, the surface integrals on the boundary cannot be neglected, because the local model is not symmetrical. If the local model is used, then the boundary conditions can be calculated from the global model as described above, and the terms from the surface integrals must be included into the assembled system of linear equations.

The following surface integrals are derived only in the 3D eddy current field problem using the local model.

There is a time varying magnetic field problem in the air region Ω_n , therefore the equation (4.10) has to be used, but the boundary integral term on Γ_n cannot be neglected, i.e.

$$\oint_{\Gamma_n} N_j \{ \mu_0 \mathbf{T}_0 - \mu_0 \nabla \Psi \} \cdot \mathbf{n} d\Gamma \neq 0. \quad (5.4)$$

This surface integral must be calculated at every triangular face of a tetrahedron connecting to the boundary as

$$\sum_{k=1}^6 \mu_0 \int_S N_j (\mathbf{W}_k \cdot \mathbf{n}) dS T_{0,k} - \sum_{i=1}^4 \mu_0 \int_S N_j (\nabla N_i) \cdot \mathbf{n} dS \Psi_i, \quad (5.5)$$

where S is the area of the face of the tetrahedron connecting to the boundary of the local model and \mathbf{n} is the outer normal unit vector of this surface triangle. The first sum is known and it has to be subtracted from the right hand side of (4.13). There are three nodes connecting to the boundary which potential value Ψ_i are known from the global model. These surface integral terms must also be assembled to the right hand side of

(4.13). There is only one node with unknown potential and the according term must be assembled to the left hand side of (4.13).

There is an eddy current field problem inside the specimen Ω_c , that is the boundary integral term from the integral (4.28) must be applied, i.e.

$$\oint_{\Gamma_c} N_j \{ \mu \mathbf{T}_0 + \mu \mathbf{T} - \mu \nabla \Psi \} \cdot \mathbf{n} \, d\Gamma \neq 0. \quad (5.6)$$

This surface integral must be calculated at every triangular face of a tetrahedron connecting to the boundary as

$$\begin{aligned} & \sum_{k=1}^6 \mu \int_S N_j (\mathbf{W}_k \cdot \mathbf{n}) \, dS \, T_{0,k} + \sum_{k=1}^6 \mu \int_S N_j (\mathbf{W}_k \cdot \mathbf{n}) \, dS \, T_k \\ & - \sum_{i=1}^4 \mu \int_S N_j (\nabla N_i) \cdot \mathbf{n} \, dS \, \Psi_i. \end{aligned} \quad (5.7)$$

The surface integral in (4.24)

$$\oint_{\Gamma_c} \mathbf{W}_j \times \left\{ \frac{1}{\sigma} \nabla \times \mathbf{T}_0 + \frac{1}{\sigma} \nabla \times \mathbf{T} \right\} \cdot \mathbf{n} \, d\Gamma \quad (5.8)$$

gives

$$\begin{aligned} & \sum_{k=1}^6 \frac{1}{\sigma} \int_S \mathbf{W}_j \cdot (\nabla \times \mathbf{W}_k \times \mathbf{n}) \, dS \, T_{0,k} \\ & + \sum_{k=1}^6 \frac{1}{\sigma} \int_S \mathbf{W}_j \cdot (\nabla \times \mathbf{W}_k \times \mathbf{n}) \, dS \, T_k. \end{aligned} \quad (5.9)$$

There are three nodes and three edges of a tetrahedron connecting to the boundary of the local model. The according potentials Ψ_i and T_k are known from the global model and these surface integral terms must be assembled to the right hand side of (4.29) and (4.27). There is only one node and three edges with unknown potentials and the according terms must be assembled to the left hand side of (4.29) and (4.27).

In the case of taking into account the hysteresis characteristic of the nonlinear media, the surface integral

$$\oint_{\Gamma_c} N_j (\mathbf{R}_{FP} \cdot \mathbf{n}) \, d\Gamma \quad (5.10)$$

from the weak form of the partial differential equation (4.36) must also be inserted. The value of $\mathbf{R}_{FP} \cdot \mathbf{n}$ is constant in one finite element and must be subtracted from the right hand side of the according equations. In this case, the above surface integrals should be modified as $\mu = \mu_{FP}$.

A comparison between the magnetic induction vectors inside the specimen according to the area of the local domain, calculated using the global model and using the local model can be seen in Fig. 5.21(a) and Fig. 5.21(b). The maximum relative difference between the calculated induction vectors is about 5%. This comparison shows the accuracy of the global–local model.

The global model is a time consuming model, but this must be used only once. The local model can be applied to simulate all of the measured cracks (the computation time of the local model is about 2 hours).

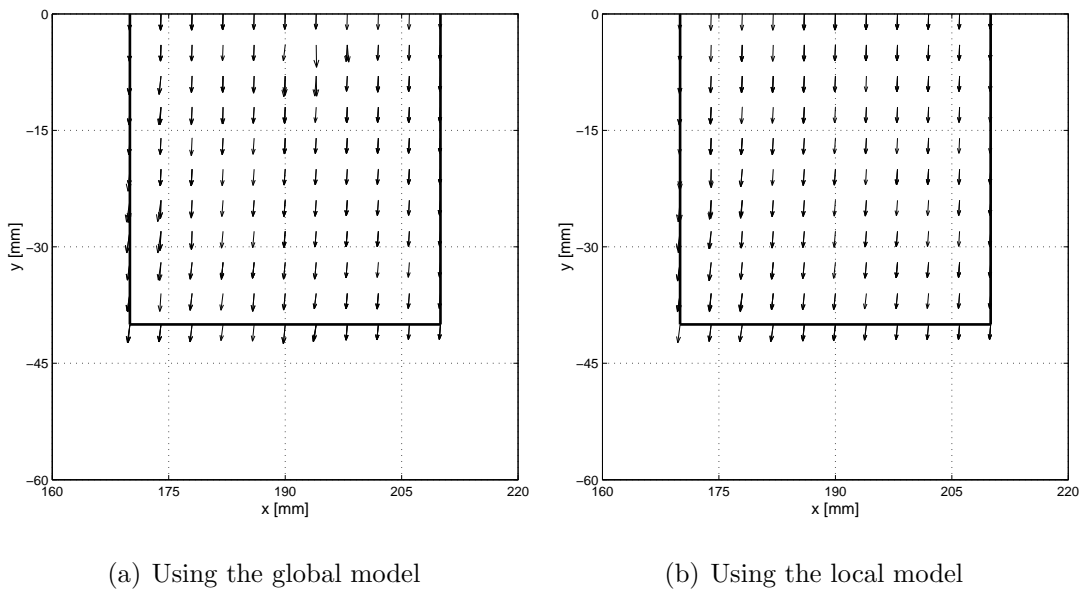


Fig. 5.21. Comparison between the resulting \mathbf{B} vectors (there are two layers, where the normalized vectors are drawn: $z = -1.25$ mm and $z = 1.25$ mm)

5.5.2 Simulation of the Hall sensor

Calculation of the output signal

The gradient of the measured and of the calculated signal $\frac{\partial U}{\partial y}$ is increasing near to the crack, because this signal is varying rapidly. Let us have a look at to Fig. 5.22. The simulated signal is narrower than the measured one, therefore I have used the following calibration process (it may be that, the mechanics of the positioning device has disturbed the measurements, however I have used a spacer as presented in the section 5.3.2).

First of all, I have calculated the magnetic field intensity vector $\mathbf{H} = \mathbf{T}_0 - \nabla\Psi$ at the scanning points along the scanning line through the center of the crack above the specimen ($x = 190$ mm, $y = -40, \dots, 0$ mm). I have supposed that, the sensor is a pointwise instrument, i.e. I have just multiplied the z -component of the magnetic field intensity vector (H_z) by the calibrating factor $k = 5.095 \cdot 10^{-4}$ Vm/A which has been determined by the calibrating solenoid (see section 5.3.1). This results a very narrow signal as can be seen in Fig. 5.22, however the simulated peak values are very close to the measured ones. This signal is a bit staged, because $\nabla\Psi$ is constant in a finite element, since I have used first order shape functions.

Second, I have supposed that, the sensor is not a pointwise instrument, but a very small one with the length of 2.9 mm. I have calculated the magnetic field intensity at 5 given points along the axis of the sensor and a linear combination of these magnetic field intensities multiplied by the calibration factor k results in a better simulation (it is denoted by $k'H$). This is a similar calibration process presented in the calibration of the FluxSet sensor (see section 5.2.2). The above calibration technique has to be used, because the length of the Hall sensor is commensurable with the size of the cracks.

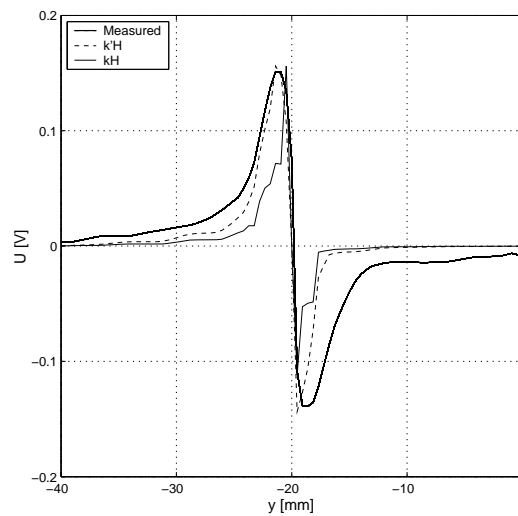


Fig. 5.22. The calibration is needed along the axis of the sensor

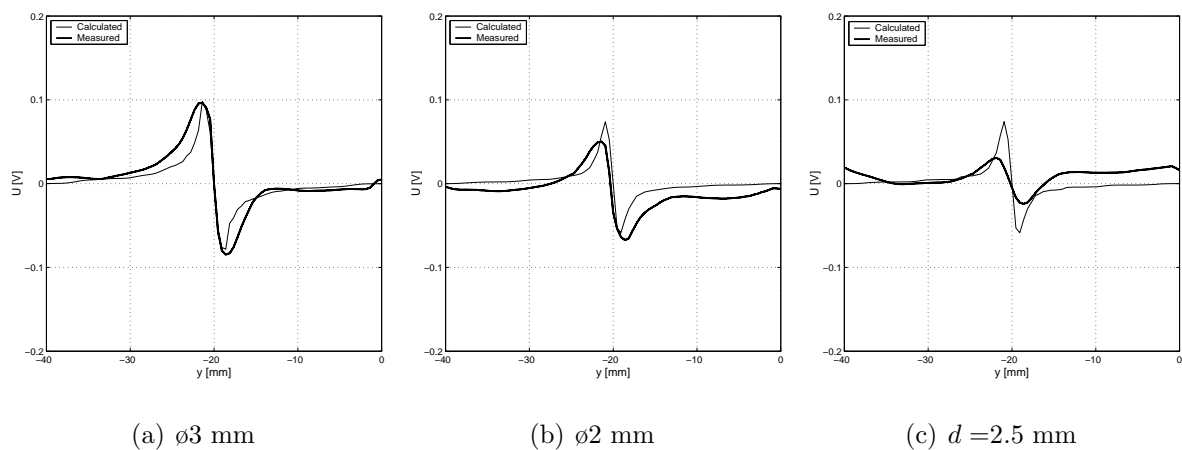


Fig. 5.23. Comparison between measured and simulated signals (I)

Comparison between the measured signals and the simulation results

I have simulated some measured crack signals which are not buried with a large noise.

First, the magnetic field intensity map according to the holes has been analyzed. I have simulated the output voltage of the sensor according to the holes with the diameter of 3 mm and of 2 mm, and the results are plotted in Fig. 5.23(a) and Fig. 5.23(b). In this case, the Hall sensor is moving through the scanning line $x = 190$ mm, $y = -40, \dots, 0$ mm which is along the center point of the cracks. A comparison between the measured and the simulated signals according to the hole with the depth of 2.5 mm can be seen in Fig. 5.23(c). Simulated signals shown in Fig. 5.23(b) and Fig. 5.23(c) are the same, because the two cracks are the same on another specimen. The values of the measured signals are different, however the waveform is similar.

The next analysis is to compare the measured and the simulated signals according to the surface slots. The results are plotted in Fig. 5.24(a) and Fig. 5.24(b). The measured

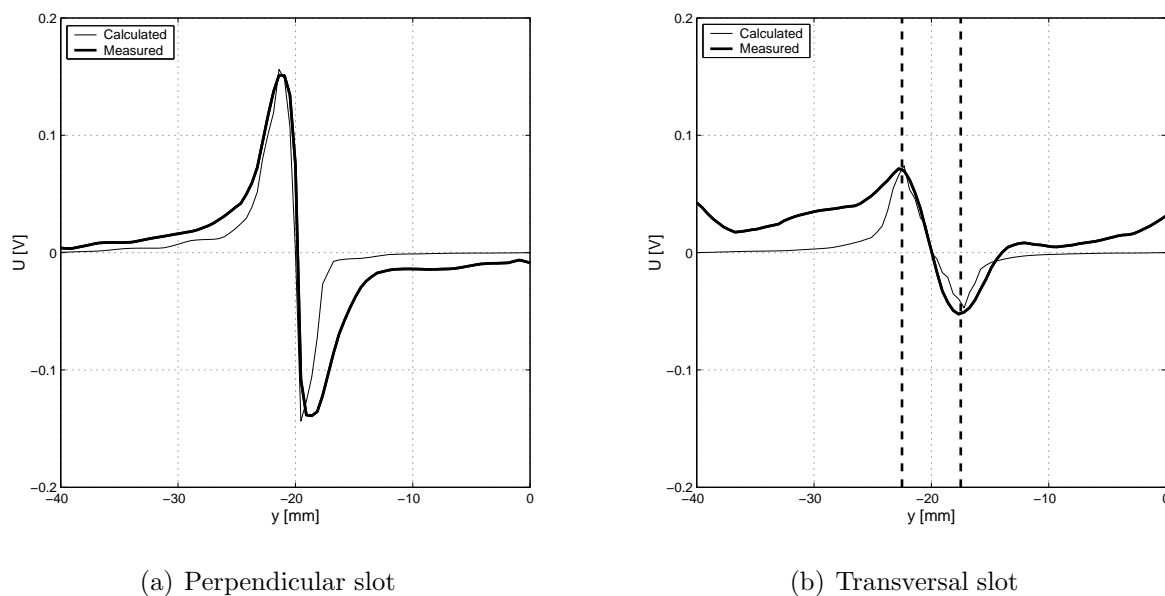


Fig. 5.24. Comparison between measured and simulated signals (II)

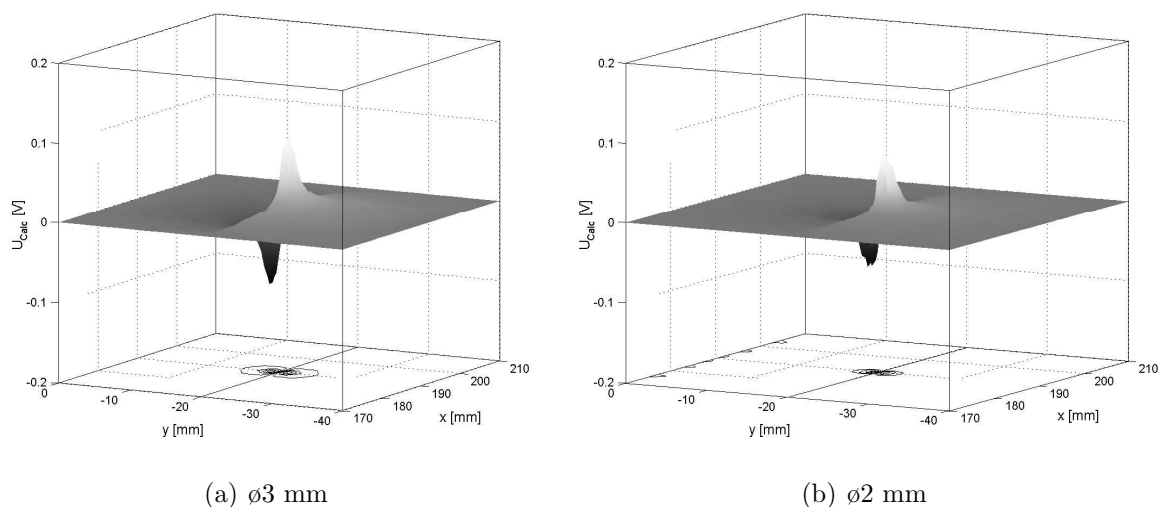


Fig. 5.25. Simulated surfaces above the scanning area

signal of the transversal slot is more noisy than the signal of the perpendicular slot as it can be seen in the figures. The size of the transversal is also presented, where the signal reach the maximum and the minimum peaks. These measurements have given the most accurate results, since the measurements and the simulations are in a good agreement. The location of the measured and of the calculated maximum and minimum peaks are very close to each other.

I have simulated the scanning process by calculating the signal of the sensor at the same scanning points which I have measured. Simulated results according to the holes with the diameter of 3 mm and of 2 mm are shown in Fig. 5.25(a) and Fig. 5.25(b). It can be seen easily that, the calculated signals are narrower than the measured ones by comparing measured (see Fig. 5.13(c) and Fig. 5.13(b)) and the above simulated signals,

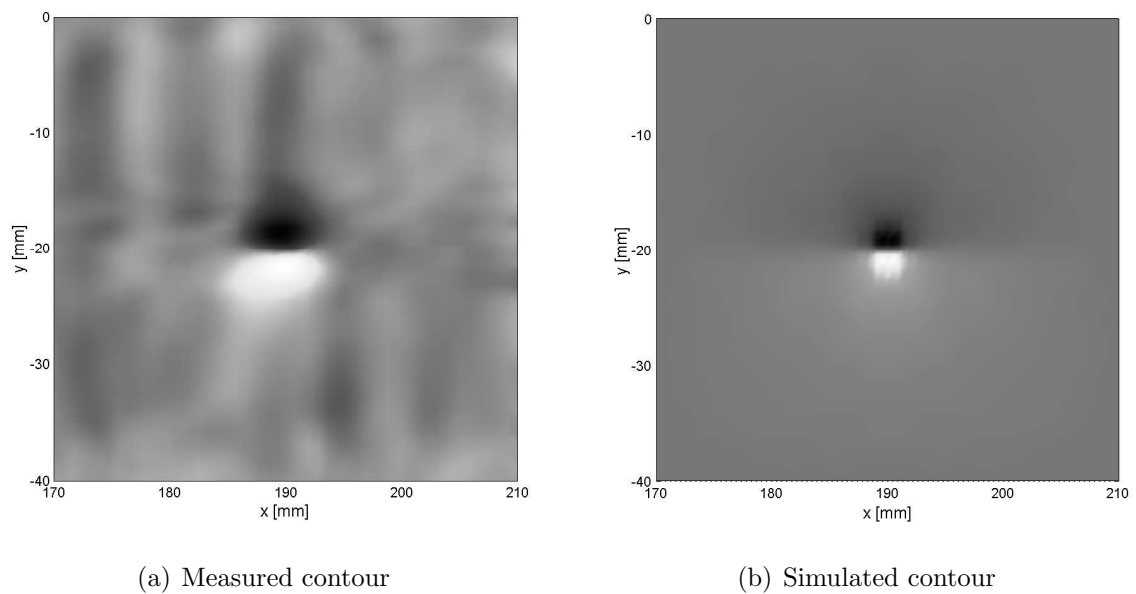


Fig. 5.26. Comparison between the measured and the simulated contour plots of the crack $\varnothing 2$ mm

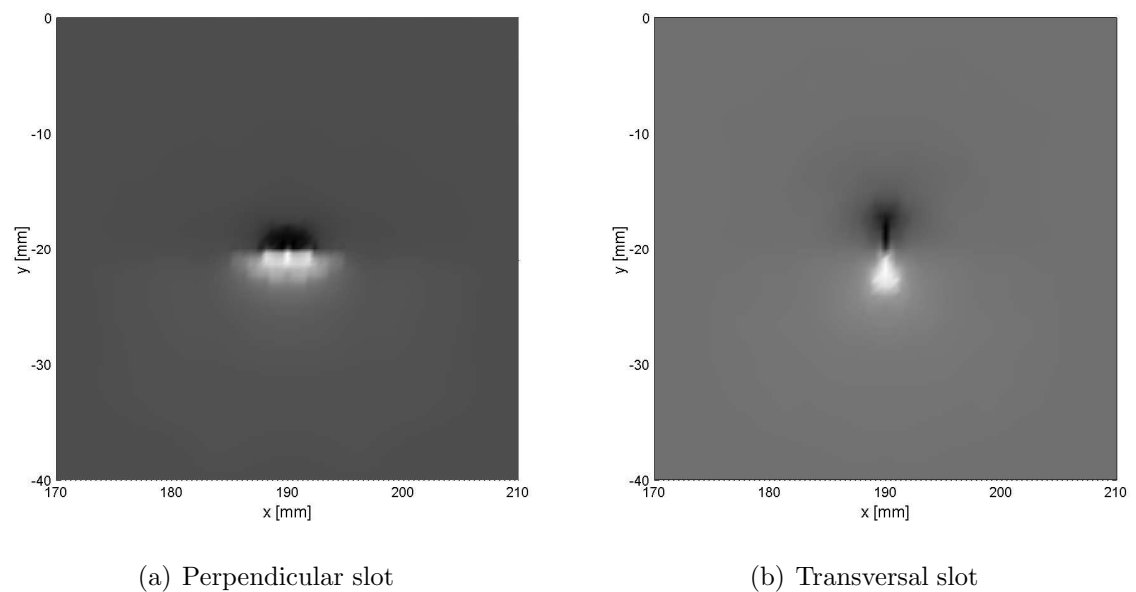


Fig. 5.27. Simulated contour plots above the surface slots

however the peak values and the shape of the signals show very good agreement.

The measured and the simulated contour plot of the signals according the surface hole with the diameter of 2 mm can be seen in Fig. 5.26(a) and Fig. 5.26(b). The difference between the measured and the simulated signals can also be seen, i.e. the simulated signal is narrower, and the size of the hole could be deduced easier from the simulated signal than from the measured one. The comparison between the peak values of the measured and of the simulated output voltages show very good agreement.

The simulated contour plot of the signals according the surface slots can be seen in

Fig. 5.27(a) and Fig. 5.27(b). The size and the orientation of the slots can be determined easier from simulations than from measurements (see Fig. 5.15(a) and Fig. 5.15(b)). It can also be seen that, the simulated signals are narrower than the measured ones.

The location and the orientation of the manufactured surface holes and slots can be determined easier from simulations than from measurements, since simulated signals are narrower than the measured ones and calculations are not buried with noise.

Conclusions

A more precise measurement arrangement would result much better agreement between the measurements and the simulations, however I could reach my aim, i.e. to simulate accurately the test equipment, to check the developed nonlinear FEM software and the NN based vector hysteresis characteristic by the comparisons between the measurements and the simulations.

The comparison between the measured and the simulated induced voltages has shown very good agreement. This global quantity can be measured easily, because the errors from measurements are averaging. The crack signals are measured in the scanning points and this measurement is buried with local noise and local measurement error.

5.6 New scientific results

3. Thesis I have confirmed the three dimensional nonlinear simulation technique by comparing simulated and measured results. I have worked out a measurement system which is able to detect the surface cracks of a specimen and I have developed the numerical simulation of this arrangement. I have worked out the global to local model (domain-decomposition) of the arrangement in the time domain. The boundary conditions of the local model have been calculated by using the global model. I have compared the simulated and the measured output signal of the Hall sensor, and these comparisons show very good agreement.

3.a I have built a measurement system to analyze the FluxSet sensor and the Hall-type sensor in the field of measuring the crack signals. I have examined the signals corresponding to cracks with different size and shape. I have worked out calibration methods to predict the output voltage of the sensors by using simple arrangements. The measurements are performed by using the software environment LabVIEW.

3.b I have developed the three dimensional nonlinear numerical analysis of the built nondestructive testing measurement system and I have used the finite element method and the $\mathbf{T}, \Psi - \Psi$ potential formulation. I have developed a global to local model of the built arrangement in the time domain. I have used the global model without any crack to predict the artificial boundary conditions of the local model where the crack has been taken into account. I have developed the surface integrals obtained from the weak form of the partial differential equations necessary to use in the local model. I have implemented the identified three dimensional neural network based isotropic vector hysteresis model to the eddy current field problem by applying the fixed-point iteration technique and the B -scheme of the polarization method. The comparisons between the measured crack signals performed by the Hall sensor and the simulation results show the good applicability of the developed model.

Chapter 6

Summary of the new scientific results

Finally, I gather my research work in the field of hysteresis modeling and of the FEM.

1. Thesis I have developed a new scalar hysteresis operator based on the function approximation capability of the neural networks to simulate the behavior of ferromagnetic materials. I have represented the first order reversal curves with a surface by introducing the variable ξ and I have approximated this surface by neural network technique. I have built a knowledge-base which contains if-then type rules about the behavior of the hysteresis characteristics. I have shown the applicability of the model by comparing simulated and measured results. I have taken into account the vectorial behavior of the magnetic field intensity and the magnetic flux density by applying the neural network based vector hysteresis model, and I have recommended a new identification procedure to build up the vector model. I have worked out the three dimensional anisotropic vector hysteresis model, and I have analyzed the behavior of the developed vector models.

- 1.a I have developed a new neural network based mathematical representation of the scalar hysteresis operator. I have handled the multivalued property of the hysteresis characteristics by introducing the new variable ξ associated with the measured first order reversal curves. This preprocessing can be applied on any kind of hysteresis characteristics. I have built a knowledge-base which contains if-then type rules about the behavior of the hysteresis characteristics. This is the memory mechanism of the model. I have realized the identification procedure by the training of the neural networks. I have built a measurement system to measure hysteresis curves on a toroidal shape C19 structural steel, and I have used these measurements to show the applicability of the neural network based scalar hysteresis model by comparing measurements and simulation results.
- 1.b I have developed the two dimensional and the three dimensional isotropic vector hysteresis models based on the neural network based scalar model. I have worked out an original and new identification procedure based on the measurable Everett function both to predict two dimensional and three dimensional isotropic hysteresis characteristics. I have compared the measured and the predicted curves and I have shown the behavior of the vector model in linear and in rotational magnetic fields.

- 1.c I have developed the two dimensional and the three dimensional neural network based anisotropic vector hysteresis models by the means of Fourier expansion of the measured Everett function of the anisotropic material. I have generalized the two dimensional model in three dimensions as a theoretical expansion of the two dimensional model, and I have recommended an identification procedure to fit to measured curves. I have compared the measured and the predicted curves and I have shown the behavior of the vector model in linear and in rotational magnetic fields, finally I have compared the isotropic and the anisotropic models.

2. Thesis I have implemented the developed neural network based vector hysteresis model to the finite element method. I have applied the Ψ and the $\mathbf{T}, \Psi - \Psi$ potential formulations, because these directly give the magnetic field intensity vector which is the input variable of the direct vector hysteresis model. I have used the nodal and the edge shape functions for the approximation of the potentials. I have handled the neural network based vector hysteresis model by applying the B -scheme of the polarization method, and I have solved the linearized system of equations by the fixed-point iteration technique. I have used an under-relaxation scheme to speed up the convergence of the method. This results in a convergent and a well applicable method to solve both time varying magnetic field problem and eddy current field problem.

3. Thesis I have confirmed the three dimensional nonlinear simulation technique by comparing simulated and measured results. I have worked out a measurement system which is able to detect the surface cracks of a specimen and I have developed the numerical simulation of this arrangement. I have worked out the global to local model (domain-decomposition) of the arrangement in the time domain. The boundary conditions of the local model have been calculated by using the global model. I have compared the simulated and the measured output signal of the Hall sensor, and these comparisons show very good agreement.

- 3.a I have built a measurement system to analyze the FluxSet sensor and the Hall-type sensor in the field of measuring the crack signals. I have examined the signals corresponding to cracks with different size and shape. I have worked out calibration methods to predict the output voltage of the sensors by using simple arrangements. The measurements are performed by using the software environment LabVIEW.
- 3.b I have developed the three dimensional nonlinear numerical analysis of the built nondestructive testing measurement system and I have used the finite element method and the $\mathbf{T}, \Psi - \Psi$ potential formulation. I have developed a global to local model of the built arrangement in the time domain. I have used the global model without any crack to predict the artificial boundary conditions of the local model where the crack has been taken into account. I have developed the surface integrals obtained from the weak form of the partial differential equations necessary to use in the local model. I have implemented the identified three dimensional neural network based isotropic vector hysteresis model to the eddy current field problem by applying the fixed-point iteration technique and the B -scheme of the polarization method. The comparisons between the measured crack signals performed by the Hall sensor and the simulation results show the good applicability of the developed model.

Chapter 7

Conclusions and future developments

A neural network based hysteresis operator has been presented in this work. The identification of the scalar model is a simple training method on measured and preprocessed first order reversal curves. The vector hysteresis model in 2D and in 3D has also been implemented for both the isotropic and the anisotropic case. While the scalar hysteresis measurement is an easy task, the measurement of the 2D vector hysteresis characteristics is a great challenge, and it is a large project. There are some problems on the measurements of the magnetic field intensity as can be found in the literature. It is a future work to build a vector hysteresis measurement system in our laboratory. The 3D vector hysteresis measurement is an open question, I have not found any paper about this topic. I have developed a theoretical representation of the 3D anisotropic model, but I think there may be several generalizations of this model.

I have built a measurement system which is able to perform simple NDT measurements. It is important to note that, I have used this system to check my computations. Building a measurement system is a hard work, because several problems can be emerged, such as the system noise, and other phenomena, that disturb the measurement. This is true for all measurement systems. I have found that, a more precise x - y positioning device should be used. The positioning device may be the weak point in my measurements. I think that, a more sensitive sensor can be built by using the developed Hall-type probe and by making a sensor matrix with 3×3 or 5×5 sensors.

At the last part of the presented work, I have presented the implemented FEM code to simulate the built measurement system. As it was presented, the main goal was to build the developed neural network based vector hysteresis model into the FEM. The nonlinear behavior of the hysteresis characteristics has been handled by the fixed-point technique which results relatively long computation time, especially in 3D case using the global model. The Newton-Raphson type iterative methods may give faster solution.

Another and very important observation is that, a stand alone software should be used to simulate any arrangement, when applying the FEM. The software package MATLAB is very powerful, but this is very slow in this case, i.e. a C-code (especially a parallel code running on a parallel computer) may be a better alternative. Higher order shape functions may also give better approximation as well [101, 102]. In the case of higher order shape functions, some case study have to be done (e.g. solving TEAM problems).

Bibliography

- [1] A.A. Adly and S.K. Abd-El-Hafiz. Using neural networks in the identification of Preisach-type hysteresis models. *IEEE Trans. on Magn.*, 34(3):629–635, 1998.
- [2] A.A. Adly, S.K. Abd-El-Hafiz, and I.D. Mayergoyz. Identification of vector Preisach models from arbitrary measured data using neural networks. *Magnetic Imaging and Modeling*, 87(9):6821–6823, 2000.
- [3] R. Albanese, E. Coccorese, G. De Santis, R. Martone, and C. Create. A neural network based technique for non destructive evaluation exploiting soft computing concepts. *Nondestructive Testing of Materials*, pages 1–12, 1995.
- [4] M. Berend and E. Berend. *Biological Lexicon for Students (in Hungarian)*. Akadémia Kiadó, Budapest, 1996.
- [5] G. Bertotti. *Hysteresis in Magnetism*. Academic Press, 1998.
- [6] O. Bíró. Edge element formulations of eddy current problems. *Comput. Meth. Appl. Mech. Engrg.*, 169:391–405, 1999.
- [7] O. Bíró, K. Hollaus, J. Pávó, and K. Preis. Numerical computation of the magnetic field due to a crack in a conducting plate. *Electromagnetic Nondestructive Evaluation (V)*, pages 11–15, 2001.
- [8] I. Bojtár and Zs. Gáspár. *Finite Element Method for Engineers*. TERC, Budapest, 2003.
- [9] A. Bossavit. *Computational Electromagnetism*. Academic Press, Boston, 1998.
- [10] I.D.O. Bottauscio, D. Chiarabaglio, C. Ragusa, M. Chiampi, and M. Repetto. Analysis of isotropic materials with vector hysteresis. *IEEE Trans. on Magn.*, 34:1258–1260, 1997.
- [11] O. Bottauscio, M. Chiampi, and C. Ragusa. Transient analysis of hysteretic field problems using fixed point technique. *IEEE Trans. on Magn.*, 39(3):1179–1182, 2003.
- [12] J. Bowler. Pulsed eddy current inversion for the determination of crack shape. *Electromagnetic Nondestructive Evaluation*, pages 263–269, 1997.
- [13] T. Chady, M. Enokizono, R. Sikora, and K. Takeuchi. Eddy current testing of concrete structures. *International Journal of Applied Electromagnetics and Mechanics*, 15:33–37, 2001/2002.

-
- [14] T. Chady, M. Enokizono, and R. Sykora. Signal restoration using dynamic neural network model for eddy current nondestructive testing. *IEEE Trans. on Magn.*, 37(5):3737–3740, 2001.
- [15] T. Chady, M. Enokizono, T. Todaka, Y. Tsuchida, and R. Sykora. Evaluation of the JSAEM round robin test samples using multi-frequency excitation and spectrogram method. *Electromagnetic Nondestructive Evaluation (V)*, pages 171–178, 2001.
- [16] W. Cheng, K. Miya, and K. Demachi. Application of FEM-BEM coupling method to eddy current testing problem. *Electromagnetic Nondestructive Evaluation (IV)*, pages 17–24, 2000.
- [17] M. Chiampi, A.L. Negro, and M. Tartaglia. A finite element method to compute three-dimensional magnetic field distribution in transformer cores. *IEEE Trans. on Magn.*, MAG-16(6):1413–1419, 1980.
- [18] S. Chikazumi. *Physics of Magnetism*. John Wiley and Sons, New York, 1964.
- [19] C. Christodoulou and M. Georgiopoulos. *Applications of Neural Networks in Electromagnetics*. Artech House, Norwood, 2001.
- [20] S. Cincotti. Approximation properties of a PWL circuit model of hysteresis. *Physica B*, 275:216–222, 2000.
- [21] V. Cingoski. *Study on Improved Three-Dimensional Electromagnetic Field Computations Utilizing Vector Edge Finite Elements*. PhD thesis, Hiroshima University, 1996.
- [22] Kikusui Electronics Corporation. *Operation Manual, PBX Series*. KIKUSUI, Japan, 1992-2000.
- [23] M. Dotterweich, G. Szymanski, and M. Waszak. Approximation of the Preisach function using feedforward neural network approximator. *International Journal of Applied Electromagnetics and Mechanics*, 17 (1-3):243–250, 2003.
- [24] L.R. Dupre, O. Bottuascio, M. Chiampi, M. Repetto, and J.A.A. Melkebeek. Modeling of electromagnetic phenomena in soft magnetic materials under unidirectional time periodic flux excitation. *IEEE Trans. on Magn.*, 35(5):4171–4184, 1999.
- [25] G. Horváth (editor). *Neural Networks with Applications (in Hungarian)*. Műegyetemi Kiadó, Budapest, 1998.
- [26] G. Stoyan (editor). *Matlab, version 4. and 5. (in Hungarian)*. TypoTex, Budapest, 1999.
- [27] V.R. Vemuri (editor). *Artificial Neural Networks, Concepts and Control Applications*. IEEE Computer Soc. Press, Los Alamos, California, 1992.
- [28] M. Enokizono, T. Chady, T. Todaka, and Y. Tsuchida. Frequency scanning in NDE using multi-frequency excitation system. *Energy and Information in Non-Linear Systems*, pages 90–93, 2001.

- [29] Gy. Fodor. *Electromagnetic Fields (in Hungarian)*. Műegyetemi Kiadó, 1996.
- [30] J. Füzi. Computationally efficient rate dependent hysteresis model. *COMPEL*, 18(3):445–457, 1999.
- [31] J. Füzi, A. Iványi, and Zs. Szabó. Preisach model with continuous output in electrical circuit analysis. *Journal of Electrical Engineering, Bratislava, Slovakia*, 48:18–21, 1997.
- [32] J. Füzi, Gy. Székely, and Zs. Szabó. Experimental construction of classical Preisach model. *Proceedings of the 8th IGTE Symposium, Graz, Austria*, pages 452–457, 1998.
- [33] A. Gasparics, Cs.S. Daróczi, S. Calcagno, V. Mollo, R. Albanese, and J. Pávó. Comparative study on the performance of ECT probes. *Electromagnetic Nondestructive Evaluation (IV)*, pages 227–234, 2000.
- [34] V. Gorican, A. Hamler, M. Jesenik, B. Stumberger, and M. Trlep. Unreliable determination of vector B in 2-D SST. *Journal of Magnetism and Magnetic Materials*, 254-255:130–132, 2003.
- [35] Sz. Gyimóthy. *Adaptív automatikus hálógenerálás a végeselem módszerhez*. PhD thesis, Budapest University of Technology and Economics, 2003.
- [36] M. Hano, T. Miyamura, and M. Hotta. Finite element eddy current analysis by novel mixed-order vector elements. *International Journal of Applied Electromagnetics and Mechanics*, 14:19–22, 2001/2002.
- [37] H. Hoshikawa, K. Koyama, H. Hayakawa, and H. Morisaki. Study on the appropriate exciter-to-detector distance in remote field eddy current tubing inspection. *Electromagnetic Nondestructive Evaluation (IV)*, pages 71–78, 2000.
- [38] National Instruments. *LabVIEW, Basics Manual*. -, 2000.
- [39] A. Iványi. *Hysteresis Models in Electromagnetic Computation*. Akadémia Kiadó, Budapest, 1997.
- [40] A. Iványi. *Magnetic Field Computation with R-functions*. Akadémia Kiadó, Budapest, 1998.
- [41] A. Iványi. *Continuous and Discrete Simulations in Electrodynamics (in Hungarian)*. Akadémia Kiadó, Budapest, 2003.
- [42] Sz. Jagasics. *Building a 3D Hall-type sensor*. Budapest, 2003.
- [43] D.C. Jiles. *Introduction to Magnetism and Magnetic Material*. Chapman and Hall, London, 1991.
- [44] Gy. Kádár and E.D. Torre. Hysteresis modeling: I. Noncongruency. *IEEE Trans. on Magn.*, MAG-23(5):2820–2822, 1987.
- [45] Gy. Kádár and E.D. Torre. Determination of the bilinear product Preisach function. *J.Appl. Phys.*, 63(8):3001–3003, 1988.

-
- [46] Gy. Kajdi. *Material Testing with Eddy Currents (in Hungarian)*. Professional Extension and Company, Budapest, 1990.
- [47] P. Kis and A. Iványi. Computer aided magnetic hysteresis measurement in LabVIEW environment. *Journal of Electrical Engineering*, 53(10):173–176, 2002.
- [48] P. Kis, M. Kuczmann, and A. Iványi. Hysteresis measurement in LabVIEW. *Physica B*, 343:357–363, 2004.
- [49] P.I. Koltermann, J.P.A. Bastos, N. Sadowski, N.J. Batistela, A. Kost, L. Janicke, and K. Miethner. Nonlinear magnetic field model by FEM taking into account hysteresis characteristics with M-B variables. *IEEE Trans. on Magn.*, 38(2):897–900, 2002.
- [50] M. Kuczmann and A. Iványi. Neural network based scalar hysteresis model. *International Journal of Applied Electromagnetics and Mechanics*, pages 225–230, 2001/2002.
- [51] M. Kuczmann and A. Iványi. Isotropic and anisotropic vector hysteresis model based on neural networks. *Journal of Electrical Engineering 9/s*, pages 73–76, 2002.
- [52] M. Kuczmann and A. Iványi. Measuring and identification of scalar hysteresis characteristics applying neural network based hysteresis (in Hungarian). *Híradástechnika*, LVII:4–9, 2002.
- [53] M. Kuczmann and A. Iványi. Neural network model of magnetic hysteresis. *COMPEL*, pages 367–376, 2002.
- [54] M. Kuczmann and A. Iványi. A new neural-network-based scalar hysteresis model. *IEEE Trans. on Magn.*, pages 857–860, 2002.
- [55] M. Kuczmann and A. Iványi. Calibration and measurement with 3D FluxSet sensor (in Hungarian). *Híradástechnika*, pages 34–37, 2003.
- [56] M. Kuczmann and A. Iványi. Neural network model for scalar and vector hysteresis. *Journal of Electrical Engineering 1-2*, pages 12–21, 2003.
- [57] M. Kuczmann and A. Iványi. Vector hysteresis model based on neural network. *COMPEL*, pages 730–743, 2003.
- [58] M. Kuczmann and A. Iványi. Nonlinear 2D edge element based FEM in $\mathbf{T}, \psi - \psi$ formulation. *Proceedings of the 9th OPTIM Conference, Brasov, Romania*, pages 41–48, 2004.
- [59] M. Kuczmann and A. Iványi. Calibration of FluxSet sensor. *Proceedings of the 12th International Symposium on Theoretical and Electrical Engineering, Warsaw, Poland*, pages 389–392, July 16-19, 2003.
- [60] M. Kuczmann and A. Iványi. Neural network based scalar hysteresis model. *Proceedings of the 10th International Symposium on Applied Electromagnetics and Mechanics, Tokyo, Japan*, pages 493–494, May 13-16, 2001.

- [61] M. Kuczmann and A. Iványi. Simulation of a nondestructive testing measurement system. *Proceedings of the 11th IGTE Symposium, Seggau Castle, Austria*, pages 376–381, September 13-15, 2004.
- [62] M. Kuczmann and A. Iványi. Vector hysteresis model based on neural network. *Proceedings of the 10th International IGTE Symposium, Graz, Austria*, pages 453–458, September 16-18, 2002.
- [63] M. Kuczmann and A. Iványi. Neural network based simulation of scalar hysteresis. *Proceedings of the 10th International Symposium on Electromagnetic Fields in Electrical Engineering, Cracow, Poland*, pages 413–416, September 20-22, 2001.
- [64] M. Kuczmann, P. Kis, A. Iványi, and J. Füzi. Vector hysteresis measurement. *Physica B*, 343:390–394, 2004.
- [65] D. Lederer, H. Igarashi, A. Kost, and T. Honma. Effective reluctivity calculation versus time step calculation of magnetic shielding with ferromagnetic material. *COMPEL*, 18:410–421, 1999.
- [66] Y. Liu, A. Bondeson, R. Bergström, M.G. Larson, and K. Samuelsson. Methods for computing eddy currents in laminated materials using edge elements. *Proceedings of the 10th IGTE Symposium, Graz, Austria*, pages 351–356, 2002.
- [67] I.D. Mayergoyz. *Mathematical Models of Hysteresis*. Springer-Verlag, New York, 1991.
- [68] O. Mihalache, G. Preda, T. Uchimoto, K. Demachi, and K. Miya. Crack reconstruction in ferromagnetic materials using nonlinear FEM-BEM scheme and neural networks. *Electromagnetic Nondestructive Evaluation (V)*, pages 67–74, 2001.
- [69] D. Minkov, T. Shoji, and J. Lee. Determining the depth distribution of magnetic dipoles in the dipole model of surface crack. *Electromagnetic Nondestructive Evaluation (IV)*, pages 9–16, 2000.
- [70] D. Minkov, T. Shoji, and J. Lee. Crack inversion based on measuring leakage magnetic field by InAs Hall element. *Electromagnetic Nondestructive Evaluation (V)*, pages 113–120, 2001.
- [71] M. Oka and M. Enokizono. High sensitive ECT probe using a differential type magneto-impedance effect sensor for a small reverse-side crack. *Electromagnetic Nondestructive Evaluation (IV)*, pages 95–102, 2000.
- [72] C. Papusoi and A. Stancu. An hysteretic remanent susceptibility and the moving Preisach model. *IEEE Trans. on Magn.*, 29(1):77–81, 1993.
- [73] J. Pávó, O. Bíró, and K. Hollaus. Calculation of the field map from the measurement data of the FluxSet sensor. *COMPEL*, 20(2):404–416, 1998.
- [74] G. Preda, O. Mihalache, B. Cranganu-Cretu, Z. Chen, and K. Miya. FEM-BEM coupling and neural network for reconstruction of crack shape from simulated pulse eddy current signals. *Energy and Information in Non-Linear Systems*, pages 110–113, 2001.

- [75] K. Preis, I. Bárdi, O. Bíró, K.R. Richter, J. Pávó, A. Gasparics, and I. Ticar. Numerical simulation and design of a FluxSet sensor by finite element method. *IEEE Trans. on Magn.*, 34(5):3475–3478, 1998.
- [76] J. Prohászka. *Material Science (in Hungarian)*. Tankönyvkiadó, Budapest, 1993.
- [77] C. Ragusa and M. Repetto. Anisotropic vector Preisach model and magnetic field solutions. *COMPEL*, 18(3):458–468, 1999.
- [78] C. Ragusa and M. Repetto. Accurate analysis of magnetic devices with anisotropic vector hysteresis. *Physica B*, 275:92–98, 2000.
- [79] M. Saghaffar, A. Kundu, and A. Nafalski. Dynamic magnetic hysteresis modelling using Elman recurrent neural network. *International Journal of Applied Electromagnetics and Mechanics*, 13:209–214, 2001/2002.
- [80] A. Salvini and P. Del Vecchio. Neural network and Fourier descriptor macro-modeling dynamic hysteresis. *Proceedings of the 12th COMPUMAG Conference, Sapporo, Japan*, pages 228–229, October 25–28, 1999.
- [81] E.S. Sazonov. *An Automated Damage Detection System for Armoured Vehicle Launched Bridge*. PhD thesis, West Virginia University, 2002.
- [82] H.R. Schwarz. *Methode der finiten Elemente*. B.G. Teubner, Stuttgart, 1991.
- [83] I. Sebestyén. Electric-field calculation for HV insulators using domain-decomposition method. *IEEE Trans. on Magn.*, 38(2):1213–1216, 2002.
- [84] C. Serpico and C. Visone. Magnetic hysteresis modeling via feed-forward neural networks. *IEEE Trans. on Magn.*, 34(3):623–628, 1998.
- [85] H. Shimoji and M. Enokinozo. E&S2 model for vector magnetic hysteresis property. *Journal of Magnetism and Magnetic Materials*, 254-255:290–292, 2003.
- [86] H. Shimoji, M. Enokinozo, and T. Todaka. Iron loss and magnetic fields analysis of permanent magnet motors by improved finite element method with E&S model. *IEEE Trans. on Magn.*, 37(5):3526–3529, 2001.
- [87] K. Simonyi and L. Zombory. *Theoretical Electrotechnik (in Hungarian)*. Műszaki Könyvkiadó, Budapest, 2000.
- [88] Zs. Szabó. *Hysteresis Models of Elementary Operators and Integral Equations*. PhD thesis, Budapest University of Technology and Economics, 2002.
- [89] T. Takagi and H. Fukutomi. Benchmark activities of eddy current testing for steam generator tubes. *Electromagnetic Nondestructive Evaluation (V)*, pages 235–252, 2001.
- [90] M. Tanaka and H. Tsuboi. Finite element model of natural crack in eddy current testing problem. *IEEE Trans. on Magn.*, 37(5):3125–3128, 2001.

- [91] M. Tanaka, H. Tsuboi, K. Ooshima, and M. Hashimo. Finite element model for crack with narrow gap in ECT problem. *Electromagnetic Nondestructive Evaluation (VI)*, pages 68–73, 2002.
- [92] T. Taniguchi, K. Nakamura, S. Yamada, and M. Iwahara. Image processing in eddy current testing for extraction of orientations of defects. *International Journal of Applied Electromagnetics and Mechanics*, 14:503–506, 2001/2002.
- [93] E. D. Torre. *Magnetic Hysteresis*. IEEE Press, New York, 1999.
- [94] E.D. Torre and Gy. Kádár. Hysteresis modeling: II. Accommodation. *IEEE Trans. on Magn.*, MAG-23(5):2823–2825, 1987.
- [95] L. Tóth. Fatigue crack growth laws and their material parameters. *VII Summer School of Fracture Mechanic-Current Research on Fatigue and Fracture, Pokrzywna, Poland*, 2001.
- [96] M. Uesaka, K. Hakuta, K. Miya, K. Aoki, and A. Takahashi. Eddy-current testing by flexible microloop magnetic sensor array. *IEEE Trans. on Magn.*, 34(4):2287–2297, 1998.
- [97] G. Vértesy, A. Gasparics, and J. Szöllösy. High sensitivity magnetic field sensor. *Sensors and Actuators*, 85:202–208, 2000.
- [98] C. Visone, C. Serpico, I.D. Mayergoyz, M.W. Huang, and A.A. Adly. Neural-Preisach-type models and their application to the identification of magnetic hysteresis from noisy data. *Physica B*, 275:223–227, 2000.
- [99] www.mathworks.com.
- [100] www.ni.com.
- [101] T.V. Yioultis and T.D. Tsiboukis. Multiparametric vector finite elements: a systematic approach to the construction of three-dimensional, higher order, tangential vector shape functions. *IEEE Trans. on Magn.*, 32(3):1389–1392, 1996.
- [102] T.V. Yioultis and T.D. Tsiboukis. Development and implementation of second and third order vector finite elements in various 3-d electromagnetic field problems. *IEEE Trans. on Magn.*, 33(2):1812–1815, 1997.
- [103] N. Yusa, W. Cheng, and K. Miya. Reconstruction of the parameters of natural crack model candidates by using neural networks. *Electromagnetic Nondestructive Evaluation (IV)*, pages 135–142, 2000.
- [104] F. Zaoui, C. Marchand, and A. Razeq. Sizing and localization of cracks using FEM and a constrained stochastic algorithm. *Electromagnetic Nondestructive Evaluation (III)*, pages 89–97, 1999.
- [105] O.C. Zienkiewicz and R. Taylor. *The Finite Element Method*. McGraw-Hill, Maidenhead, 1991.